NATIONAL UNIVERSITY OF SCIENCES & TECHNOLOGY
COLLEGE OF ELECTRICAL AND MECHANICAL ENGINEERING, RAWALPINDI, PAKISTAN

Trajectory Generation and Tracking for UAV Landing

By
Muhammad Sharjil

MS-64 (Mechanical Engineering)
(2010-NUST-MS-PhD-Mech-06)

Thesis submitted to the Department of Mechanical Engineering,
National University of Sciences and Technology,
College of Electrical and Mechanical Engineering, Rawalpindi, Pakistan
in partial fulfillment of the requirements for the degree of Masters of Science in Mechanical Engineering

Thesis Supervisor
Dr. Hasan Aftab Saeed


بسم الله الرحمن الرحيم

CERTIFICATE OF COMPLETENESS

It is hereby certified that the dissertation submitted by NS **Muhammad Sharjil**, Reg No. **2010-NUST-MS-PhD-Mech-06**, Titled: ***Trajectory Generation and Tracking for UAV Landing*** has been checked/reviewed and its contents are complete in all respects.

Supervisor's Name: **Dr. Hasan Aftab Saeed**

Signature: ______________________

Date: ______________________

DECLARATION

I hereby declare that this thesis is entirely and purely my own work and based on my personal efforts and intellect under the guidance and supervision of my thesis supervisor

“Dr. Hasan Aftab Saeed”

All the sources used in this thesis are properly cited and no portion of this thesis is an act of plagiarism. This work is purely done for the fulfillment of requirements for aforementioned degree in respective department. No part of this thesis is submitted for any other application for any degree or qualification in this or any other university, degree awarding or non-degree awarding college or institute.

Signature: ____________________

Muhammad Sharjil

ACKNOWLEDGMENT

Countless words of thanks and admiration to Allah, the Almighty. Without His Will and Kindness, this accomplishment would not have been possible.

I would like to express my sincere gratitude to my advisor, Dr. Hasan Aftab Saeed, for motivation and continuous support. His supervision gave me direction throughout research and writing of this thesis.

Besides my advisor, I would also like to thank my thesis committee members Dr. Shakil Ahmed, Mr. Raja Amir Azim and Dr. Tariq Talha for their encouragement and continuous support. I would like to extend special thanks to Dr. Shakil Ahmed, whose guidance, enthusiasm, technical expertise and out of the way help were pivotal in concluding this research. Mr. Raja Amir Azim was instrumental in casting of thesis objective and critical evaluation that helped me a lot in shaping this thesis.

I would like to thank my colleague Mr. Faisal Aftab, who always responded whenever I needed help. I would not forget to thank my dear friends Mr. Uzair Gill, Mr. Rizwan Ahmed and Flt. Lt. Shahid Hussain, for always being there for me. I have been fortunate to have met and studied with many wonderful people like Mr. Kamran Kiyani and Mr. Salman Siddiqui, who made my time at college enjoyable and their continuous encouragement made it possible for me to reach all the way to this point.

Last but not the least, special thanks to my parent and siblings, who provided me with all the comfort and resources.

ABSTRACT

Landing is the most critical phase of aircraft flight and poses vulnerability. Automatic landing offers an added safety by minimizing undue human errors during this critical flight phase. Unmanned Air Vehicle reduces this risk by eliminating human loss but monetary aspect is still there. This makes landing methodology improvement, an active research field for safe recovery of small scale UAV's in wake of constraints. Small scale UAV runway landing option offers research ground being equally viable for large scale UAV's and civil airliners. Driving ground for active research being the reduction in required runway length while offering minimum impact velocity at touch down to increase landing feasibility at short length airfields. This results in lower structure stresses.

Landing consist of glide slope capturing phase and flare phase. UAV maintains a constant descend rate during glide phase till a threshold altitude above the runway called Flare initiation height. After achieving this altitude, UAV gets into flare maneuver to touch down on runway with minimum vertical velocity in order to reduce impact at touch down. This is attained by shedding off the kinetic and potential energy in the form of increased drag through pitch up maneuver. The distance required during landing depends upon obstacle avoidance, engine control capabilities and permissible impact velocity.

Extensive research is already being done on online/offline trajectory generation for runway landing of fixed wing UAV. This thesis is aimed at design and development of vertical plane trajectory generation algorithm and tracking control for autonomous runway landing of fixed wing UAV. The proposed algorithm is capable of touch down at intended point on runway with intended vertical velocity allowing reduced required distance during flare. The algorithm is capable of being computationally viable for inflight calculations.

H_∞ SISO control law for altitude profile tracking with cascaded inner loop H_∞ SISO pitch rate stability augmented pitch loop are designed in continuous time domain for Glide phase. H_∞ SISO control law for vertical velocity profile tracking with cascaded inner loop H_∞ SISO pitch rate stability augmented pitch loop are designed in continuous time domain for flare phase. These controllers are evaluated for stability, performance and uncertainty over an array of linear models depicting landing flight envelope. Controller implementation is carried out in discretized format in 6dof simulation and evaluated to track the trajectory command for accurate landing on runway.

FASER (Free-flying Aircraft for Subscale Experimental Research) of UAV Laboratories, University of Minnesota is used as the subject platform. C-language based Simulink® interfaced 6dof simulation is used to implement and evaluate the performance of developed algorithm and tracking controller.

TABLE OF CONTENTS

CERTIFICATE OF COMPLETENESS i
DECLARATION ii
ACKNOWLEDGMENT iii
ABSTRACT iv
LIST OF FIGURES viii
LIST OF TABLES xii
Chapter 1: INTRODUCTION 1
  1.1 Overview 1
  1.2 Thesis Objective 2
  1.3 Methodology 2
  1.4 Thesis Scope 2
  1.5 Literature Survey 3
  1.6 Thesis Outline 4
Chapter 2: UAV PLATFORM 5
  2.1 Physical Geometry 5
  2.2 Nonlinear Simulation Model 6
    2.2.1 Aerodynamic Model 7
      2.2.1.1 Force Equations 7
      2.2.1.2 Moment Equations 8
      2.2.1.3 Kinematic Equations 9
    2.2.2 Inertia Model 9
    2.2.3 Propulsion Model 17
      2.2.3.1 Propulsion Motor 17
      2.2.3.2 Propeller Characteristics 17
    2.2.4 Actuator Model 19
Chapter 3: Linearization and Open Loop Response 20
  3.1 6DoF Linearization 20
    3.1.1 Extraction of Longitudinal and Lateral Model 21
  3.2 Open Loop Simulation 24
Chapter 4: Landing Flight Phase 29
  4.1 Landing Flight Phase 29
    4.1.1 Base leg 30

4.1.2 Glide Phase 30
4.1.3 Flare Phase 30
4.2 Landing Schemes 31
4.2.1 Glide Phase 31
4.2.2 Flare Phase 31
4.2.2.1 Scheme 1: Exponential Trajectory Profile Generation [11] 31
4.2.2.2 Scheme 2: Exponential Trajectory Profile Generation with Touchdown at Intended Point with intended Vertical Speed [16] 33
4.2.2.3 Scheme 3: Exponential Height/Vertical Velocity Command with Time Constant Calculation based on Initial and Final Vertical Velocity [20] 35
4.2.2.4 Scheme 4: Linear Height Profile [18] 36
4.3 Landing Parameter Calculation 36
4.3.1 Glide Phase 36
4.3.2 Flare Phase 38
Chapter 5: Proposed Landing Scheme 39
5.1 Proposed Flare Phase Scheme 39
5.2 Implementation and Online computation 40
5.3 Results 42
Chapter 6: Control System Design 46
6.1 Onboard Sensors 46
6.2 H_∞ Loop Shaping Technique 46
6.2.1 Loop Shaping Fundamental Relations 46
6.2.2 Weights Selection for Loop Shaping 47
6.2.3 H_∞ Loop shaping 47
6.3 Controller Design 50
6.3.1 Control Scheme 50
6.3.2 Glide Phase 51
6.3.2.1 The Plant Model 51
6.3.2.2 The Specifications 51
6.3.2.3 Pitch Rate Loop Design 52
6.3.2.4 Pitch Loop Design 52
6.3.2.5 Height Controller 60
6.3.3 Flare Phase 66
6.3.3.1 The Plant Model 66

6.3.3.2 The Specifications 66
6.3.3.3 Pitch Rate Loop Design 66
6.3.3.4 Pitch Loop Design 68
6.3.3.5 Vertical Velocity Controller 74
Chapter 7: Simulation Results 80
7.1 Glide Phase 80
7.2 Flare Phase 81
Chapter 8: Conclusion 88
8.1 Conclusion 88
8.2 Future Work Recommendations 88
References 89

LIST OF FIGURES

Figure 1.1: Thesis Methodology 2

Figure 1.2: Thesis Layout 4

Figure 2.1: Research test bed: FASER RC plane[30] 5

Figure 2.2: FASER nonlinear simulation [27] 6

Figure 2.3: Forces and moments in aircraft body axis [30] 7

Figure 2.4: Rolling moment coefficient data 10

Figure 2.5: Pitching moment coefficient data 10

Figure 2.6: Yawing moment coefficient data 11

Figure 2.7: Drag force coefficient data 11

Figure 2.8: Lift force coefficient data 12

Figure 2.9: Side force coefficient data 12

Figure 2.10: Elevator Drag force coefficient data 13

Figure 2.11: Elevator Lift force coefficient data 13

Figure 2.12: Elevator pitching moment coefficient data 14

Figure 2.13: Aileron rolling moment coefficient data 14

Figure 2.14: Rudder side force coefficient data 15

Figure 2.15: Rudder side force coefficient data 15

Figure 2.16: Rudder yawing moment coefficient data 16

Figure 2.17: Rudder yawing moment coefficient data 16

Figure 2.18: Motor Power Output 18

Figure 2.19: Propeller Coefficient of Thrust 19

Figure 2.20: Propeller Coefficient of Power 19

Figure 3.1: Procedure for Linearization and Decoupling of Longitudinal and Lateral modes 20

Figure 3.2: Forward velocity openloop step response for $\delta_e = 1^o$ 24

Figure 3.3: Angle of attack openloop step response for $\delta_e = 1^o$ 24

Figure 3.4: Pitch rate openloop step response for $\delta_e = 1^o$ 25

Figure 3.5: Pitch angle openloop step response for $\delta_e = 1^o$ 25

Figure 3.6: Height openloop step response for $\delta_e = 1^o$ 26

Figure 3.7: Beta openloop step response for $\delta_a = 1^o$ 26

Figure 3.8: Roll rate openloop step response for $\delta_a = 1^o$ 27

Figure 3.9: Yaw rate openloop step response for $\delta_a = 1^o$ 27

Figure 3.10: phi angle openloop step response for $\delta_a = 1^o$ 28

Figure 3.11: Yaw angle openloop step response for $\delta_a = 1^o$ 28

Figure 4.1: Landing Trajectory 29

Figure 4.2: Longitudinal Plane Landing Trajectory 30

Figure 4.3: Glide Phase Trajectory 32

Figure 4.4: Landing Trajectory for scheme 1 [11] 33

Figure 4.5: Landing Trajectory for scheme 2 [16] 34

Figure 4.6: Landing Trajectory for scheme 4 [18] 37

Figure 4.7: γ Angle for different landing Velocities 38

Figure 5.1: Proposed Landing Scheme Trajectory 40

Figure 5.2: Proposed Algorithm's Online Computation Flow Chart 41

Figure 5.3: Proposed algorithm online computation vertical velocity results 41

Figure 5.4: Proposed algorithm online computation height results 42

Figure 5.5: Height profile vs distance required comparison 44

Figure 5.6: Vertical velocity profile vs distance required comparison 45

Figure 6.1: Shaped Plant and Controller [35] 48

Figure 6.2: H_∞ close loop structure [34] 49

Figure 6.3: Co-prime Factorization [34] 50

Figure 6.4: Control Schemes [11] 51

Figure 6.5: Plant selection for Glide phase Controller 52

Figure 6.6: Root locus for Glide phase pitch rate Loop 53

Figure 6.7: Bode plot for Glide phase pitch rate Loop 53

Figure 6.8: Bode Plots of Glide phase pitch control Loop shaping weights W1 and W2 55

Figure 6.9: Bode plot for Glide phase open loop shaped plant and H_∞-controller+plant 56

Figure 6.10: Nyquist plot for Glide phase open loop pitch control transfer function with H_∞ controller .. 57

Figure 6.11: Bode plot for Glide phase close loop pitch control and sensitivity transfer function with H_∞ controller 57

Figure 6.12: Step response for Glide phase pitch control close loop with H_∞ controller 58

Figure 6.13: Glide phase step response for pitch control close loop over the whole envelope 58

Figure 6.14: Glide phase pitch control Gain/Phase margin and close loop bode plot over the whole envelope 59

Figure 6.15: Bode plot of Height transfer function with cascaded pitch loop... 60

Figure 6.16: Bode plots of weights W1 and W2 for shaping Height loop.. 61

Figure 6.17: Bode plot for height loop shaped Plant and H∞ controller+plant 62

Figure 6.18: Bode plots and nyquist plot for Height Control open loop transfer function with H∞ controller.. 63

Figure 6.19: Bode plot for Height Control close loop and sensitivity transfer function with H∞ controller 63

Figure 6.20: Step response for Height Control close loop with H∞ controller... 64

Figure 6.21: Glide Phase close loop height control step response over the envelope.............................. 64

Figure 6.22: Glide Phase open loop height control stability margins and close loop bodeplot over the envelope 65

Figure 6.23: Plant selection for Flare phase Controller 66

Figure 6.24: Root locus for flare phase pitch rate loop 67

Figure 6.25: Bode plot for flare phase pitch rate loop.. 67

Figure 6.26: Bode Plots of Flare Phase Pitch Control Loop shaping weights W1 and W2.......................... 69

Figure 6.27: Bode plot for flare phase pitch control open loop transfer function with H∞ controller...... 70

Figure 6.28: Nyquist plot for flare phase pitch control open loop transfer function with H∞ controller... 71

Figure 6.29: Bode plot for flare phase pitch control close loop and sensitivity transfer function with H∞ controller.. 71

Figure 6.30: Step response for flare phase pitch control close loop with H∞ controller............................ 72

Figure 6.31: Flare Phase close loop pitch control step response over the envelope 72

Figure 6.32: Flare phase open loop pitch control stability margins and close loop bode plot over the envelope 73

Figure 6.33: Bode plot of Flare Phase Vertical Velocity transfer function with cascaded pitch loop......... 74

Figure 6.34: Bode plots of weights W1 and W2 for shaping vertical velocity loop 75

Figure 6.35: Open loop bode plot for vertical velocity transfer function with H∞ controller 76

Figure 6.36: Nyquist plot for vertical velocity open loop transfer function with H∞ controller................. 77

Figure 6.37: Vertical velocity close loop bode plot and sensitivity transfer functions with H∞ controller 77

Figure 6.38: Close loop step response for vertical velocity with H∞ controller... 78

Figure 6.39: Flare Phase close loop Vertical Velocity step response over the envelope........................... 78

Figure 6.40: Flare Phase stability margins and close loop bode plot over the envelope 79

Figure 7.1: Glide phase height tracking 82

Figure 7.2: Glide phase pitch angle tracking 82

Figure 7.3: Glide phase elevator deflection 83

Figure 7.4: Glide phase distance to runway 83

Figure 7.5: Glide Phase angle of attack 84

Figure 7.6: Flare phase vertical velocity tracking 84

Figure 7.7: Flare phase pitch angle tracking 85

Figure 7.8: Flare phase height profile 85

Figure 7.9: Flare phase elevator deflection 86

Figure 7.10: Flare phase distance to runway 86

Figure 7.11: Flare Phase angle of attack 87

LIST OF TABLES

Table 2.1: FASER Parameters [30] 6

Table 2.2: Damping Derivatives 9

Table 2.3: Inertia Data 17

Table 3.1: Linear Model Extraction Input Data 21

Table 3.2: Longitudinal mode characteristics 22

Table 3.3: Dutch Roll mode characteristics 23

Table 3.4: Spiral mode and Roll Subsidance mode characteristics 23

Table 4.1: Flare Phase parameters 38

Table 5.1: Fixed parameters for comparison of trajectory generation algorithms 42

Table 5.2: Test cases for evaluation and comparison of trajectory generation algorithms 43

Table 5.3: Comparison of distance output for trajectory generation schemes 43

Chapter 1: INTRODUCTION

1.1 Overview

The term Unmanned Aerial Vehicle (UAV) is a pilotless flying platform being capable of autonomous flight or to be remotely controlled. It can be expendable or recoverable, and can carry a lethal or non-lethal payload [**1**]. In today's growing world of technological advancement, unmanned aerial vehicle (UAV) platforms have evolved into multi-operational and autonomous flying machines. They have proved to be useful for both military as well as civilian applications [**2**, **3**, **4**, **5**]. In civil applications, the UAV's are used for monitoring/reporting of wildfire in forests, border patrol, search and rescue missions, meteorological data acquisition, maritime monitoring and pipeline inspection etc. Military application ranges from surveillance, reconnaissance, air support and carrying out of striking missions [**6**].

UAV platforms are preferred over piloted aircrafts due to:

- Multiple mission capability
- Low budget
- Ease of operation
- Minimum probability of operation team damage

Landing is the most critical part of UAV mission and is the prime factor in defining the functional and operational capability of UAV. Landing options available for fix wing UAVs depend on their size, configuration and mission profiles. The prime objective of landing phase is to get the UAV back onto the ground safely in shortest possible landing distance with minimum impact on structure at touch down. Wheeled landing, belly landing, parachute- airbag recovery, deep stall, sky-hook recovery, net recovery and parafoil are the some of the available landing options that define the category of fix wing UAV.

Wheeled landing is still the most common technique for tactical UAVs landing. It is analogous to landing of fighter jets and civil airlines. This type of landing is preferred due to reliability and handing issues. UAVs are required to ensure high accuracy in wheeled landing. Statistical crash data for fix wing UAVs and large commercial jet plane indicates that approach and landing phases are the most vulnerable phases prone to disaster [**7**, **8**].

Automatic landing capability enhances the overall independence of the system [**7**]. Landing autopilot ensures greater safety and provides simplicity of operation by reducing the operator's workload load. It also enhances wind catering capabilities during landing such as high winds, turbulence and wind shear.

1.2 Thesis Objective

The primary objective of this project is to design trajectory generation algorithm for runway based landing of UAV being capable of landing at the desired touchdown point with intended touchdown vertical speed. This implies that the UAV track the generated landing pattern in order to land accurately. Thus, control system for tracking of generated trajectory command is to be designed for accurate landing. Moreover, the results of the algorithm are to be compared with the existing landing trajectory schemes to highlight the benefits of this scheme. The main objective can be summarized as:

- being capable of executing fully autonomous landing confined to vertical plane
- must be capable of generating online parameters for flare phase, based on the current state of the vehicle and the desired state at chosen touch down point

1.3 Methodology

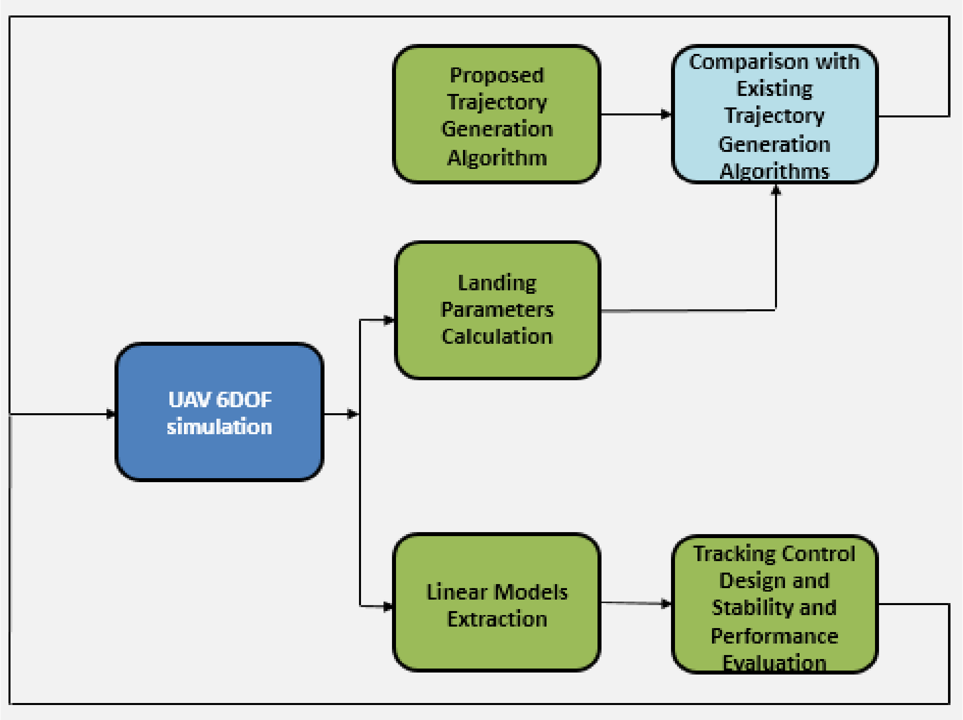

Figure 1.1: Thesis Methodology

1.4 Thesis Scope

The research objective is confined to the trajectory generation and tracking in longitudinal plane. Moreover, the designed algorithm is confined to comparison with existing trajectory generation algorithms for distance requirement within same levels of height and touch down speed.

1.5 Literature Survey

Trajectory generation and tracking control for accurate landing of UAV is an active research domain. Different methodologies have been anticipated to handle the automatic landing of UAVs based on exploitation of both classical control theory and modern intelligent control techniques. Trajectory for wheeled landing is a depiction of pilot's instinct. Practical landing data for pilot's actions during landing are examined and system identification techniques are utilized for mathematical model validation of aircraft and classical PI altitude controller is employed for the landing phase tracking [**9**]. Aircraft transitory phase between glide path to flare path is focused in [**10**] and a blending function is formulated for mixing of trajectory command during this transitory phase. An exponential trajectory profile for flare phase is proposed by shaping the vertical velocity profile [**11**] while an exponential profile in height is shaped in [**12**]. LOS based nonlinear guidance logic in longitudinal plane for glide phase is employed based on [**14**] in [**13**, **21**]. Classical PI controllers are utilized for tracking of generated path.

Landing of a fixed-wing UAV on moving platform i.e. ship deck is explored in [**15**], while autonomous landing controllers are designed with classical controller design theory for fast inner-loop attitude controllers and slower outer-loop point-mass controllers.

Non-linear dynamic inversion control technique for achieving autonomous landing [**16**] through tracking of generated trajectory, based on relative position of UAV from runway. The generated landing path ensures smooth and continuous switching between glide phase to the flare phase. A single GPS antenna and airspeed sensor based fully autonomous taxiing, take-off and landing of fixed wing UAV is presented in [**17**] and LQR controllers are utilized for autonomous take-off and landing.

Landing trajectory generation centered on distance to runway based height profile generation with fix vertical velocity profile during flare phase. The normal acceleration control scheme utilizing classical PID controllers are designed to track the trajectory [**18**, **19**]. Methodology is presented for parameter calculation of exponential trajectory [**11**] based on initial and final vertical velocity during flare. The glide phase trajectory is based on generation on vertical velocity based command taking into account the current height of UAV above the ground and distance from runway [**20**].

Neural networks online learning based controllers for landing phase of a fighter aircraft to cater for actuator failures and severe winds is addressed in [**22**]. Auto landing control law problem is addressed with H_2 controllers and with Linear Matrix Inequalities (LMI's) approach [**23**]. Comparison of classical controllers with neural aided landing controllers for heavy transport aircrafts is given in [**24**]. Mixed $H_2/H\infty$ control technique is utilized for auto landing of commercial airplane in [**25**]. A standard trajectory generation is discussed for autonomous landing for the IAI UAV while fault tolerance uncertainty is catered by means of a neural network based flight control module [**26**].

1.6 Thesis Outline

This thesis is organized as follows: Chapter 2 describes the UAV platform and the associated 6-DOF model. Chapter 3 discusses the linearization procedure around a cruise condition in landing leg before acquiring approach and the open loop characteristics of the system. Chapter 4 describes the landing flight phase, existing flare phase landing trajectory generation algorithms and calculation of landing parameters. Chapter 5 presents the proposed flare phase trajectory generation algorithm and its online implementation along with comparison results with existing schemes. Chapter 6 is related to control system design in longitudinal plane for tracking of generated command. H_∞ loop shaping based controllers are designed for landing phase. Chapter 7 is related to simulation results. Chapter 8 presents conclusion and recommendations for future work.

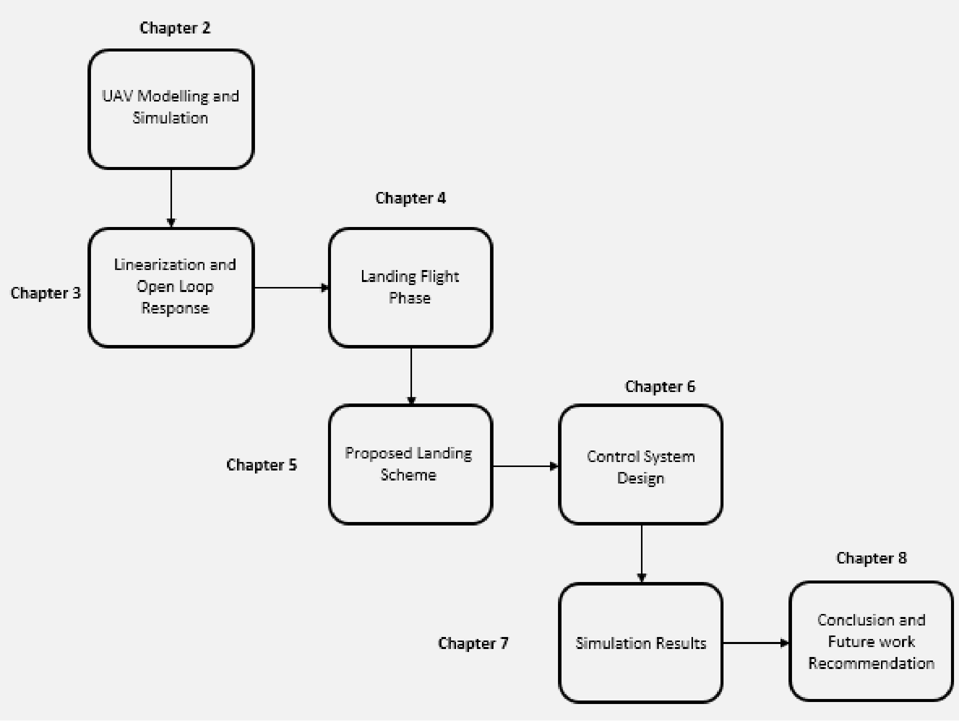

Figure 1.2: Thesis Layout

Chapter 2: UAV PLATFORM

Aircraft nonlinear dynamic models are used extensively for stability and control analysis. 6dof simulation embedding nonlinear dynamic model provide platform for flight control and trajectory generation algorithm implementation and evaluation. This includes aerodynamics, mass-inertia, propulsion, gravity, environment, actuation and sensor models.

In this chapter UAV platform from university of Minnesota's Aerospace Department UAV Research Group [**27**] will be discussed, which is used in this thesis. This is a commercial off the shelf UAV with a detailed experimentally tuned 6dof model available openly at university of Minnesota website.

Section 2.1 describes physical parameters of UAV used in this thesis. Section 2.2 outlines the 6dof nonlinear simulation model.

2.1 Physical Geometry

FASER (Free-flying Aircraft for Subscale Experimental Research) [**28**] shown in figure 2.1, is a commercial off the shelf, fixed wing radio controlled UAV. Table 2.1 provides a summary of important physical parameters.

Figure 2.1: Research test bed: FASER RC plane[30]

Table 2.1: FASER Parameters [30]

Parameter	FASER
Wing Span (m)	1.92
Wing Chord (m)	0.43
Length (m)	1.32
Wing Reference Area (m^2)	0.769
MTOW(Tested) (Kg)	9.07
Empty Weight (Kg)	6.35
Endurance (min)	15 – 20
Cruise Velocity (m/sec)	20 – 30

2.2 Nonlinear Simulation Model

Matlab/Simulink environment based nonlinear dynamic model is taken from [**27**]. Framework is based on Simulink modeling of Aerosonde UAV and relies of AeroSim Blockset from Unmanned Dynamics [**29**]. Nonlinear simulation layout of FASER [**27**] is shown in figure 2.2.

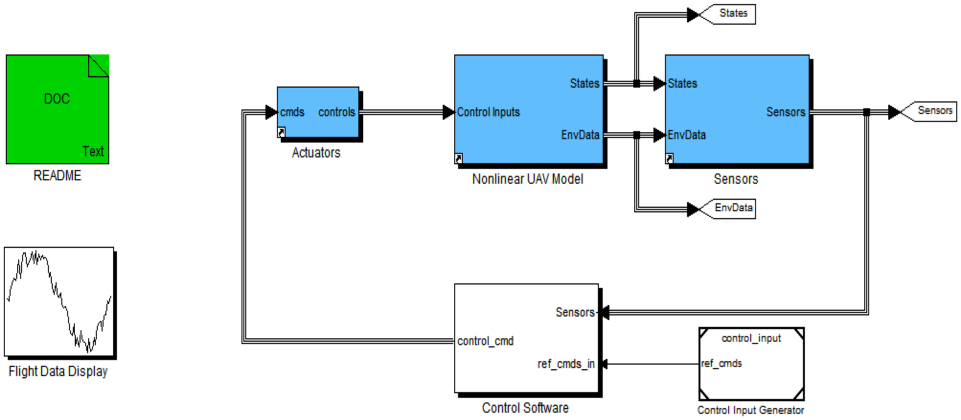

Figure 2.2: FASER nonlinear simulation [27]

2.2.1 Aerodynamic Model

Six degree of freedom equations describing the dynamic model of an aircraft, are derived from the forces in *X*, *Y* and *Z* body axis and moments *L*, *M* and *N* about the body axis [**30**]. Figure 2.3 depicts the forces and moments definition in body axis.

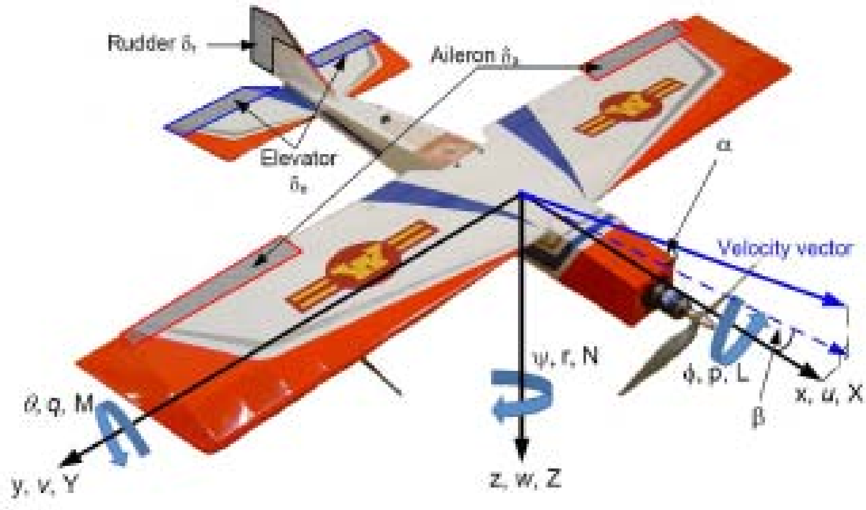

Figure 2.3: Forces and moments in aircraft body axis [30]

2.2.1.1 Force Equations

The linear velocities in body axis are calculated using summation of forces [**30**]:

$$u = rv - qw + \frac{\overline{q}S}{m} C_X - g\sin\theta + \frac{T}{m} \tag{2. 1}$$

$$\dot{v} = pw - ru + \frac{\overline{q}S}{m} C_Y - g\cos\theta\sin\phi \tag{2. 2}$$

$$\dot{w} = qu - pv + \frac{\overline{q}S}{m} C_Z - g\cos\theta\cos\phi \tag{2. 3}$$

where

{*u* (*m/s*), *v* (*m/s*) and *w* (*m/s*)} = body axis linear velocities

{*p* (*rad/s*), *q* (*rad/s*) and *r* (*rad/s*)} = body axis angular rates,

{*φ* (*rad*), *Θ* (*rad*) and *ψ* (*rad*)} = body attitude angles

$\overline{q}$ (*Pa*) = dynamic pressure

{C_X, C_Y and C_j} = aerodynamic force coefficients. The aerodynamic force coefficients are [**30**]

$$C_X = C_L \sin\alpha - C_D \cos\alpha \tag{2. 4}$$

$$C_Z = -C_D \sin\alpha - C_L \cos\alpha \tag{2. 5}$$

$$C_Y = C_{Y_\beta} + C_{Y_{\delta r}} \delta r + \frac{b}{2V_a}(C_{Y\,p}\, p + C_{Y\,r}\, r) \tag{2.6}$$

where

α (*rad*) = angle of attack

β (*rad*) = sideslip angle. The *x*, *y* and *z* axis body forces are [**30**]:

$$X = \overline{q} S C_X \tag{2.7}$$

$$Y = \overline{q} S C_Y \tag{2.8}$$

$$Z = \overline{q} S C_Z \tag{2.9}$$

The lift (C_L) and drag (C_D) coefficients are given by [**30**]:

$$C_L = C_{L0} + C_{L\alpha}\alpha + C_{L\,\delta e}\,\delta_e + \frac{c}{2V_a}(C_{L_{\dot\alpha}}\dot\alpha + C_{L_q} q) \tag{2.10}$$

$$C_D = C_{D_0} + C_{D_{\delta e}}\,\delta_e + C_{D_{\delta r}}\,\delta_r + \frac{(C_L - C_{L_{\min}})}{\pi . e . AR} \tag{2.11}$$

2.2.1.2 Moment Equations

The angular rate equations are given by [**30**]:

$$\dot p - \frac{I_{xz}}{I_{xx}}\dot r = \frac{\overline{q}Sb}{I_{xx}}c_l - \frac{I_{zz} - I_{yy}}{I_{xx}}qr + \frac{I_{xz}}{I_{xx}}qp \tag{2.12}$$

$$\dot q = \frac{\overline{q}S\overline{c}}{I_{yy}}c_m - \frac{I_{xx} - I_{zz}}{I_{yy}}pr - \frac{I_{xz}}{I_{yy}}(p^2 - r^2) + \frac{I_p}{I_{yy}}\omega_p r \tag{2.13}$$

$$\dot r - \frac{I_{xz}}{I_{zz}}\dot p = \frac{\overline{q}Sb}{I_{zz}}c_n - \frac{I_{yy} - I_{xx}}{I_{zz}}pq - \frac{I_{xz}}{I_{zz}}qr - \frac{I_p}{I_{zz}}\omega_p q \tag{2.14}$$

where

ω_p (*rad/s*) = propeller rotation velocity,

{I_{xx}, I_{yy}, I_{zz}, I_{xz} and I_p} = moment of inertia (kgm^2) coefficients for the aircraft and propulsion system

{c_l, c_m and c_n } = non-dimensional moment coefficients. These are expressed as:

$$c_l = c_{l\,\beta}\beta + c_{l\,\delta a}\delta a + c_{l\,\delta r}\delta r + \frac{b}{2V_a}(c_{l\,p}\,p + c_{l\,r}\,r) \tag{2.15}$$

$$c_m = c_{m\,0} + c_{m\,\alpha}\alpha + c_{m\,\delta e}\delta e + \frac{\overline{c}}{2V_a}(c_{m\,\dot\alpha}\dot\alpha + c_{m\,q}\,q) \tag{2.16}$$

$$c_n = c_{n\beta}\beta + c_{n\delta a}\delta a + c_{n\delta r}\delta r + \frac{b}{2V_a}(c_{np}p + c_{nr}r) \qquad \textbf{(2. 17)}$$

The moments about the body axis are given by [**30**]:

$$L = \bar{q}Sbc_l \qquad \textbf{(2. 18)}$$

$$M = \bar{q}Sbc_m \qquad \textbf{(2. 19)}$$

$$N = \bar{q}Sbc_n \qquad \textbf{(2. 20)}$$

2.2.1.3 Kinematic Equations

The kinematics equations relate Euler angles {*φ*, *Θ*, *ψ*}, body angular rates {*p*, *q*, *r*} and aerodynamics angles {*α*, *β*, *γ*}. These are given as [**30**]:

$$\dot{\phi} = p + \tan\theta(q\sin\phi + r\cos\phi) \qquad \textbf{(2. 21)}$$

$$\dot{\theta} = q\cos\phi - r\sin\phi \qquad \textbf{(2. 22)}$$

$$\dot{\psi} = \frac{q\sin\phi + r\cos\phi}{\cos\theta} \qquad \textbf{(2. 23)}$$

$$\theta = \gamma + a\cos\phi + \beta\sin\phi \qquad \textbf{(2. 24)}$$

Table 2.2: Damping Derivatives

CL_q	**Cm_q**	**Cl_p**	**Cl_r**	**Cn_p**	**Cn_r**	**CY_r**
6.2928	-7.8542	-0.3731	0.1505	-0.0560	-0.1230	0.1516

2.2.2 Inertia Model

Aircraft mass, center of gravity and moment of inertia coefficients are described by inertia model. The moment of inertia matrix I is [**30**]:

$$\mathrm{I} = \begin{bmatrix} \mathrm{I}_{xx} & -\mathrm{I}_{xy} & -\mathrm{I}_{xz} \\ -\mathrm{I}_{yx} & \mathrm{I}_{yy} & -\mathrm{I}_{yz} \\ -\mathrm{I}_{zx} & -\mathrm{I}_{zy} & \mathrm{I}_{zz} \end{bmatrix} \qquad \textbf{(2. 25)}$$

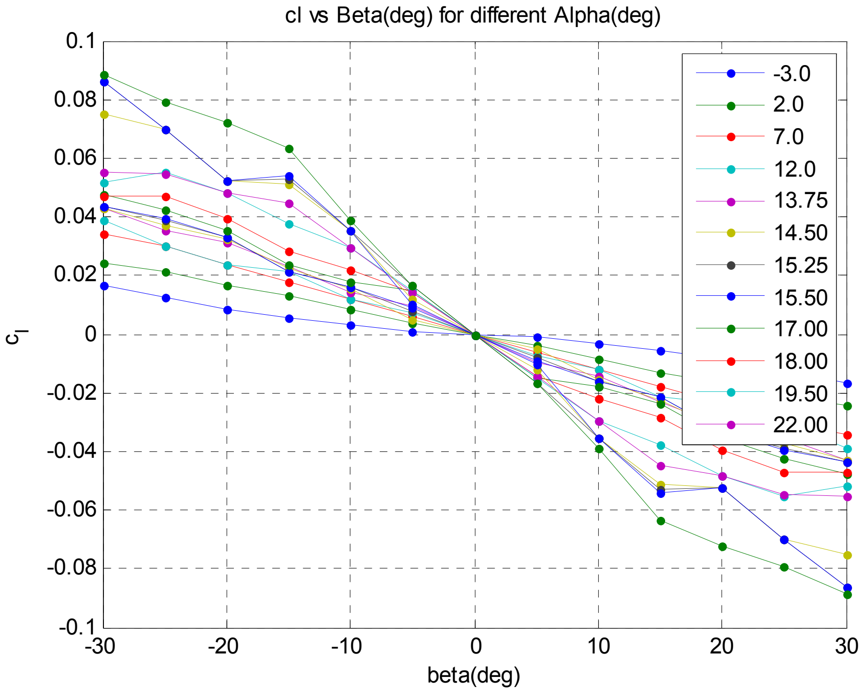

Figure 2.4: Rolling moment coefficient data

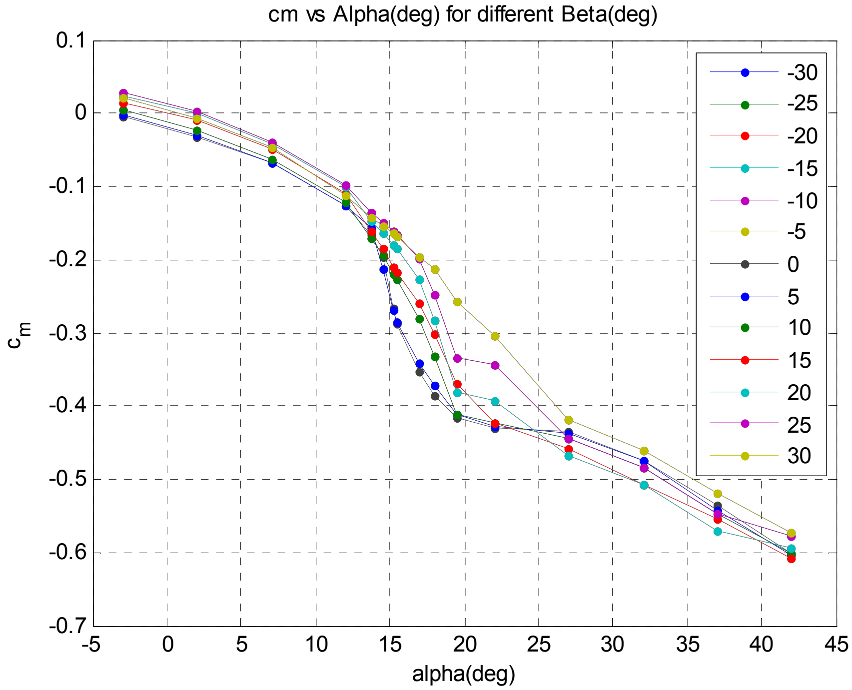

Figure 2.5: Pitching moment coefficient data

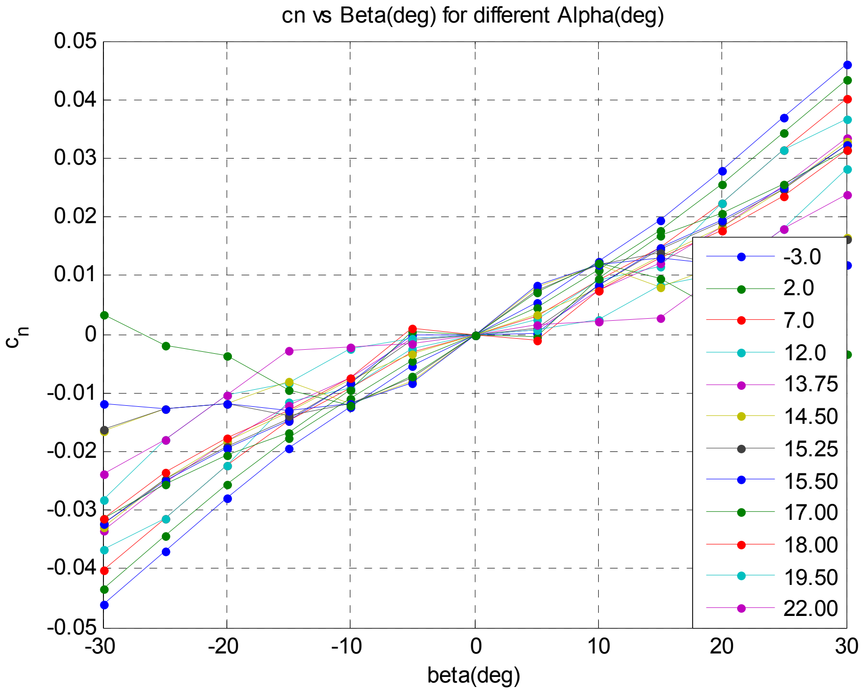

Figure 2.6: Yawing moment coefficient data

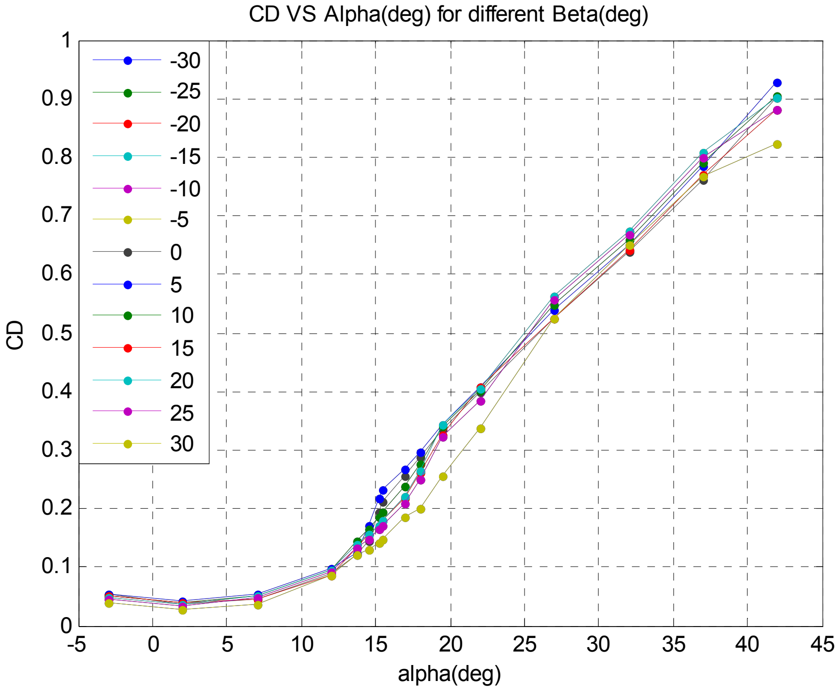

Figure 2.7: Drag force coefficient data

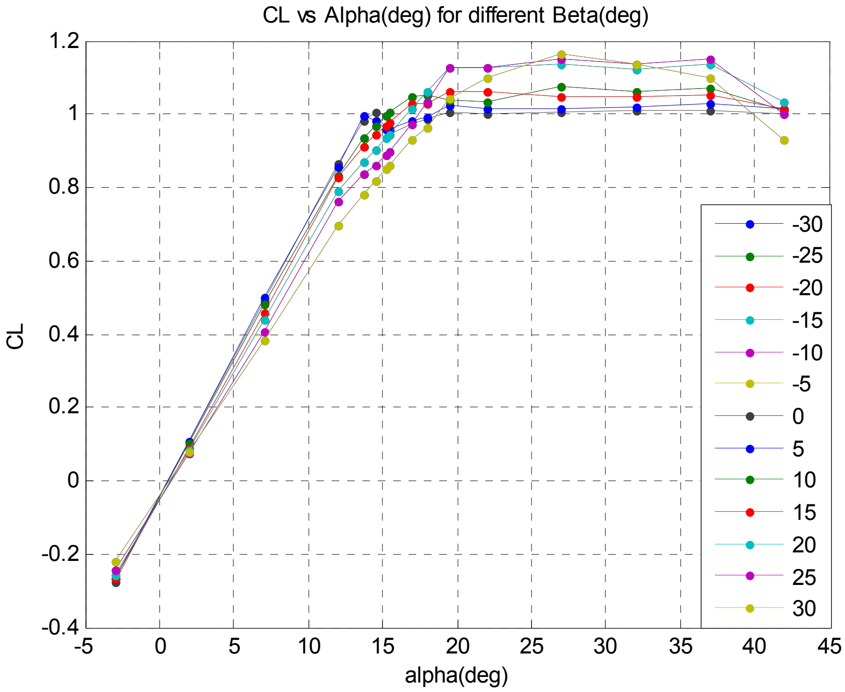

Figure 2.8: Lift force coefficient data

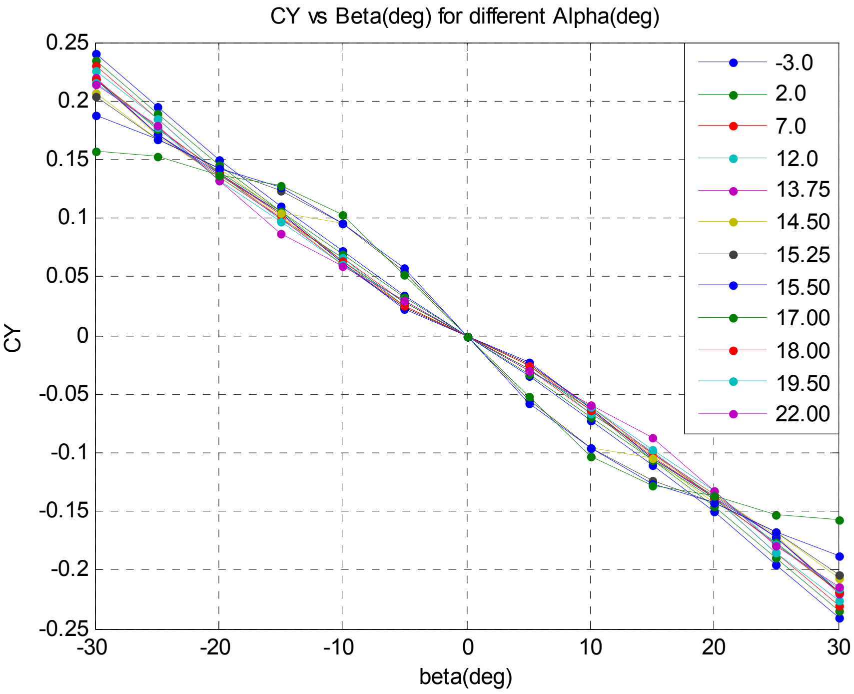

Figure 2.9: Side force coefficient data

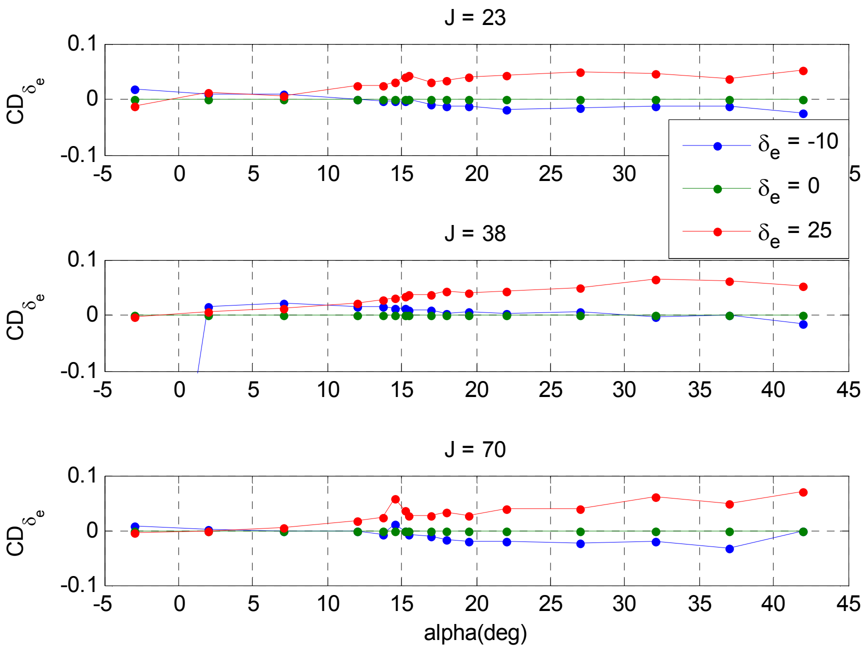

Figure 2.10: Elevator Drag force coefficient data

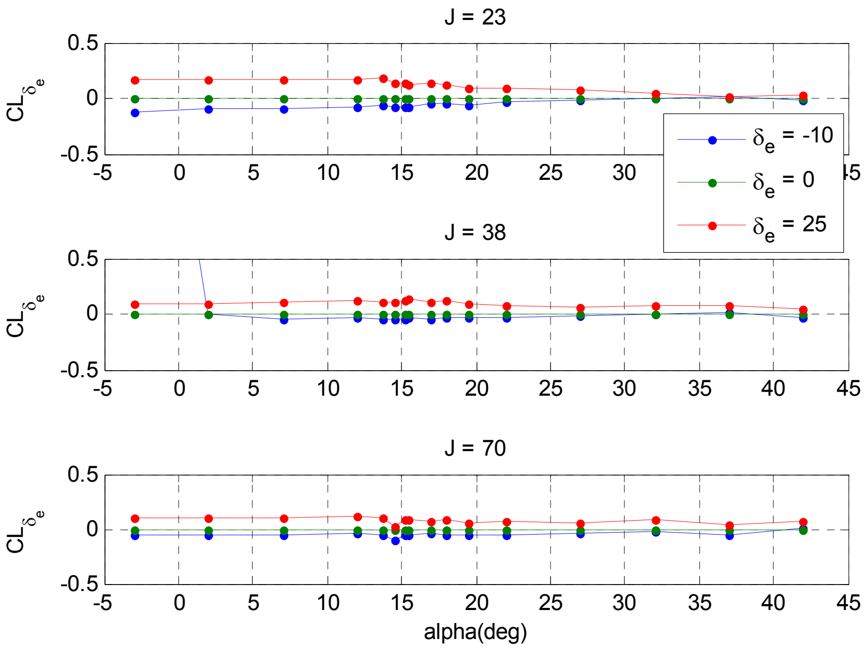

Figure 2.11: Elevator Lift force coefficient data

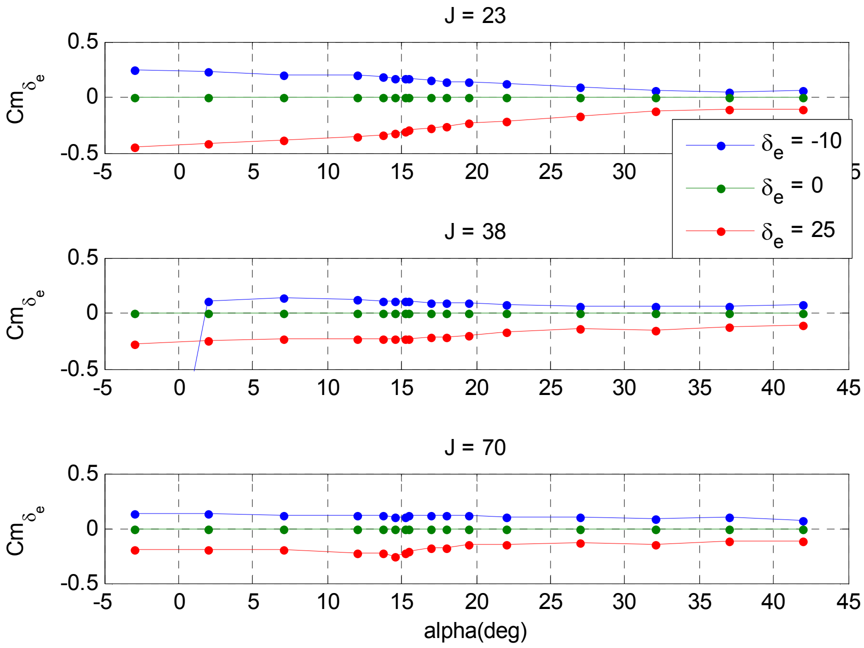

Figure 2.12: Elevator pitching moment coefficient data

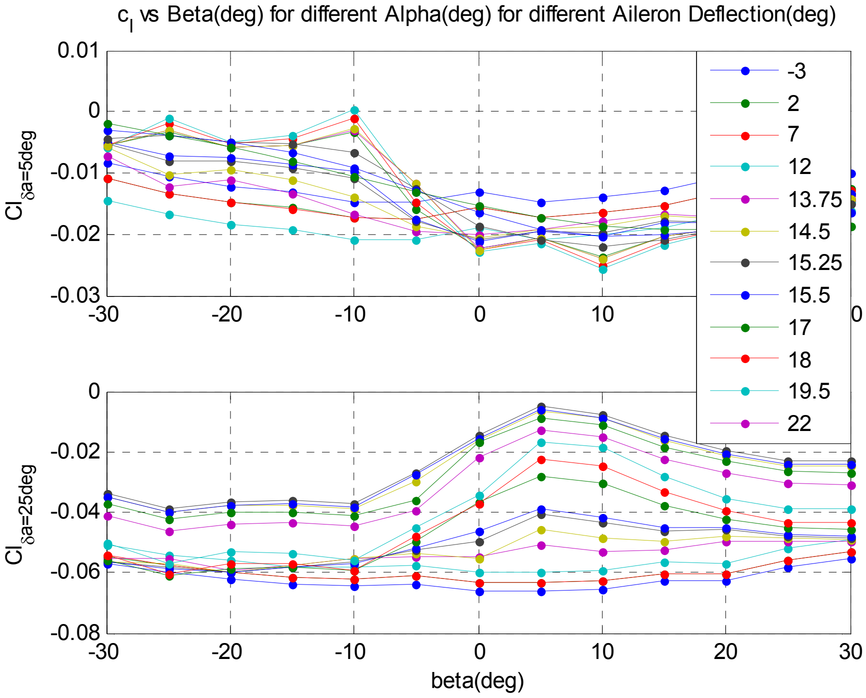

Figure 2.13: Aileron rolling moment coefficient data

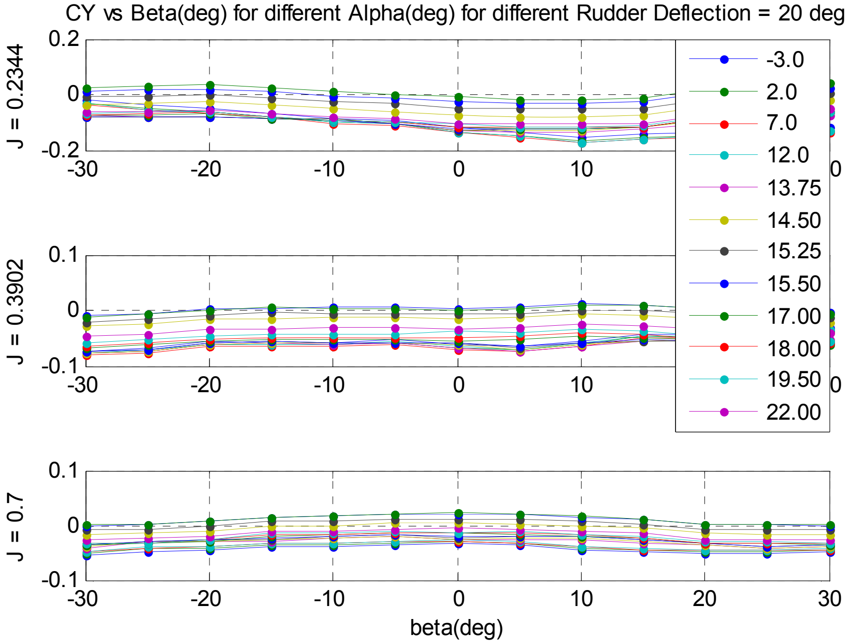

Figure 2.14: Rudder side force coefficient data

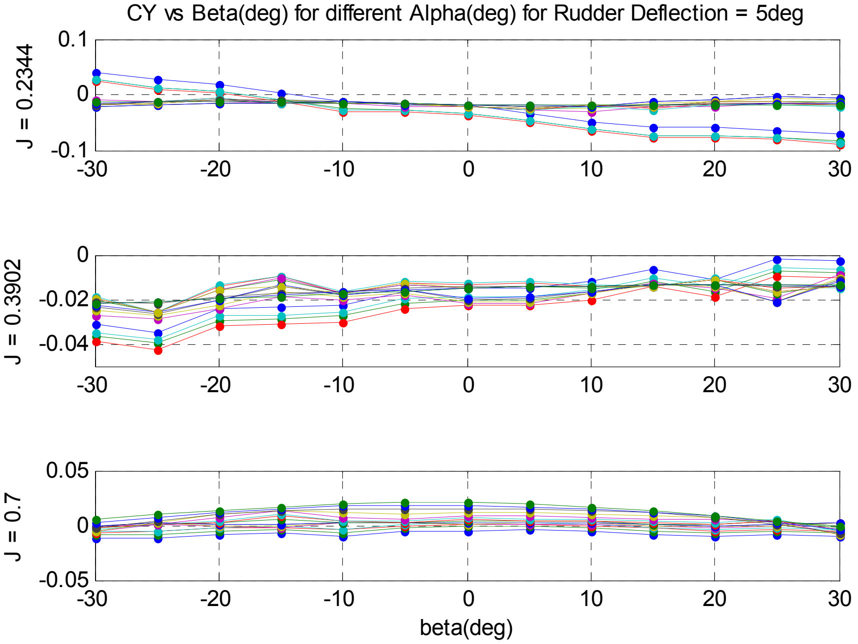

Figure 2.15: Rudder side force coefficient data

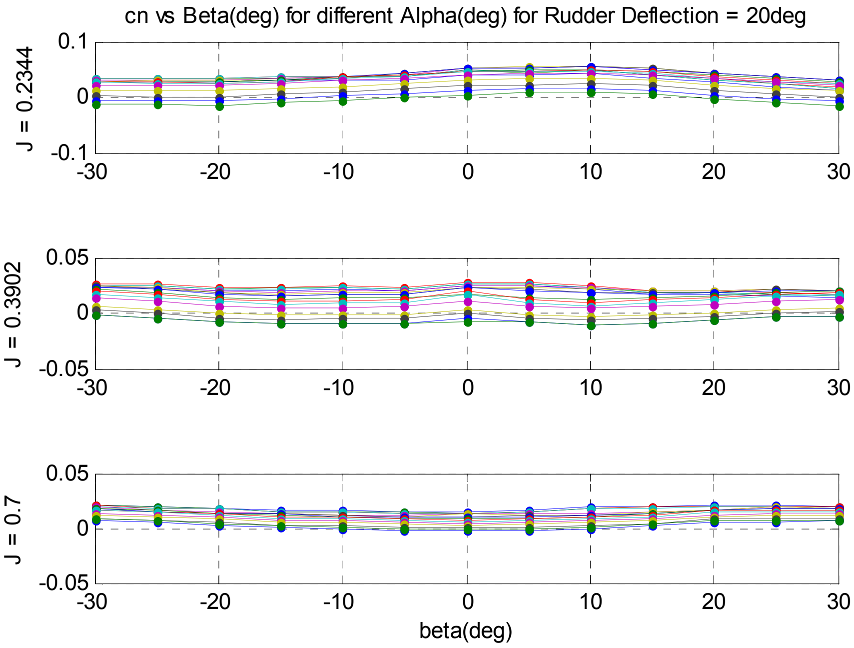

Figure 2.16: Rudder yawing moment coefficient data

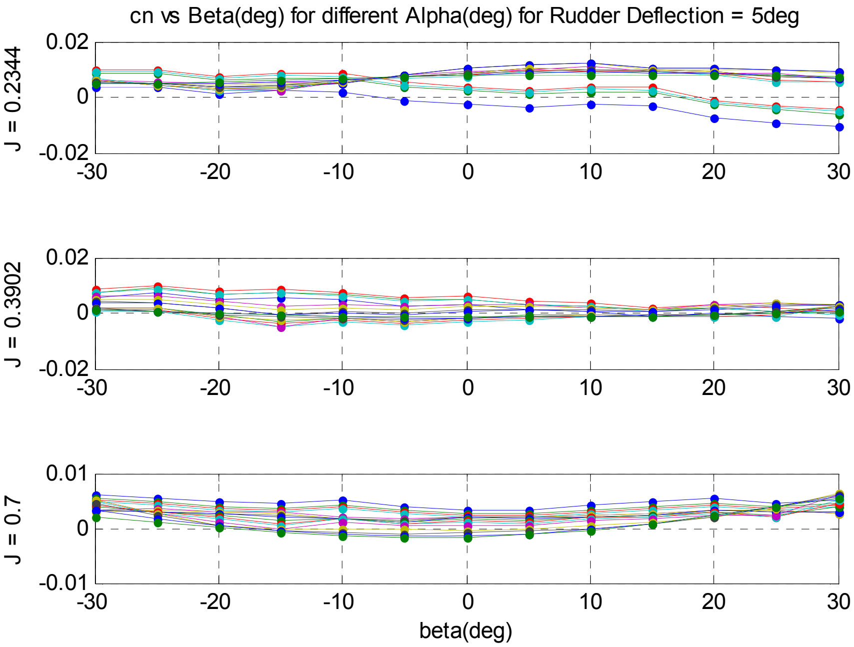

Figure 2.17: Rudder yawing moment coefficient data

Symmetry is assumed about the xz plane for FASER UAV, hence $\mathrm{I}_{xy} = \mathrm{I}_{xz} = \mathrm{I}_{zy} = 0$

$$\mathrm{I} = \begin{bmatrix} \mathrm{I}_{xx} & 0 & 0 \\ 0 & \mathrm{I}_{yy} & 0 \\ 0 & 0 & \mathrm{I}_{zz} \end{bmatrix} \tag{2. 26}$$

Table 2.3: Inertia Data

I_{xx}(kgm^2)	I_{yy}(kgm^2)	I_{zz}(kgm^2)	I_{p}(kgm^2)
0.8658	1.0095	1.7005	4.1935e-4

2.2.3 Propulsion Model

The propulsion system describes the functioning between electric motor and propeller dynamics. The conservation of angular momentum gives the propulsion dynamics as [**30**]:

$$(\mathrm{I}_{motor} + \mathrm{I}_{propeller})\dot{\omega}_p = T_{motor} - T_{propeller} \tag{2. 27}$$

where, I_{motor} = moment of inertia of rotating motor body(kgm^2)

I_{motor} = moment of inertia of propeller with spinner hub attachment (kgm^2)

I_{motor} = Output torque at motor shaft (Nm)

I_{motor} = Torque generated by propeller (Nm)

2.2.3.1 Propulsion Motor

The propulsion motor used is *E-flite Power 25 BL Outrunner Motor* [**30**]. The motor performance data showing the relationship between throttle stick input (δ_T) and output power (P_o) is given in figure 2.5.

The motor shaft torque, T_{motor} (*Nm*), is:

$$T_{motor} = \frac{P_0}{\omega_p} \tag{2. 28}$$

2.2.3.2 Propeller Characteristics

The propeller performance is generally characterized by 3 parameters [**30**]:

Advance ratio, *J*, given by:

$$J = \frac{\pi V_a}{\omega_p R} \tag{2. 29}$$

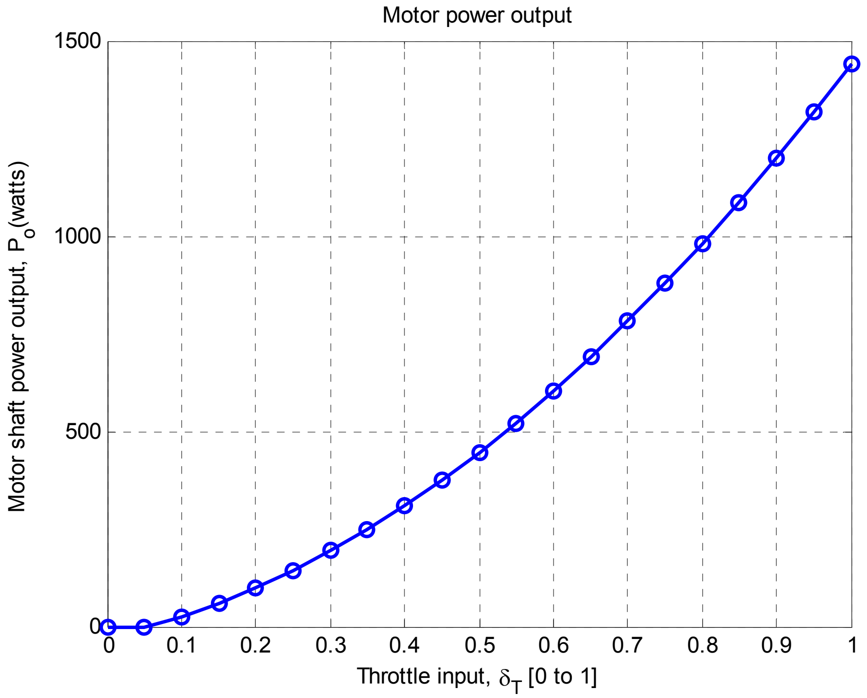

Figure 2.18: Motor Power Output

Coefficient of Thrust, C_T , given by

$$C_T = \frac{F_P \pi^2}{4\rho R^4 {\omega_p}^2} \tag{2.30}$$

Coefficient of Power, C_P , given by

$$C_P = \frac{T_P \pi^3}{4\rho R^5 {\omega_p}^2} \tag{2.31}$$

where

R (*m*) = diameter of the propeller

F_p (*N*) = propeller thrust

T_p (*Nm*) = propeller torque and

ρ (kg/m^3) = air density.

The propeller thrust (F_p) and moment (T_p) at different advance ratios condition used for simulation are given in figure 2.19 and 2.20 respectively.

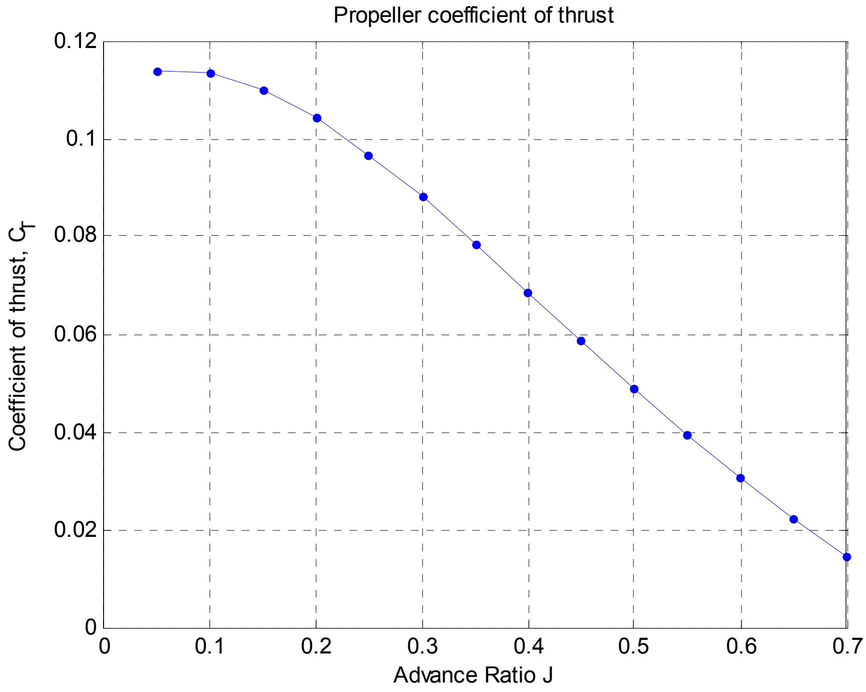

Figure 2.19: Propeller Coefficient of Thrust

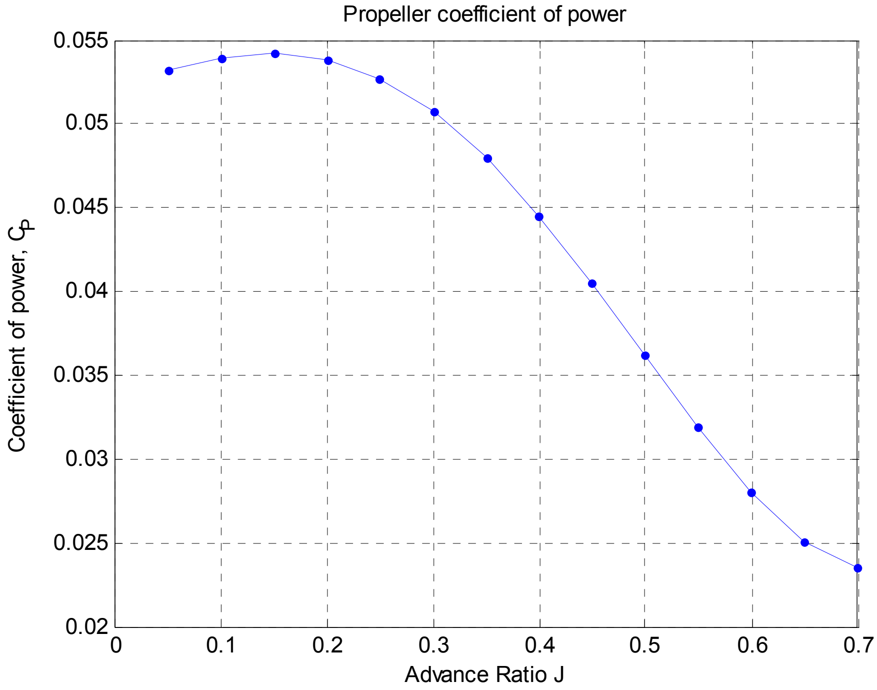

Figure 2.20: Propeller Coefficient of Power

2.2.4 Actuator Model

The UAV control surfaces have a bandwidth of 8 Hz [**30**]. The rotation rate is 150 *deg/s* and angular deflection saturation limits is ±25°.

Chapter 3: Linearization and Open Loop Response

Linearized model for fix wing UAVs are separated into longitudinal and lateral directional modes. This makes problem bit simplified for flight dynamics and control analysis [**30**]. The assumption is based on the fact that the two modes have negligible cross-coupling effect [**11**]. This assumption is applicable on the FASER UAV platform because of typical aileron, rudder and elevator control and also due to symmetry about xz plane causing minimum inertia cross-coupling.

For linear models extraction from the nonlinear simulation model, linearization is carried out about trim point and is shown in figure 3.1.

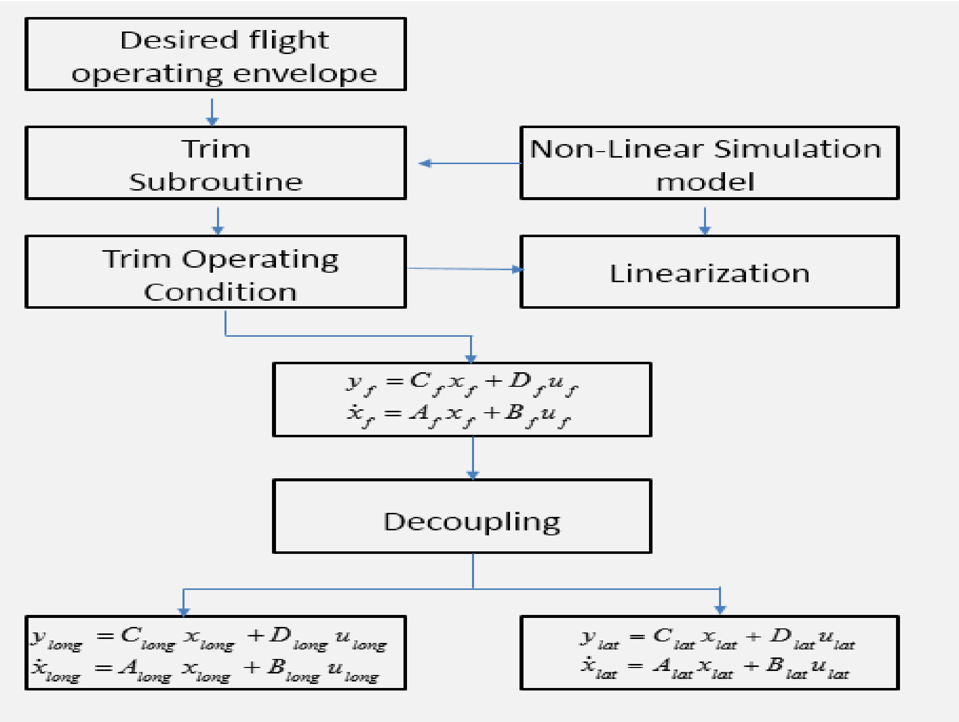

Figure 3.1: Procedure for Linearization and Decoupling of Longitudinal and Lateral modes

3.1 6DoF Linearization

Linear models of the FASER UAV are obtained after trimming at a desired flight operating envelop. Table 3.1 gives the desired flight operating envelope for the landing phase of the UAV. The linearized dynamic model is [**30**]:

$$\begin{aligned} y_f &= C_f x_f + D_f u_f \\ \dot{x}_f &= A_f x_f + B_f u_f \end{aligned} \tag{3. 1}$$

$\mathbf{x}_f$ = [u v w ϕ Θ ψ p q r h ω]^T

[u, v, w] = body velocities

[ϕ Θ ψ] = Euler angles

[p, q, r] = body angular rates

h = altitude

ωp = propeller rpm

uf = [δa, δe, δt ,δr]^T input vector

yf = [V_a β α ϕ Θ ψ h]^T

V_a is total velocity

β = sideslip angle

α = attack angle

Table 3.1: Linear Model Extraction Input Data

Airvelocity (m/s)	Altitude m)	Theta(deg)	ω (rpm)	δ_e(deg)	δ_T
20	30	5.9	899	-4.87	0.397

The output variables V_a, α and β are [**30**]:

$$\alpha = \tan^{-1}(\frac{w}{u}) \tag{3. 2}$$

$$\beta = \sin^{-1}(\frac{v}{V_a}) \tag{3. 3}$$

$$Va = \sqrt{(u^2 + v^2 + w^2)}$$

(3. 4)

3.1.1 Extraction of Longitudinal and Lateral Model

The longitudinal model consists of x and z body velocities (*u*, *w*), pitch angular rate *q*, pitch angle *Θ*, height *h* and propeller angular rotation ω_p state with control inputs as elevator (δ_e) and throttle (δ_T) [**30**]. Output variables are height *h*, velocity V_a, angle of attack *α*, pitch rate *q*, attitude angle *Θ.* Equation 3.5 The state-space representation is:

$$\begin{aligned} y_{long} &= C_{long} x_{long} + D_{long} u_{long} \\ \dot{x}_{long} &= A_{long} x_{long} + B_{long} u_{long} \end{aligned} \tag{3. 5}$$

Where

$x_{long} = [\, u \; w \; q \; \theta \; h \; \omega]^T$

$u_{long} = [\delta_e \;\; \delta_T]^T$

$y_{long} = [\, V_a \; \alpha \; q \; \theta \; h]^T$

$$\begin{Bmatrix} \dot{u} \\ \dot{w} \\ \dot{q} \\ \dot{\vartheta} \\ \dot{Z}_e \\ \dot{\omega} \end{Bmatrix} = \begin{bmatrix} -0.3184 & 0.9496 & -2.063 & -9.753 & 9.683\text{e-}005 & 0.007117 \\ -0.3984 & -5.615 & 19.89 & -1.011 & -0.0009339 & 0 \\ 0.3248 & -1.493 & -6.871 & 0 & -2.683\text{e-}016 & -0.003762 \\ 0 & 0 & 1 & 0 & 0 & 0 \\ -0.1031 & 0.9947 & 0 & -20 & 0 & 0 \\ 78.12 & 8.099 & 0 & 0 & -0.07804 & -4.458 \end{bmatrix} \begin{Bmatrix} u \\ w \\ q \\ \vartheta \\ Ze \\ \omega \end{Bmatrix} + \begin{bmatrix} 0.707 & 0 \\ -8.052 & 0 \\ -58.08 & 0 \\ 0 & 0 \\ 0 & 0 \\ 0 & 3323 \end{bmatrix} \{\delta_e \quad \delta_T\}$$

$$\begin{Bmatrix} V_a \\ \alpha \\ q \\ \vartheta \\ h \end{Bmatrix} = \begin{bmatrix} 0.9947 & 0.1031 & 0 & 0 & 0 & 0 \\ -0.005156 & 0.04973 & 0 & 0 & 0 & 0 \\ 0 & 0 & 1 & 0 & 0 & 0 \\ 0 & 0 & 0 & 1 & 0 & 0 \\ 0 & 0 & 0 & 0 & -1 & 0 \end{bmatrix} \begin{Bmatrix} u \\ w \\ q \\ \vartheta \\ Ze \\ \omega \end{Bmatrix} + \begin{bmatrix} 0 & 0 \\ 0 & 0 \\ 0 & 0 \\ 0 & 0 \\ 0 & 0 \end{bmatrix} \{\delta_e \quad \delta_T\}$$

The longitudinal motion is composed of [**30**]

- Short period mode
- Phugoid mode

The short period oscillatory mode is marked with relatively high damping and natural frequency and effects the angle of attack and the pitch angle at constant velocity. Phugoid mode consists of relatively low damping and low natural frequency and variation is in velocity at constant angle of attack. A_{long} matrix singular values depicts the longitudinal dynamic.

Table 3.2: Longitudinal mode characteristics

	Root Location	**Natural Frequency ω_n (rad/sec)**	**Damping Ratio ξ**
Short Period	-6.25 ± 5.49i	8.32	0.75
Phugoid	-0.00948 ± 0.523i	0.531	0.178

Table 3-2 describes the characteristic of longitudinal mode. With negative real parts of roots, both the modes are stable.

The lateral model contains lateral body velocity *v*, roll and yaw body angular rates (*p*, *r*) and roll and yaw attitude angles (*φ, ψ*). Aileron (δ_a) and rudder (δ_r) are the control inputs. Sideslip angle β, roll and yaw angular rate (*p*, *r*), roll and yaw attitude angle (*φ, ψ*) are the measured outputs [**30**]. Lateral linear model equation is

$$\begin{aligned} y_{lat} &= C_{lat}x_{lat} + D_{lat}u_{lat} \\ \dot{x}_{lat} &= A_{lat}x_{lat} + B_{lat}u_{lat} \end{aligned} \qquad (3.\ 6)$$

where

$x_{lat} = [\ v\ \ p\ \ r\ \ \phi\ \ \psi]^T$

$u_{lat} = [\delta_a\ \ \delta_r]^T$

$y_{lat} = [\ \beta\ \ p\ r\ \phi\ \psi]^T$

$$\begin{Bmatrix} \dot{v} \\ \dot{p} \\ \dot{r} \\ \dot{\phi} \\ \dot{\psi} \end{Bmatrix} = \begin{bmatrix} -0.419 & 2.053 & -19.53 & 9.753 & 0 \\ -1.536 & -8.377 & 2.325 & 0 & 0 \\ 0.5715 & 0.4601 & -1.515 & 0 & 0 \\ 0 & 1 & 0.1037 & 0 & 0 \\ 0 & 0 & 1.005 & 0 & 0 \end{bmatrix} \begin{Bmatrix} v \\ p \\ r \\ \phi \\ \psi \end{Bmatrix} + \begin{bmatrix} 0 & -0.07984 \\ -76.82 & 1.268 \\ 8.575 & -5.724 \\ 0 & 0 \\ 0 & 0 \end{bmatrix} \begin{Bmatrix} \delta_a & \delta_r \end{Bmatrix}$$

$$\begin{Bmatrix} \beta \\ p \\ r \\ \phi \\ \psi \end{Bmatrix} = \begin{bmatrix} 0.05 & 0 & 0 & 0 & 0 \\ 0 & 1 & 0 & 0 & 0 \\ 0 & 0 & 1 & 0 & 0 \\ 0 & 0 & 0 & 1 & 0 \\ 0 & 0 & 0 & 0 & 1 \end{bmatrix} \begin{Bmatrix} v \\ p \\ r \\ \phi \\ \psi \end{Bmatrix} + \begin{bmatrix} 0 & 0 \\ 0 & 0 \\ 0 & 0 \\ 0 & 0 \\ 0 & 0 \end{bmatrix} \begin{Bmatrix} \delta_a & \delta_r \end{Bmatrix}$$

The lateral modes are spiral mode, roll subsidence mode and the Dutch-roll mode. The spiral mode is a slow mode and generates yawing at nearly zero sideslip with some roll angle. The roll subsidence mode is concerned with roll angle dynamic response. The Dutch-roll mode is oscillatory mode and is a mixture of roll, yaw and sideslip. Eigenvalues of the A_{lat} matrix contain lateral modes of the system. Dutch-roll mode is stable too and its characteristic is shown in Table 3.3. Table 3.4 shows characteristics for roll and spiral mode which are stable.

Table 3.3: Dutch Roll mode characteristics

	Root Location	Natural Frequency ω_n (rad/sec)	Damping Ratio ξ
Dutch Roll Mode	-1.06e ± 3.33i	3.50	0.304

Table 3.4: Spiral mode and Roll Subsidance mode characteristics

	Root Location	Time Constant (s)
Spiral Mode	0.0564	17.73
Roll Subsidence Mode	8.13	0.123

3.2 Open Loop Simulation

Figure 3.2 – 3.6 represents longitudinal plane response to a 1° δ_e step input. Figure 3.7 – 3.11 represents lateral plane response to 1° δ_a step input.

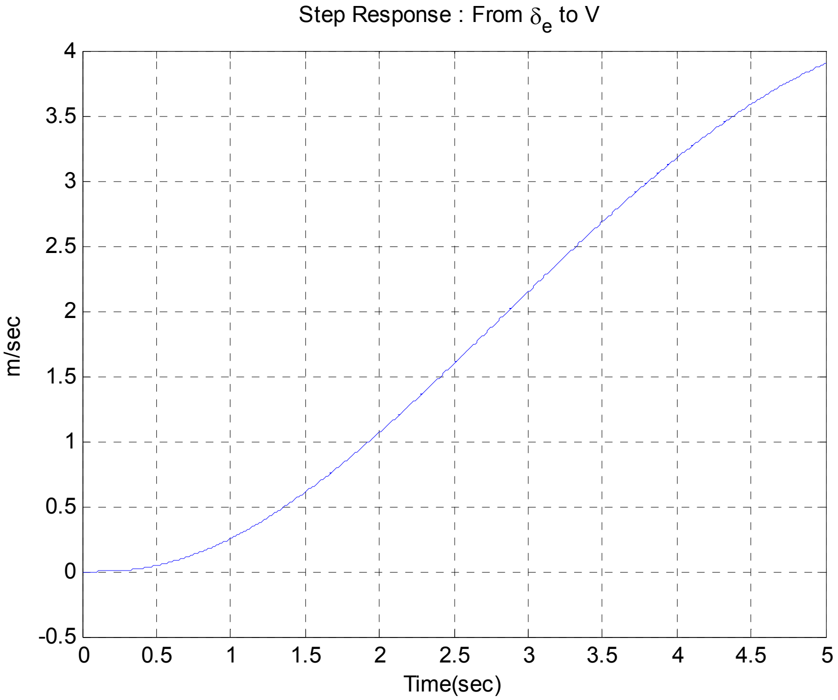

Figure 3.2: Forward velocity openloop step response for δ_e = 1°

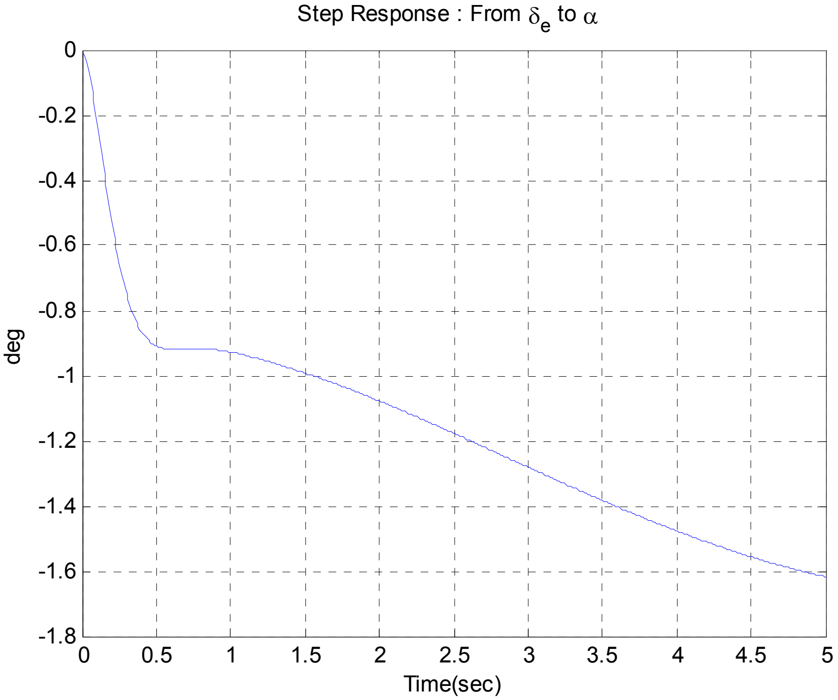

Figure 3.3: Angle of attack openloop step response for δ_e = 1°

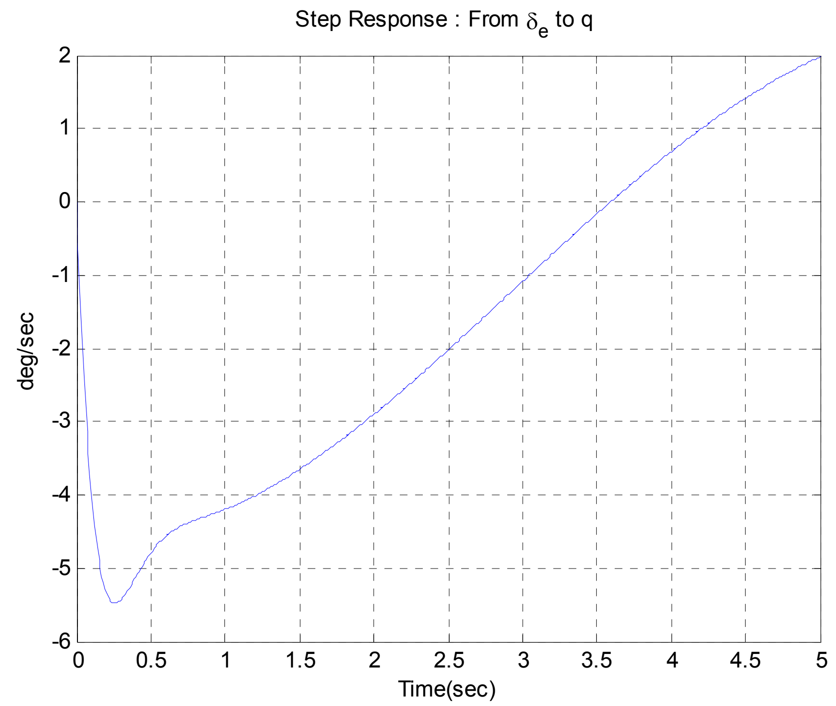

Figure 3.4: Pitch rate openloop step response for $\delta_e = 1^o$

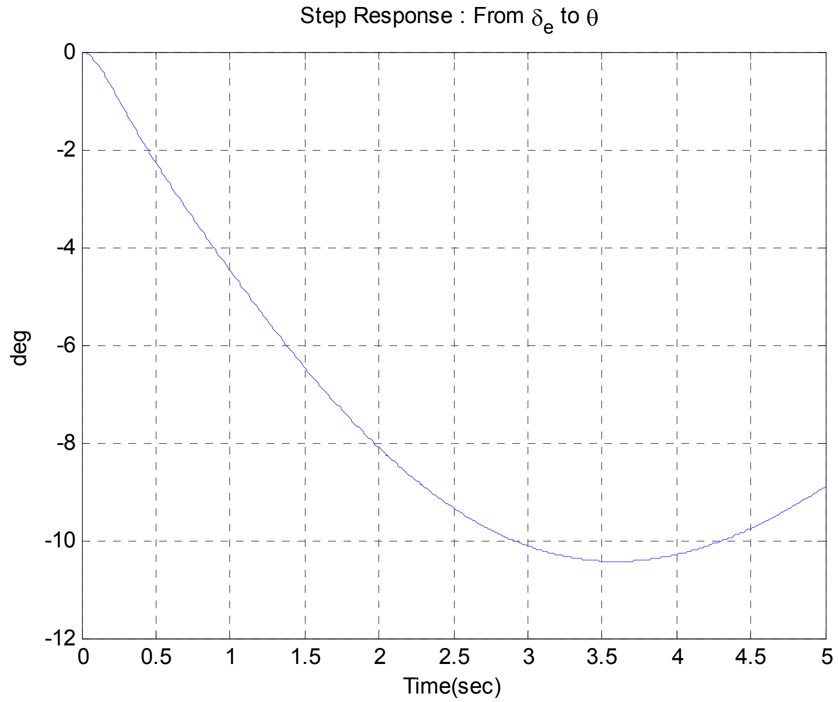

Figure 3.5: Pitch angle openloop step response for $\delta_e = 1^o$

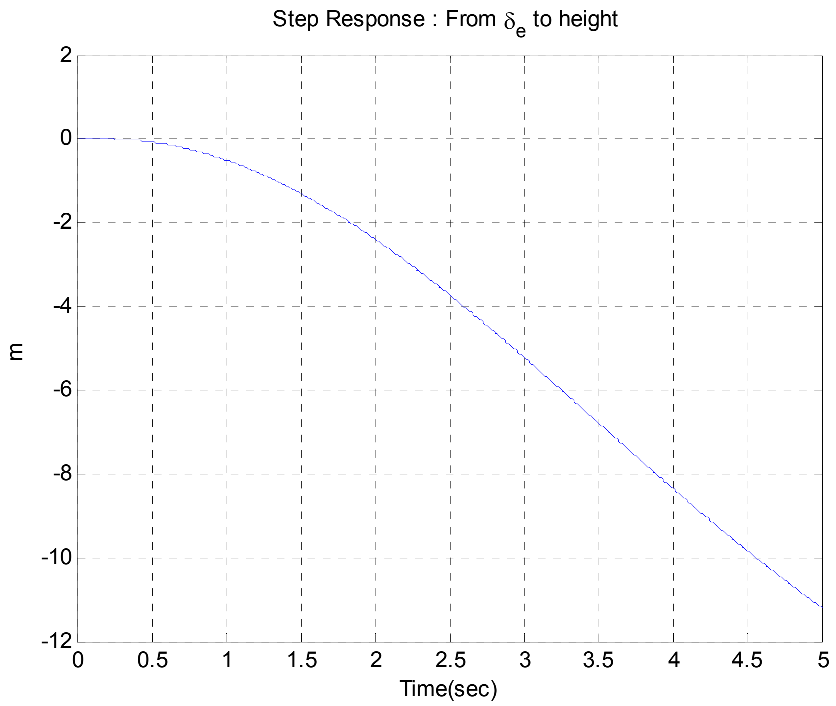

Figure 3.6: Height openloop step response for $\delta_e = 1^o$

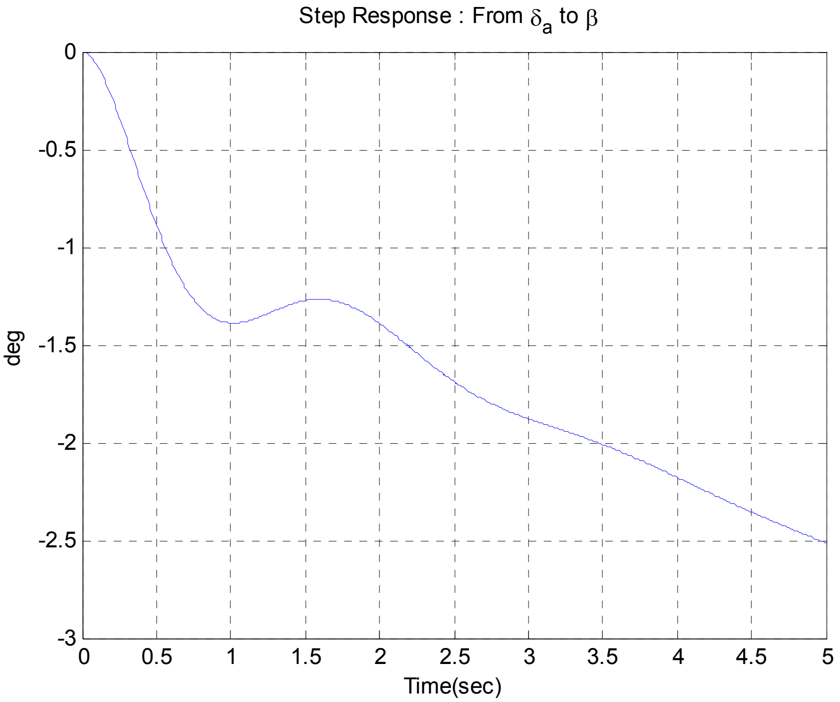

#

Figure 3.7: Beta openloop step response for $\delta_a = 1^o$

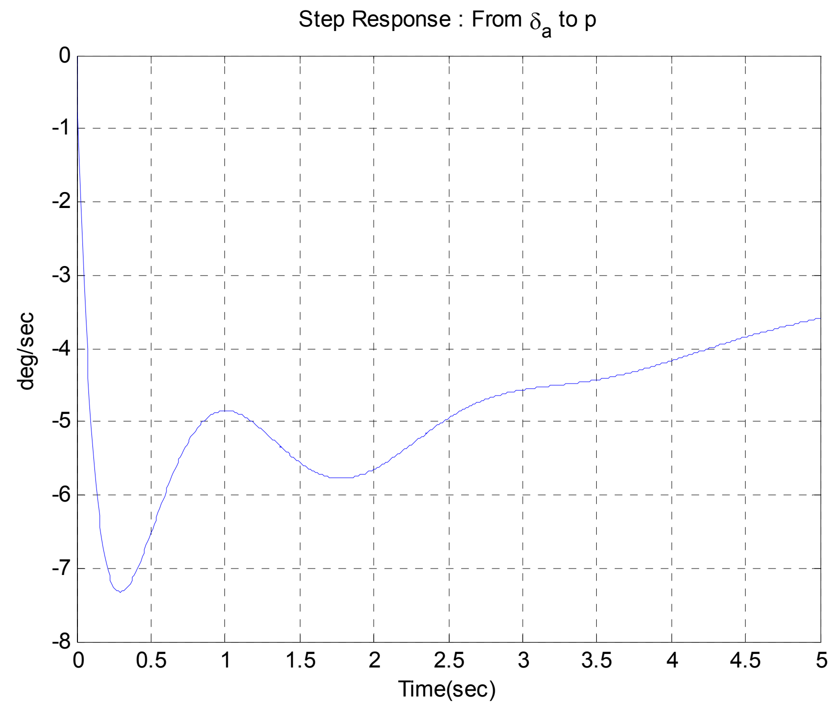

#

Figure 3.8: Roll rate openloop step response for $\delta_a = 1°$

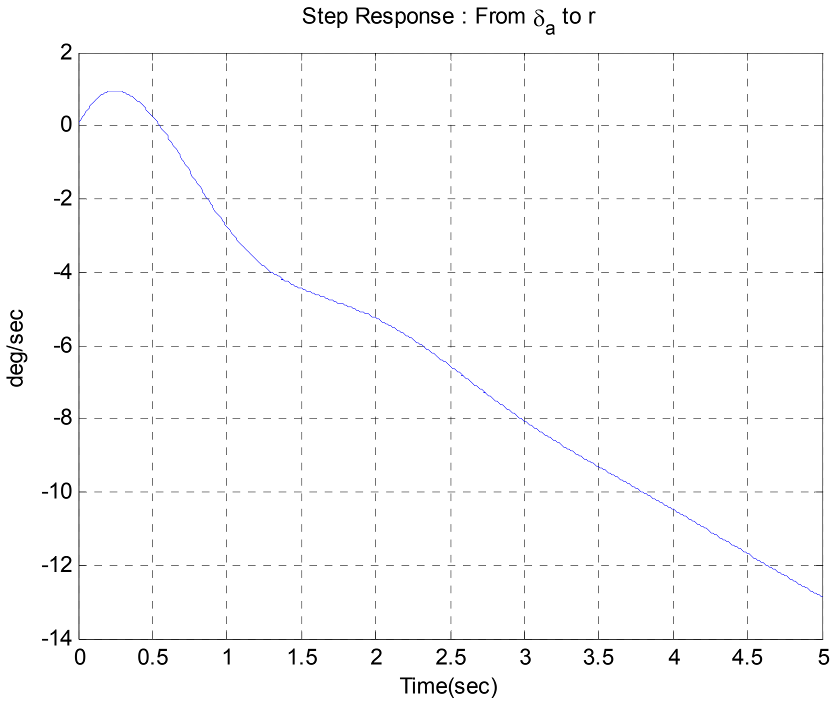

#

Figure 3.9: Yaw rate openloop step response for $\delta_a = 1°$

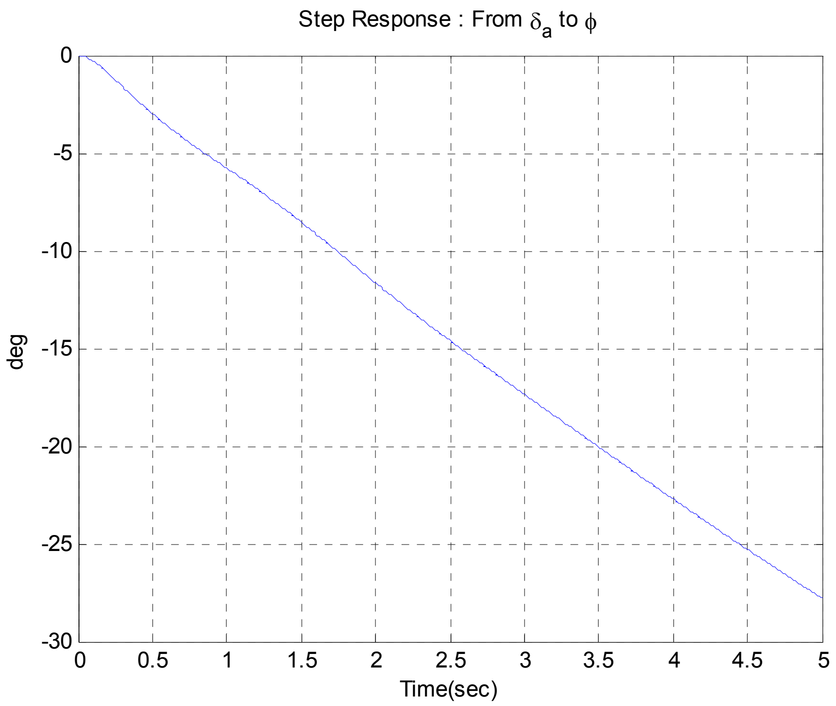

#

Figure 3.10: phi angle openloop step response for $\delta_a = 1^o$

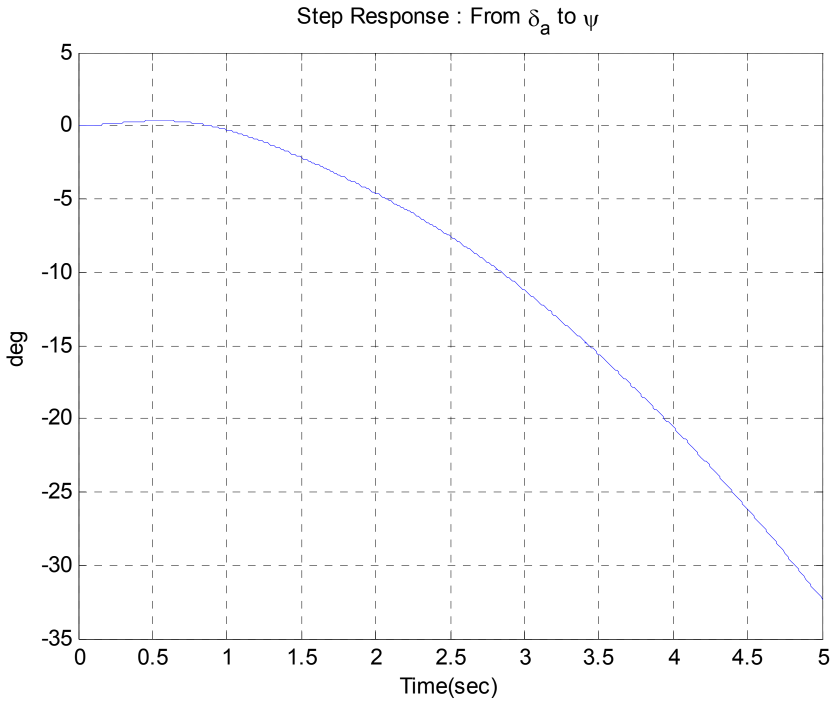

#

Figure 3.11: Yaw angle openloop step response for $\delta_a = 1^o$

Chapter 4: Landing Flight Phase

The anatomy of landing flight phase is discussed in this chapter along with existing autonomous landing strategies. UAV landing flight phase in longitudinal plane consists of distance to runway based trajectory command that can be either altitude profile or vertical velocity profile. The generated profile ensure smooth descend till touch down on runway. The forward velocity is required to be kept constant throughout this fight phase [**11**]. Figure 4.1 represents the generated landing trajectory.

Section 4.1 starts off with an overview of different landing phases in detail and defines the longitudinal landing trajectory parameters. Section 4.2 discusses the existing autonomous landing strategies. Section 4.3 discusses landing parameters calculation.

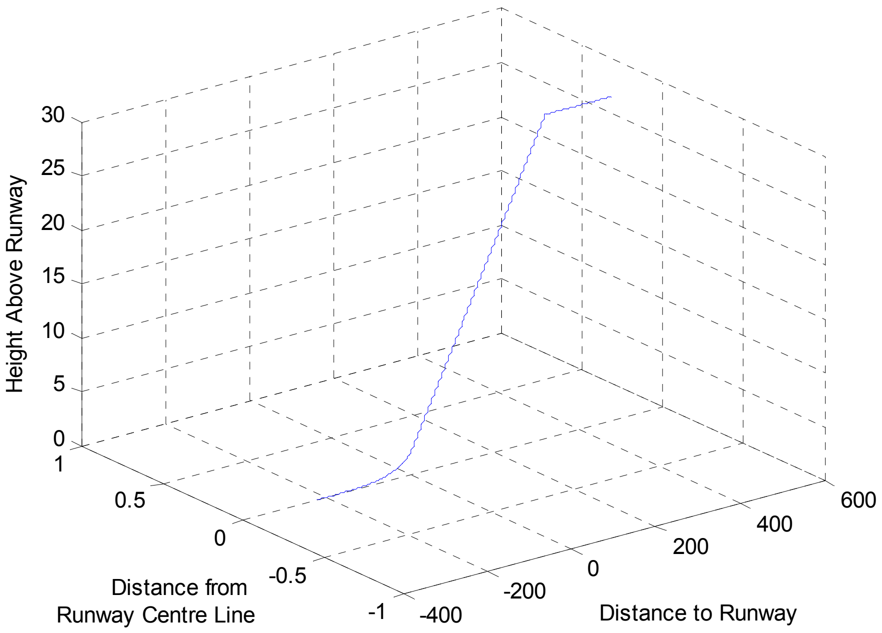

Figure 4.1: Landing Trajectory

4.1 Landing Flight Phase

Landing flight phase of UAV in longitudinal plane are depicted in figure 4.2 and can be generalized into three segments:

- Base leg
- Glide Phase
- Flare Phase

4.1.1 Base leg

It's the final leg of mission in which UAV starts its landing maneuver. The flight path of UAV must be aligned with the centerline of the runway. The landing velocity required during this leg is to be 1.3 times the stall velocity of the aircraft [**19**].

4.1.2 Glide Phase

At a certain threshold distance from the runway based on height above the runway, UAV starts a descending maneuver that is termed the Glide Phase. The descending flight path extends down towards a fix point on the runway which should be within the first one-third of the runway [**19**]. The UAV descends along an altitude profile which is a function of relative distance from runway at a fix flight path angle termed as glide slope angle γ [**11**].

The flight path angle and velocity are two important parameters that govern the glide phase trajectory. Short landing distance requires low velocity. High flight path angle allow obstacle avoidance and reduced landing time but higher downward velocity. Below a certain combination of desired flight path angle and velocity values, throttle setting become ineffective in controlling the forward velocity [**31**].

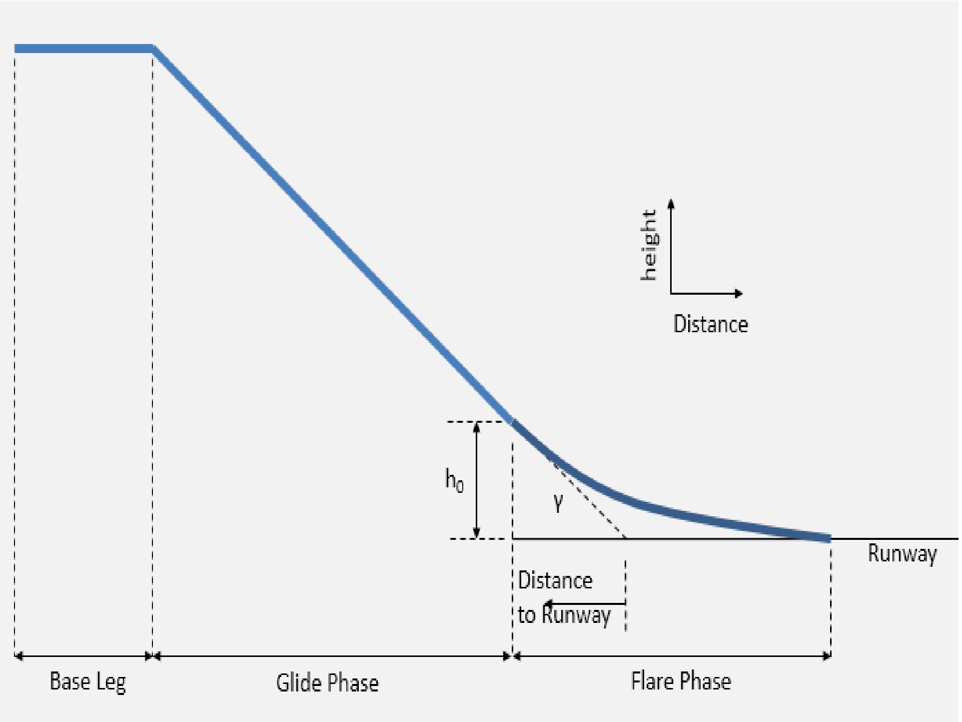

Figure 4.2: Longitudinal Plane Landing Trajectory

4.1.3 Flare Phase

At a certain height above runway, approach attitude acquired during glide phase is required to be transitioned in to landing attitude [**13**]. Landing attitude ensure UAV's main wheel touch down before nose wheel touch down [**20**]. The descending flight path of glide phase is gradually transformed to near parallel flight with the runway in an exponential fashion [**11**]. The trajectory is a function of forward velocity, flight path angle, flare initiation altitude and flare time [**31**]. This ensures lower touchdown impact velocity, governed by permissible structural loading on the landing gears. This phase terminates with UAV touching down on the runway.

4.2 Landing Schemes

Landing phase for UAV's in longitudinal plane is mainly concerned with generation of trajectory based on current position from runway in the form of height or vertical velocity profile. Existing schemes in aircraft trajectory generation and control text books and current level of research provides different strategies for generation of profiles. Trajectory algorithm methodology is limited by the availability of onboard sensors that can vary from GPS, IMU integrated GPS and DGPS [**18**, **19**]. In this section, the implemented glide phase scheme will be discussed. Brief description as well as mathematical background of GPS based flare phase schemes will be discussed, that will provide a base for comparison with proposed scheme in chapter 5.

4.2.1 Glide Phase

The UAV will be aligned with the runway if it starts tracking the glide slope. The glide-slope is a fictitious line at a fix angle connecting the UAV c.g with intended touchdown point [**20**]. The glide slope can be defined by two parameters

- Relative ground position difference between UAV and runway in longitudinal plane
- Glide Slope angle

$$h_{cmnd} = (\text{distancetorunway}) * \tan\gamma \qquad (4.\ 1)$$

During glide phase, the longitudinal landing accuracy is a function of estimated altitude error and the glide slope angle γ. Lower values of γ results in higher longitudinal landing error from the intended touchdown point but higher values of γ will reduce longitudinal error from intended touch down point at a cost of a high impact velocity [**19**].

4.2.2 Flare Phase

4.2.2.1 Scheme 1: Exponential Trajectory Profile Generation [11]

This scheme is a mathematical representation of aircraft pilot's response while performing a flare from glide mode to final touchdown on runway. The rate of descent response decreases in an exponential manner during flare which makes the aircraft fly an exponential path.

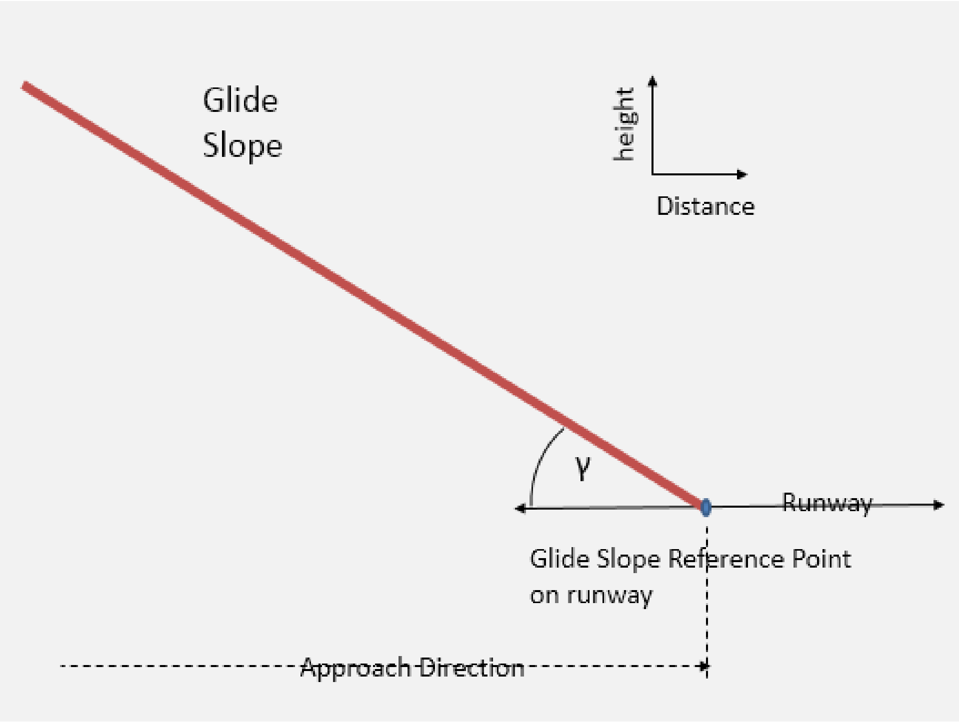

Figure 4.3: Glide Phase Trajectory

For UAV's, the same approach is employed by generating a distance from runway based exponential height or vertical velocity command from initiation of flare till touchdown.

$$h_{cmnd} = h_0 e^{-t/\tau} \tag{4. 2}$$

where h_0 = Flare initiation height

τ= exponential command time constant

Differentiating h_{cmnd} yields

$$\dot{h}_{cmnd} = -\frac{h_0}{\tau} e^{-t/\tau} = -\frac{h}{\tau} \tag{4. 3}$$

or at t = 0

$$\dot{h}(0) = -\frac{h_0}{\tau} \tag{4. 4}$$

the h_{cmnd} equation becomes

$$\dot{h}_{cmnd} = \dot{h}(0) e^{-t/\tau} \tag{4. 5}$$

Flare phase geometry can be shown as

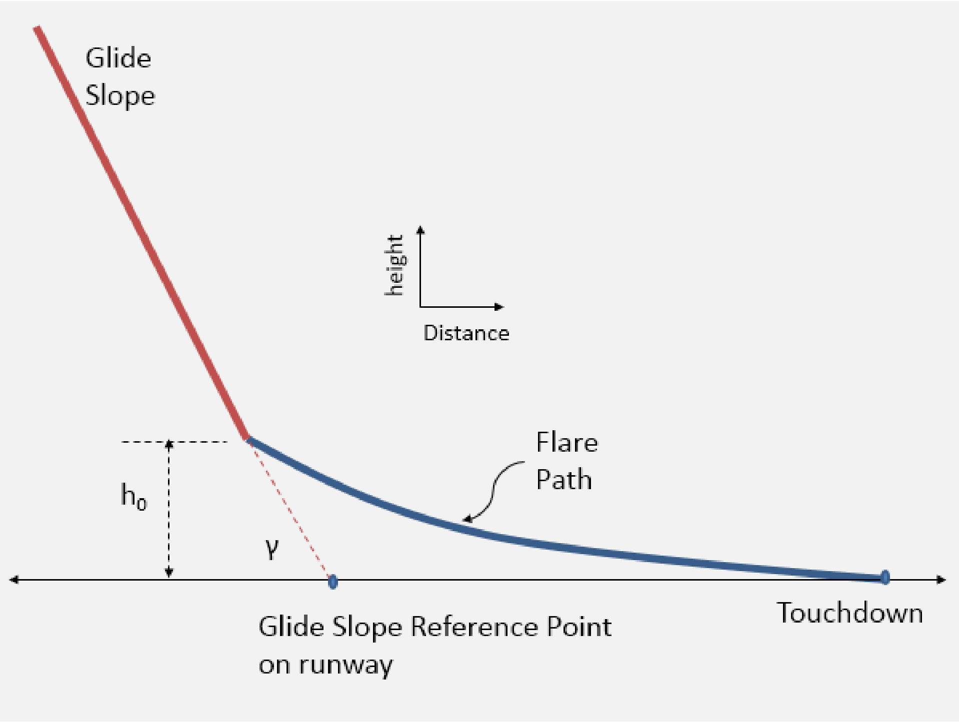

Figure 4.4: Landing Trajectory for scheme 1 [11]

The unknowns in h_{cmnd} equation are h_0 and τ can be determined by exploiting the fact that at flare initiation rate of descent $\dot{h}(0)$ is

$$\dot{h}(0) = V\sin(\gamma) \tag{4. 6}$$

where V = forward velocity

τ determines the distance to touchdown point from glide slope reference point on runway. Assuming it takes four time constant to touches down the ground distance during flare

$$(4\tau)(V) = d + R \tag{4. 7}$$

where R = distance on ground from flare initiation point to glide slope reference point on runway

d = distance on ground from glide slope reference point on runway to touchdown

4.2.2.2 Scheme 2: Exponential Trajectory Profile Generation with Touchdown at Intended Point with intended Vertical Speed [16]

This scheme is centered at formulation of exponential command based on [**11**] architecture. This scheme ensures height command generation that terminates on desired touch down point with desired touchdown downward velocity. Parameters are calculated through iteration of set of equations and convergence ensures a feasible set that ensures the desired results.

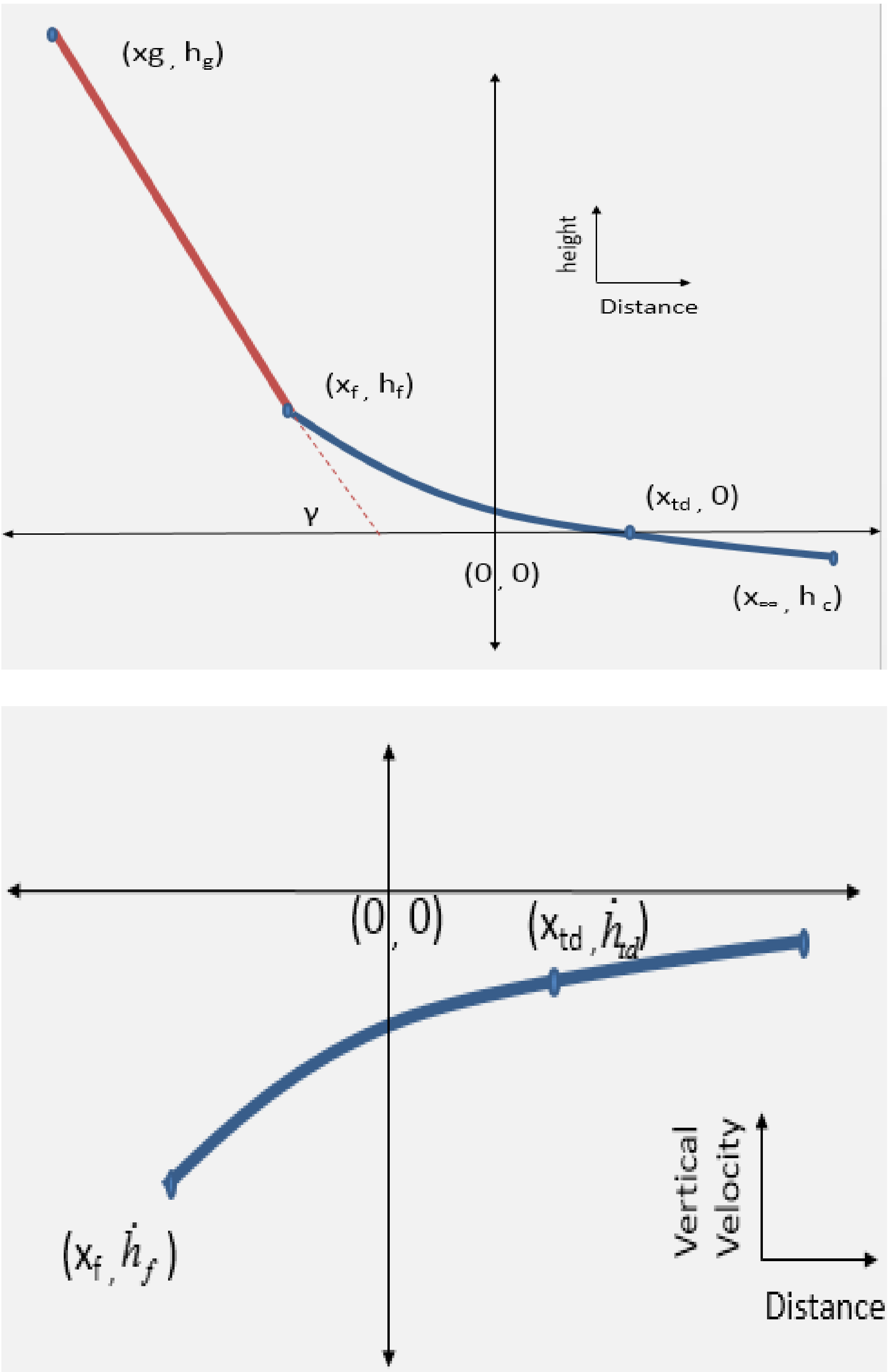

Figure 4.5: Landing Trajectory for scheme 2 [16]

At flare initiation point, the commanded height is

$$h_{cmnd} = -(x - x_{g0}) \tan \gamma \qquad (4.8)$$

Furthermore, the exponential height command profile during flare phase can be written as

$$h_{cmnd} = h_c + (h_f - h_c)e^{-K_x(x-x_f)} \tag{4. 9}$$

With the unknowns are flare initiation coordinates in longitudinal plane as h_f and x_f, final height below the ground h_c where flare trajectory should terminate and constant K_x.

These unknowns are found through imposition of certain constraints i.e.

- The height equation at coincident point between flare and glide slope i.e. $x = x_f$ is

$$h_f = -(x_f - x_{g0})\tan\gamma \tag{4. 10}$$

- The coincidence point between flare and glide slope have same slope i.e. at $x = x_f$,dh/dx is same

$$(h_f - h_c)K_x = \tan\gamma \tag{4. 11}$$

- At touch down point, flare height command should be zero i.e. $h_{cmnd} = 0$ at $x = x_{td}$

$$h_{cmnd} = 0 = h_c + (h_f - h_c)e^{-K_x(x_{td}-x_f)} \tag{4. 12}$$

- The touchdown vertical velocity should be equal to the specified sink rate i.e. $\dot{h}_{cmnd} = \dot{h}_{td}$ at $x = x_{td}$

$$\dot{h}_{cmnd} = \dot{h}_{td} = -(h_f - h_c)e^{-K_x(x_{td}-x_f)} \tag{4. 13}$$

4.2.2.3 Scheme 3: Exponential Height/Vertical Velocity Command with Time Constant Calculation based on Initial and Final Vertical Velocity [20]

This scheme is centered at formulation of exponential command based on [**11**] architecture. This scheme provides Time constant τ calculation based on flare initiation vertical velocity and intended touchdown velocity. This scheme doesn't ensure generated height command to touchdown at intended point because exponential command goes to zero at infinity.

Governing equation is

$$\dot{h}_{cmnd} = \dot{h}_o(0)e^{-\frac{t}{\tau}} \tag{4. 14}$$

Which in turn can be formulated at touch down point with $t = (x - x_{td})/V$ as

$$\dot{h}_{cmnd} = \dot{h}_{td} = \dot{h}_o(0)e^{-\frac{(x-xtd)}{V*\tau}} \tag{4. 15}$$

Solving this equation for time constant τ gives

$$\tau = \frac{-(x - x_{td})}{V * \ln\left[\frac{\dot{h}_{td}}{\dot{h}_o(0)}\right]} \tag{4. 16}$$

4.2.2.4 Scheme 4: Linear Height Profile [18]

This scheme is based on generation of distance to runway proportional linear height command during flare phase that in turns generate a constant descent rate. Flight path angle γ during flare phase is chosen such that $\gamma_{glide} > \gamma_{flare}$. Touch down velocity governs the structural impact criteria and increases the landing distance.

This scheme ensure height command termination at intended touch down point with intended touchdown sink rate.

The mathematical formulation of height command is

$$h_{cmnd} = (x - x_{td0}) \tan \gamma \tag{4. 17}$$

Which in turns gives vertical velocity command as

$$\dot{h}_{cmnd} = V * \tan \gamma \tag{4. 18}$$

4.3 Landing Parameter Calculation

4.3.1 Glide Phase

Short landing distance, short landing time and obstacle avoidance requires higher γ during glide. But higher γ causes higher rate of descent as well as high impact velocity at touchdown. Simulation were performed to evaluate value of γ at recommended landing velocity of $1.3xV_{stall}$ [**18**]. Forward velocity was tried to be controlled while altitude tracking at a certain γ angle was performed. The results are given in figure 4.7. It can be clearly observed that the velocity is uncontrollable above certain value of γ because engine throttle is already at its minimum. The glide slope angle was chose to be $\gamma = 5^o$ based on this analysis for landing velocity of 20m/sec.

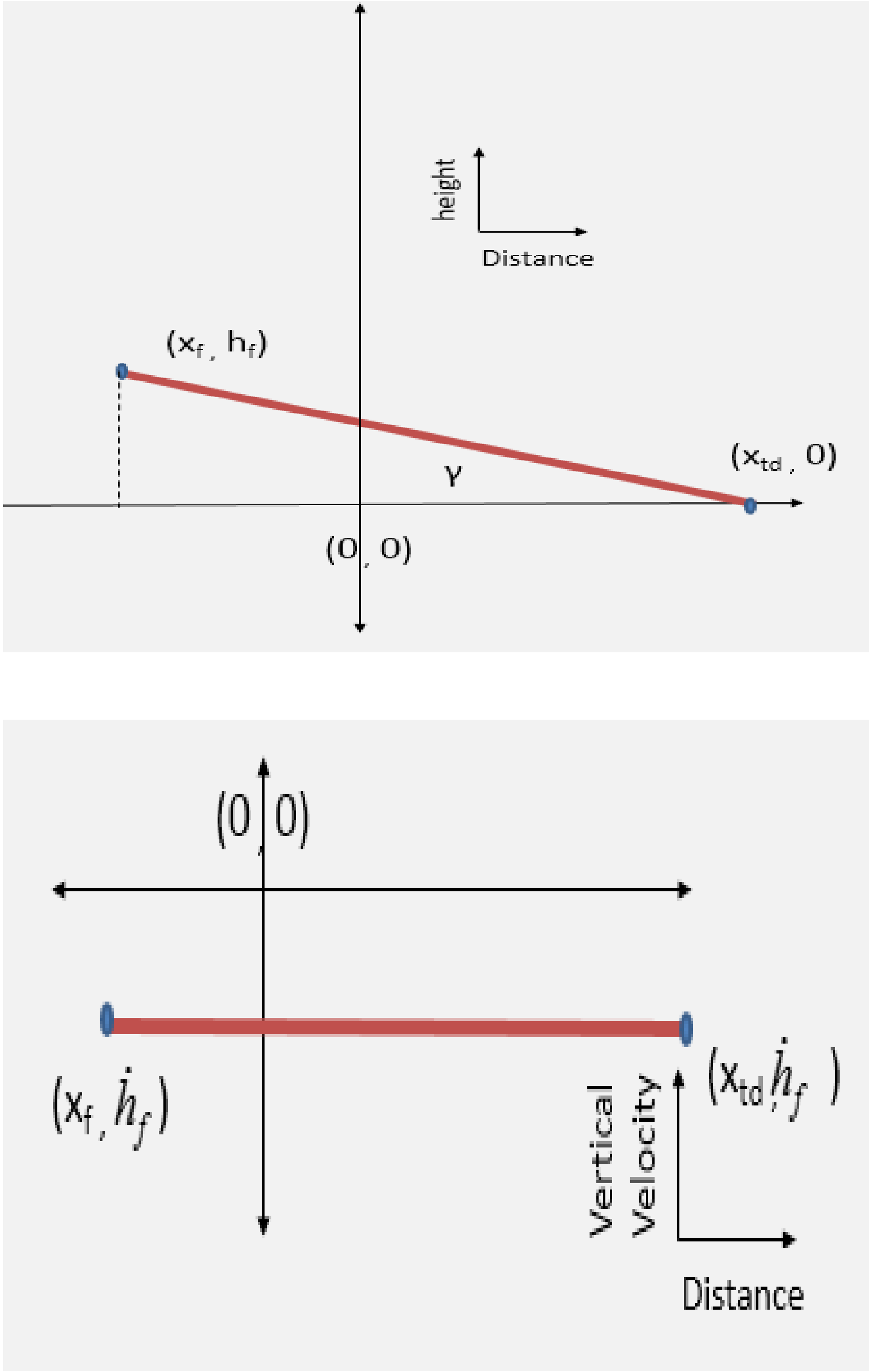

Figure 4.6: Landing Trajectory for scheme 4 [18]

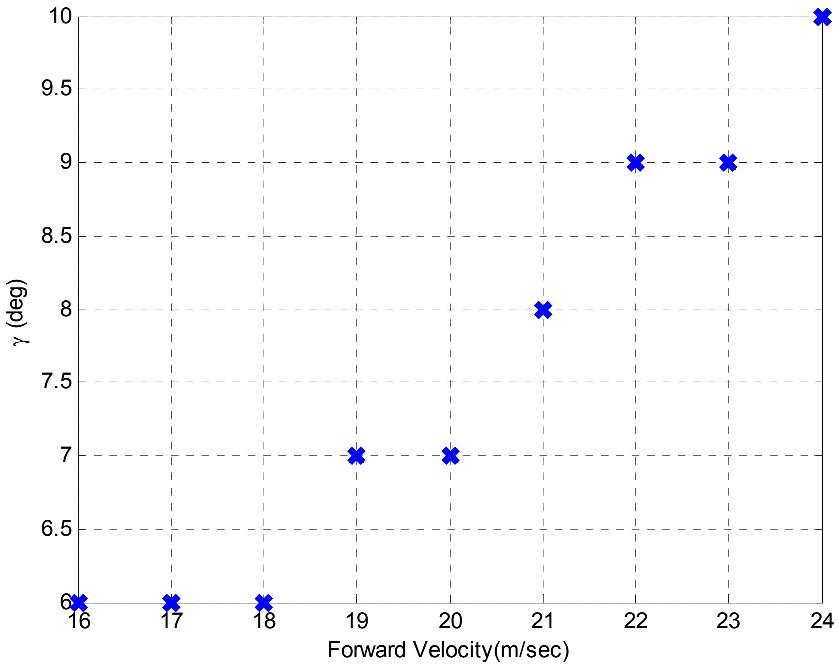

Figure 4.7: γ Angle for different landing Velocities

4.3.2 Flare Phase

Flare phase is all about distance required for landing and impact velocity. Parameter calculation was carried out for fix initial and final vertical velocity for flare phase using scheme 1 for flare initiation height. Distance required was evaluated for all schemes using this flare initiation height, initial and final vertical velocity.

Table 4.1: Flare Phase parameters

Flare Initiation Height h_o (m)	Time Constant τ(sec)
2.03	1.16

Chapter 5: Proposed Landing Scheme

Landing distance reduction is prime goal of flare phase maneuver while keeping the vertical velocity within the structural impact bound. This chapter discusses proposed flare scheme, its implementation and online calculation and comparison with existing schemes.

Section 5.1 present proposed flare phase scheme and its mathematical background. Implementation and online calculation is discussed in Section 5.2. Comparison results are presented in Section 5.3

5.1 Proposed Flare Phase Scheme

Instead of using a distance to runway based trajectory command in height or vertical velocity based on exponential profile, polynomial expressions can be evaluated. A linear profile evaluated in vertical velocity command results in parabolic command in height profile. This idea was utilized in this scheme.

$$\dot{h}_{cmnd} = mt + c \tag{5. 1}$$

Integrating the above expression

$$\int_{htd}^{hf} dh = \int_{ttd}^{tf} (mt + c)dt \tag{5. 2}$$

At touchdown distance to runway becomes zero and h_{td} = 0, so t_{td} = 0 because $t = \frac{\text{distanceto runway}}{V}$

Therefore the height expression is

$$h_f = t_f\left(\frac{m}{2}t_f + c\right) \tag{5. 3}$$

Calculation of h_f, m and c are based on chosen relative distance between flare initiation and touch down, forward velocity during landing phase and γ angle.

$$m = \frac{\dot{h}_f - \dot{h}_{td}}{t_f} \tag{5. 4}$$

$$c = \dot{h}_{td} \tag{5. 5}$$

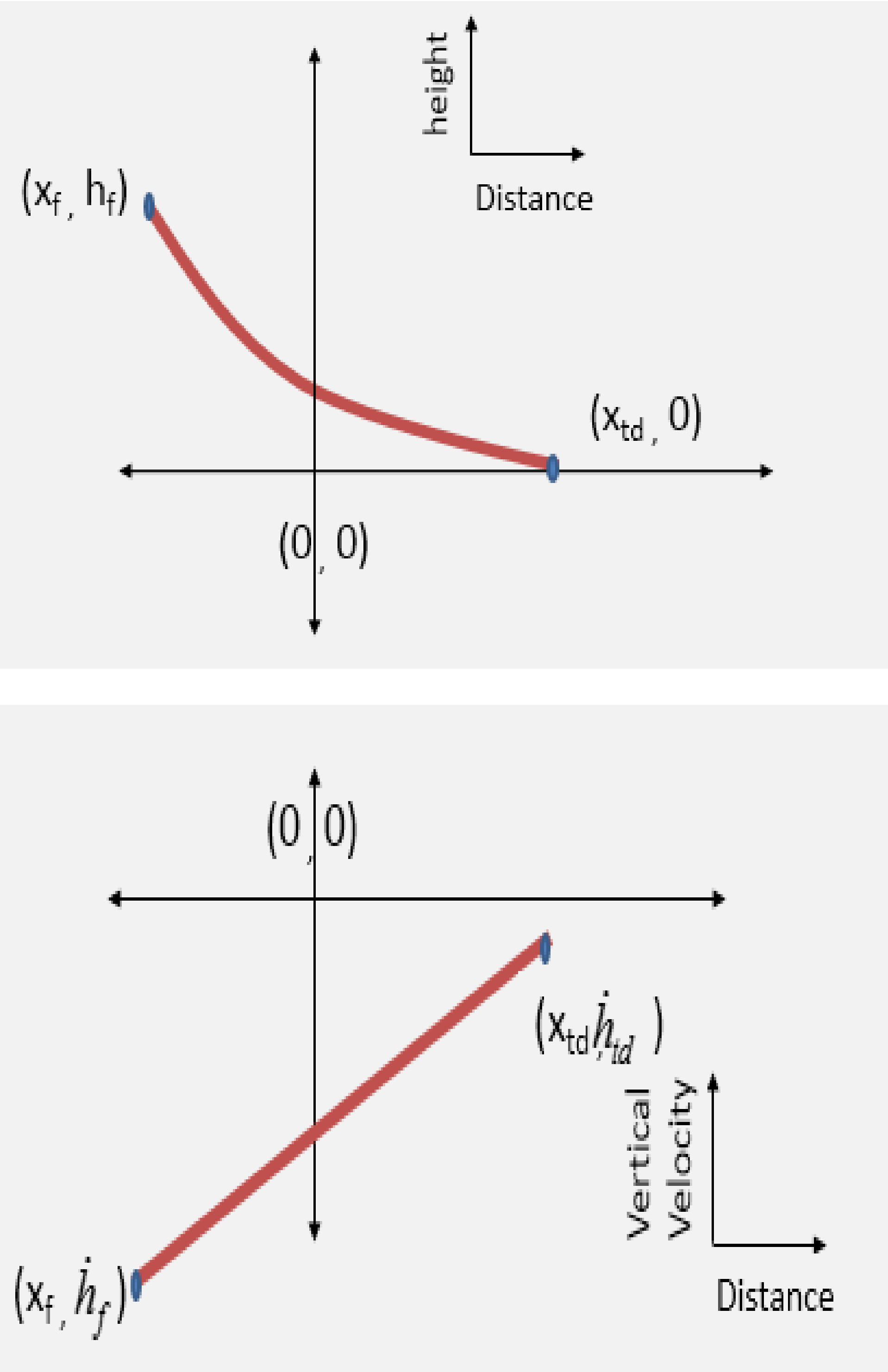

Figure 5.1: Proposed Landing Scheme Trajectory

5.2 Implementation and Online computation

The purposed scheme is implemented in control software block of simulation in c-language as shown in figure 2.2. Both pre-calculated parameters and online computation options are made available. Since the flare initiation height, γ angle, $\dot{h}_{td}$ are fix parameters, the variables to be calculated $\dot{h}_f$ from rate of change of trajectory command in glide phase, m and c from distance to intended touchdown point. The block diagram for online calculation is given in figure 5.2 and its evaluation is shown in figure 5.3 - 5.4.

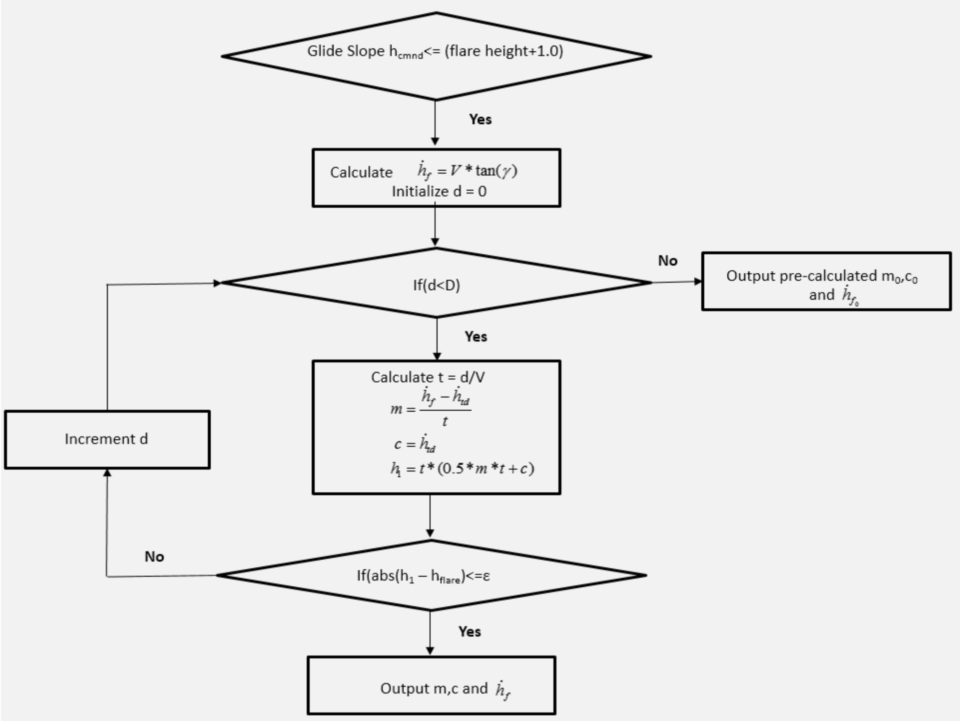

Figure 5.2: Proposed Algorithm's Online Computation Flow Chart

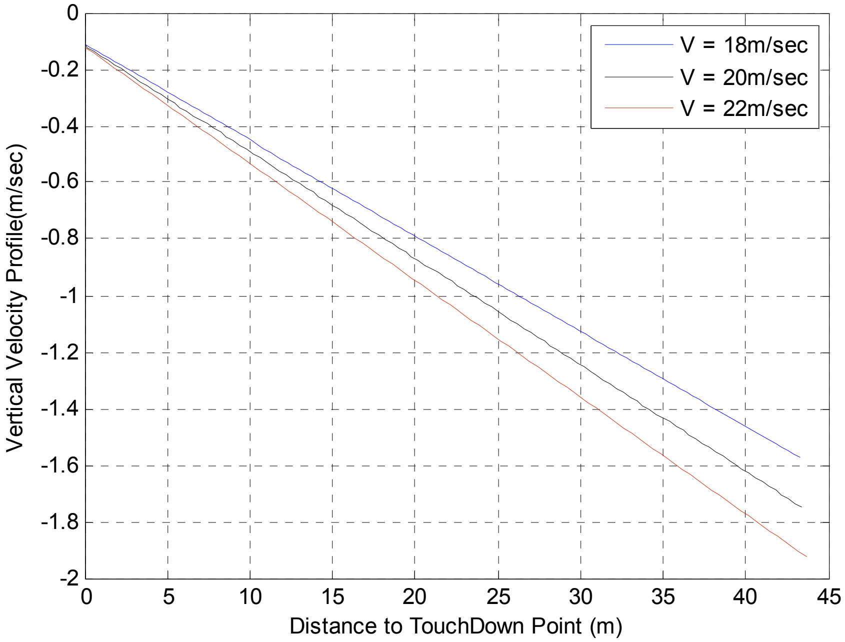

Figure 5.3: Proposed algorithm online computation vertical velocity results

The proposed algorithm's online computation requires two linear equation to be solved iteratively. Distance is the varying parameter and search is on getting the resulting height to be within the bound of flare height. Thus, the computational cost for this algorithm is quite low because of simplicity of this algorithm as compared with scheme 2 in chapter 4 which requires four nonlinear equations to be solved iteratively while giving the same qualitative output as the proposed algorithm, by ensuring touchdown at intended point with intended vertical velocity.

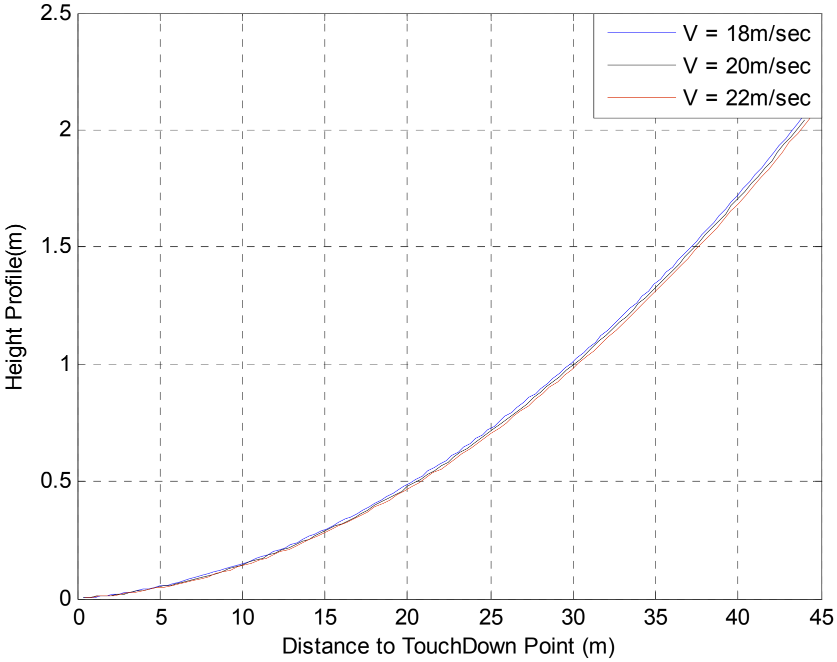

Figure 5.4: Proposed algorithm online computation height results

5.3 Results

Performance of flare phase command generation schemes discussed in section 4.2.2 are compared with proposed scheme. These schemes are evaluated for distance required for generated command to make height to decay to zero, starting with initial flare vertical velocity and ensuring touch down vertical velocity.

Table 5.1: Fixed parameters for comparison of trajectory generation algorithms

Flight Path Angle γ (deg)	$\dot{h}_{td}$ **(m/sec)**
5	-0.1

Four cases were designed to evaluate the distance output of the proposed scheme. These cases have different forward velocity and flare initiation height.

Table 5.2: Test cases for evaluation and comparison of trajectory generation algorithms

	Velocity (m/sec)	Flare Initiation Height (m)	$\dot{h}_f$ (m/sec)
Case 1	20	2.03	-1.74
Case 2	20	2.61	-1.74
Case 3	22	2.03	-1.91
Case 4	18	2.61	-1.56

Table 5.3: Comparison of distance output for trajectory generation schemes

	Scheme 1	Scheme 2	Scheme 3	Scheme 4	Proposed Scheme
Case 1	89.2	48.75	46.2	387.0	44.0
Case 2	115.4	60.26	65.0	498.0	57.0
Case 3	91.8	48.89	45.3	415.0	44.5
Case 4	112.2	58.56	62.6	467.0	56.5

Distance to runway based trajectory command in the form of height and vertical velocity profiles for all schemes, is presented in figure 5.5 - 5.6 for case 1. Origin corresponds to intended touch down point on runway and the direction of travel is towards intended touch down point.

It can be observed from comparison of distance output for the above mentioned cases that the proposed scheme is giving reduced landing distance during flare phase. Moreover, this scheme ensures touch down at intended touch down point with intended touch down vertical velocity thus providing lower impact at touchdown.

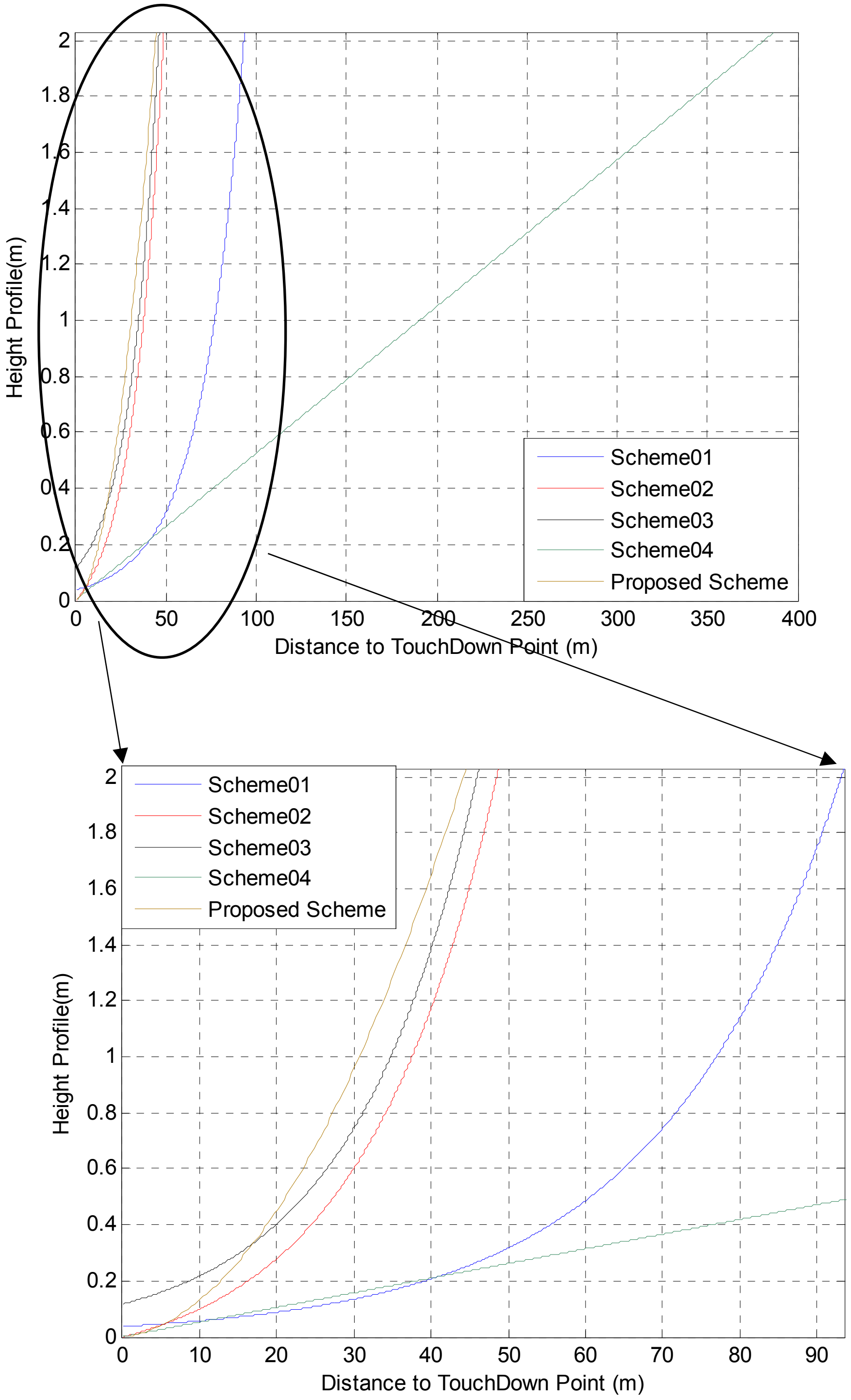

Figure 5.5: Height profile vs distance required comparison

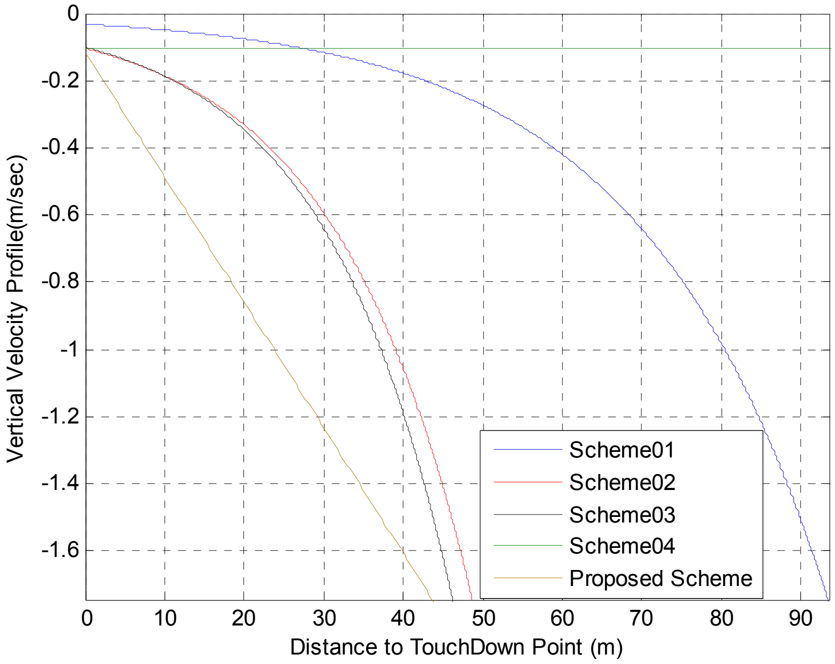

Figure 5.6: Vertical velocity profile vs distance required comparison

Chapter 6: Control System Design

Control system enables the UAV to move along a desired trajectory, while rejecting disturbances and catering for uncertainties. For UAV control framework, cascaded control scheme is generally used with inner loop (airframe stabilization) and outer loop (trajectory tracking) [**11**]. The controller design is based on the H_∞ loop shaping technique to cater for uncertainties i.e. unmodelled dynamics and parametric uncertainties due to variation of aerodynamic, thrust and inertial data. The designed controller provides desired performance and stability in the wake of model uncertainties or parametric uncertainties. The implementation of designed controller is done in c-language based s-function in discretized state space form.

The organization of this chapter is as following: Section 6.1 describes the onboard avionics. Section 6.2 presents the H_∞ Loop-Shaping technique theory. Section 6.3 presents controller design for glide phase and flare phase.

6.1 Onboard Sensors

The following onboard sensors are assumed to be available onboard while designing of control system:

- Inertial Measurement Unit (IMU) with accelerometers and rate gyros for body accelerations in 3 axis and angular rates, attitude angles in 3 axis.
- One Global Positioning Sensor GPS/Differential GPS providing position and ground speed
- One Airdata System (ADS) providing pressure altitude and airspeed measurements

6.2 H_∞ Loop Shaping Technique

6.2.1 Loop Shaping Fundamental Relations

Consider G(s) representing the open loop transfer function. It is product of all transfer functions in the loop i.e. actuator, plant, sensor and controller. The sensitivity function S(s) and complementary sensitivity function T(s) are [**35**]

$$L(s) = G(s)K(s) \tag{6. 1}$$

$$S = (I + L)^{-1} \tag{6. 2}$$

$$T = (I + L)^{-1} L) \tag{6. 3}$$

$$T(s) + S(s) = I \tag{6. 4}$$

A requirement for command tracking is to have complementary sensitivity function close to unity in the desired frequency band and for noise rejection it must be close to zero. Sensitivity function should be close to zero for disturbance rejection in the desired frequency domain.

Loop shaping involves loop transfer function magnitude response shaping i.e. L(s) =G(s)*K(s) and in turn how the controller K(s) be selected for loop gain shaping to get the desired performance and robust stabilization. The loop gain L(s) in bandwidth region is required to be as much high as possible. The trade-offs between design objectives in feedback control are

- Requirement of large loop gain for good disturbance rejection, command tracking and stabilization of unstable plant
- Small loop gain for noise rejection on plant outputs

Robust stabilization does not give the leverage of specifying performance requirements. Thus, plant G(s) is multiplied with pre and post compensators for openloop singular values shaping, prior to stabilization of the shaped plant.

W1 and W2 being the pre and post compensators for the shaped plant Gs (s).

$$L(s) = W1(s)G(s)W2(s) \tag{6. 5}$$

Feedback controller K(s) for the plant G(s) becomes

$$K(s) = W1(s)K_s(s)W2(s) \tag{6. 6}$$

6.2.2 Weights Selection for Loop Shaping

Weights selection is one of the critical step in the loop shaping design. Weights are intended to provide high gain at low frequencies for better disturbance rejection capabilities. They ensure intended bandwidth for the compensated system with roll off at high frequency for noise attenuation.

6.2.3 H∞ Loop shaping

H∞ Loop shaping is modern control theory design methodology, centered on inputs and outputs weighting in frequency domain of nominal plant and possesses several advantages regarding the classical methods [**32**]

- Straightforward method with no γ iterations requirement

- merges performance advantages of the classical loop-shaping with H∞ optimization robust characteristics [**33**]

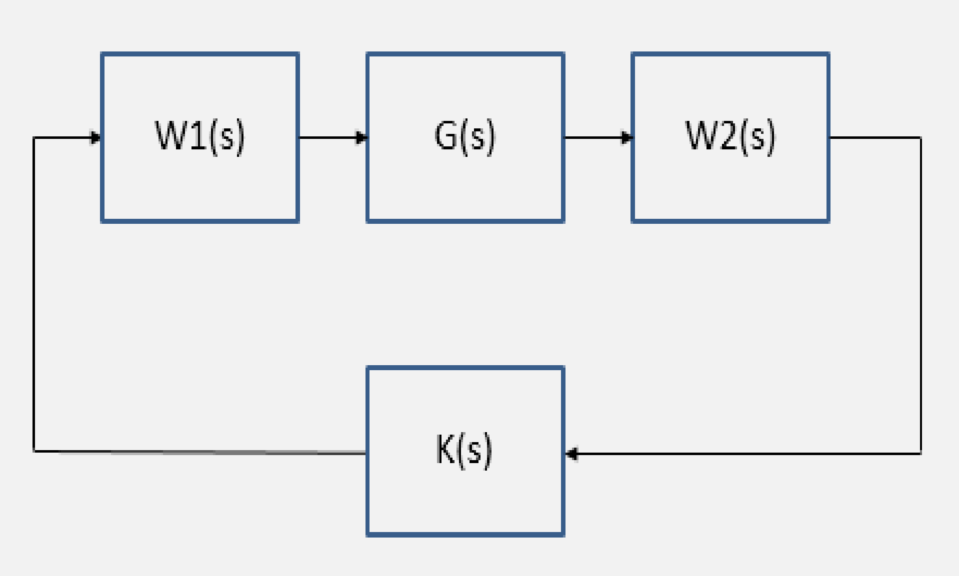

Figure 6.1: Shaped Plant and Controller [35]

It involves the controller to shape the loop gain for the nominal plant in different frequency regions to cater for perturbations while warranting closed-loop stability and (if possible) performance with in a known bound of perturbation [**34**].

The design process is two stage

- augmentation of pre-compensator with plant model for desired shape of open-loop frequency response singular values
- H∞ optimization of this shaped plant for robustly stabilization w.r.t. co-prime factor uncertainty.

Generalized closed loop structure is show in figure 6.2.

The exogenous input w (includes reference signal and disturbances) and the operating variables u are the two inputs. The outputs are the performance signals z which needs to be minimized and y are the measured quantities that require control. y is related to input u through K as

$$\begin{bmatrix} z \\ y \end{bmatrix} = P(s)\begin{bmatrix} w \\ u \end{bmatrix} = \begin{bmatrix} P_{11}(s) & P_{12}(s) \\ P_{21}(s) & P_{22}(s) \end{bmatrix}\begin{bmatrix} w \\ u \end{bmatrix} \tag{6. 7}$$

$$u = K(s)y \tag{6. 8}$$

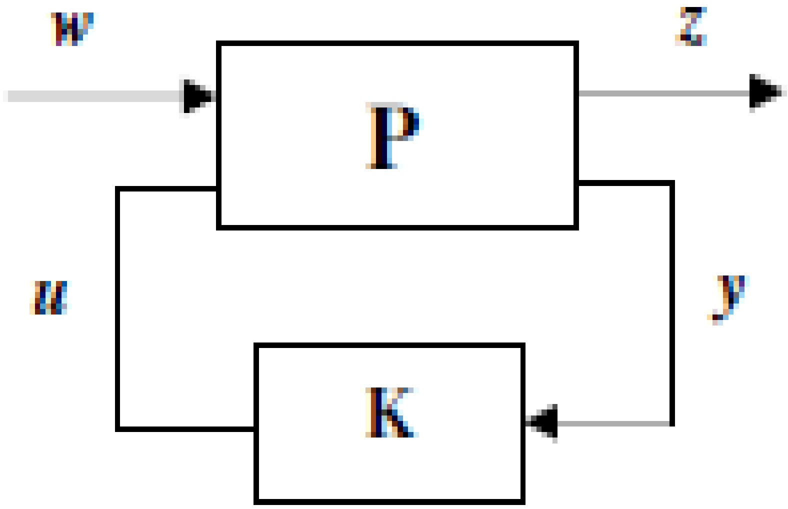

Figure 6.2: H∞ close loop structure [34]

z is related to w as

$$z = F_l(P,K)w \tag{6. 9}$$

Having defined:

$$F_l(P,K) = P_{11} + P_{12}K(I - P_{22}K)^{-1}P_{21} \tag{6. 10}$$

Therefore, the H∞ controller design goal is to get a controller K which reduces FL according to H∞ norm

$$\| F_l(P,K) \|_\infty = \sup_\omega \overline{\sigma}(F_l(P,K)(j\omega)) \tag{6. 11}$$

where $\overline{\sigma}$ = max F singular value L.

The plant G which has a normalized left co-prime factorization and its stabilization is

$$G_\Delta = M^{-1}N \tag{6. 12}$$

The perturbed plant model G_Δ is shown in figure 6.3

where $\overline{M}$, $\overline{N}$ = left co-prime factorization of G with

$$\| \Delta = [\Delta_M \Delta_N] \|_\infty \leq \varepsilon \tag{6. 13}$$

The maximum value of ε obtained non-iteratively is

$$\gamma_{\min} = \varepsilon_{\max}^{-1} = \{I - \| [NM] \|_H^2 \}^{-\frac{1}{2}} \tag{6. 14}$$

where $\| \, . \, \|_H$ = Hankel norm

$\varepsilon_{\max}$ = max stability margin

A controller that guarantees

$$\| F_l(P,K) \|_\infty = \| \begin{bmatrix} K \\ I \end{bmatrix} (I - PK)^{-1} M^{-1} \|_\infty \le \frac{1}{\varepsilon} \tag{6. 15}$$

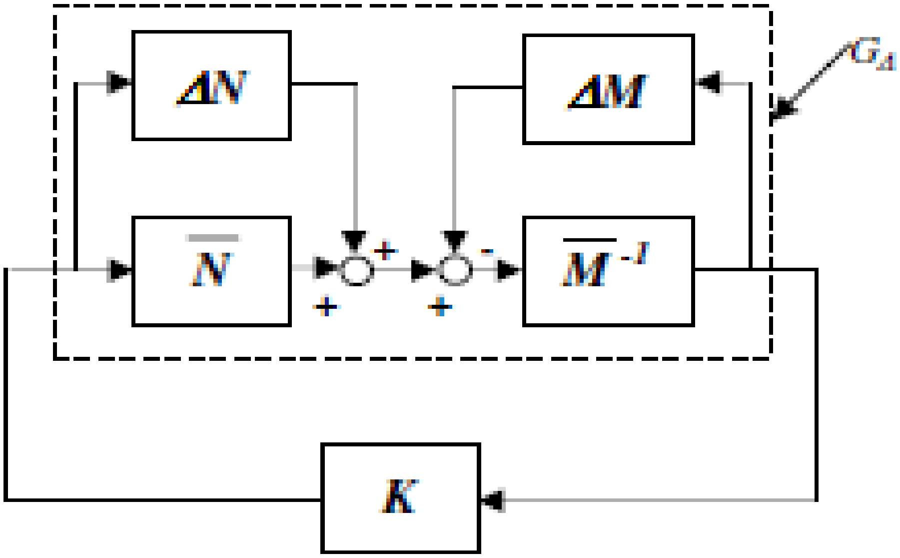

Figure 6.3: Co-prime Factorization [34]

for a specified $\gamma > \gamma_{\min}$ is

$$K = \begin{bmatrix} A + BF + \gamma^2 (L^T)^{-1} Z C^T (C + DF) & \gamma^2 (L^T)^{-1} Z C^T \\ B^T X & -D^T \end{bmatrix} \tag{6. 16}$$

$$F = S^{-1}(D^T C + B^T X) \tag{6. 17}$$

$$L = (1 - \gamma^2) I + XZ \tag{6. 18}$$

The synthesis procedure yields the controller of figure 6.1.

6.3 Controller Design

6.3.1 Control Scheme

The longitudinal plane control schemes in [**11**, **33**] are altitude command tracking or vertical velocity command tracking with cascaded pitch angle hold. These are shown in figure 6.4. Pitch angle hold loop act as an inner loop. It is formed by tracking of pitch angle ‘θ’ command while the rate feedback gain provides added damping to short period mode. The outer loop is formed by tracking of height or vertical velocity. Altitude tracking control is used in glide Phase while velocity tracking control is used in flare phase.

6.3.2 Glide Phase

6.3.2.1 The Plant Model

Linear control system design starts with linear model of vehicle. UAV longitudinal dynamic model as discussed in the chapter 3 is used for controller design. Longitudinal plane linear models were extracted for V = {18, 20, 22} (m/s) with UAV takeoff weight = {7.4, 9.0} (Kg) and height = {5, 10, 20, 30} (m). The linear model selected for control design was taken at V = 20m/sec and at a height of 20 m as shown in figure 6.5. The red dot shows the design time linear model.

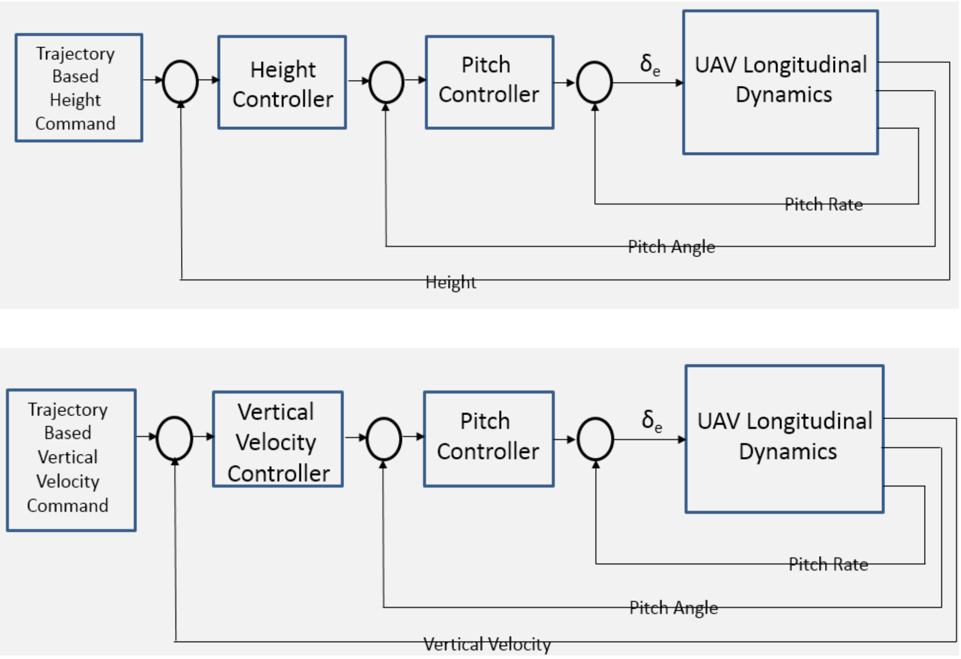

Figure 6.4: Control Schemes [11]

6.3.2.2 The Specifications

Since glide phase is a critical flight phase, maximum tracking of generated command is required for accurate landing. The overshoot < 12% was imposed with a minimum rise time. Height controller in the outer loop is required to track reference height by giving the control signal to inner loop. Further closed loop system response to step input exhibits overshoot < 10%. The steady state error required to be <5%. Controller in the outer loop is design in such a way that it tracks the reference height by applying appropriate deflections of the elevator if the actual height differs from the desired reference value.

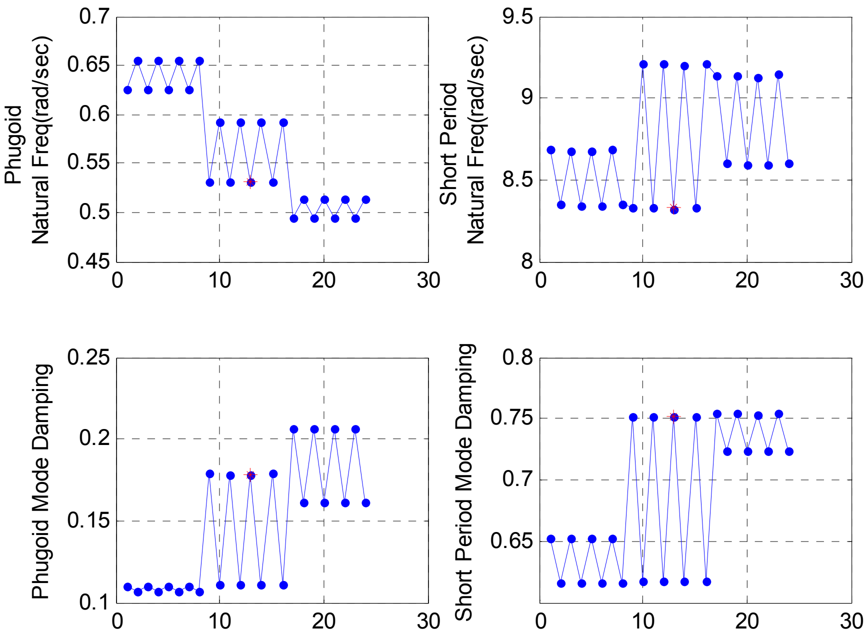

Figure 6.5: Plant selection for Glide phase Controller

6.3.2.3 Pitch Rate Loop Design

The damping ratio in short period mode for selected model is 0.75. Rate feedback introduced to further improve short period damping. Feedback gain was selected from root locus plot of δ_e to pitch rate q. Figure 6.6 indicates that a gain of 0.0193 improves damping to 0.8 and is used as a feedback gain in pitch rate loop. The increase damping of short period mode is presented in bode plot of δ_e to pitch angle Θ in figure 6.7.

6.3.2.4 Pitch Loop Design

The plant model consists of actuator transfer function in series with UAV linear model along with pitch rate ‘q’ feedback with gain. Actuator model is taken to be unity gain as its bandwidth is 8Hz and doesn’t affect the control bandwidth. A delay of 40msec is used as *Pade*’ approximation of second order at

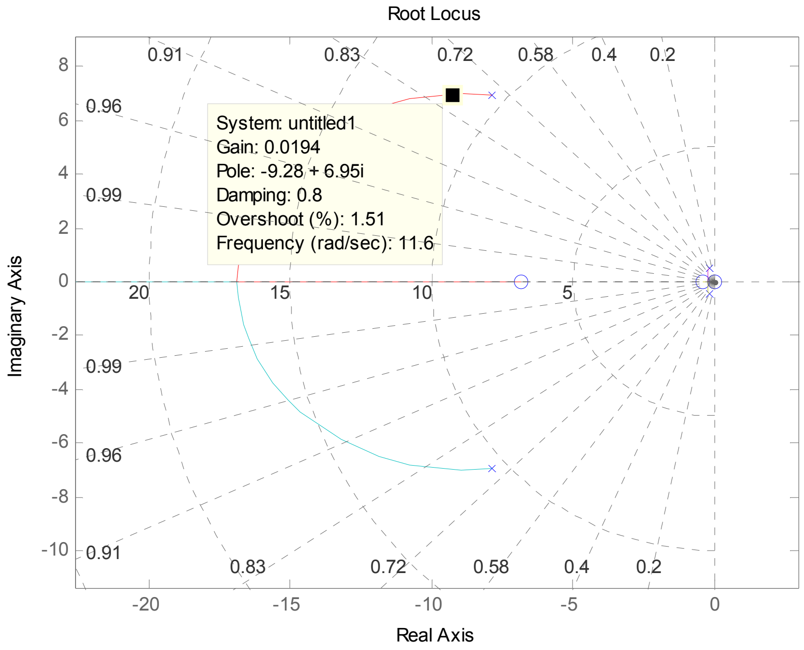

Figure 6.6: Root locus for Glide phase pitch rate Loop

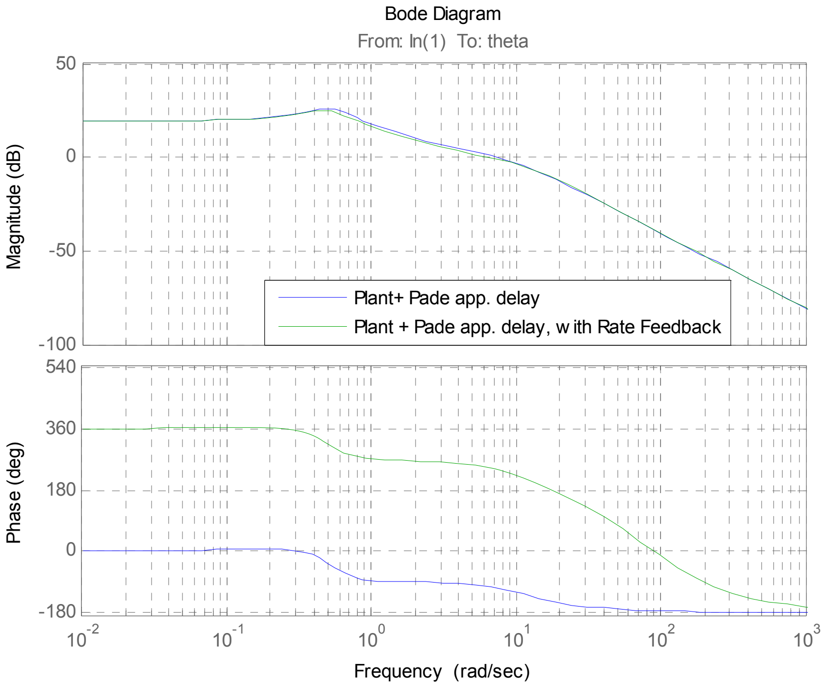

Figure 6.7: Bode plot for Glide phase pitch rate Loop

design time as specified in simulation to account for sensor delays. The control loop is SISO with input elevator and output theta. Weights selected for shaping of open loop frequency response are shown in figure 6.8

$$W1 = \frac{(s+0.7)}{(s+0.04)} \qquad W2 = \frac{338.878(s+8.372)}{(s+130)(s+21.77)}$$

Using H∞ loop shaping algorithm from [**35**], algebraic riccati equations are solved. The resulting controller for pitch loop control has gamma = 2.3253 with gain margin: 2.77@ 28.80 rad/sec and phase margin: 76.4^{o} @ 6.44 rad/sec. The designed controller gain and phase margins depicts enough capabilities to cater for uncertainties in the form of gain and delay margins.

Bode plot for pitch control open loop transfer function with H∞ controller is given in figure 6.9. The nyquist plot for open loop transfer function is given in figure 6.10. Bode plot for close loop pitch control transfer function and sensitivity transfer function is given in figure 6.11. Close loop step response for pitch control loop with H∞ controller are given in figure 6.12. Figure 6.13 contains the close loop pitch angle step responses with the designed controller over the whole envelope. Figure 6.14 shows the open loop gain/ phase margins for pitch control with designed controller over the whole envelope and bode plot over the whole envelope for close loop pitch control with designed controller. These plots ensure that the designed controller is both stable and controllable over the envelope.

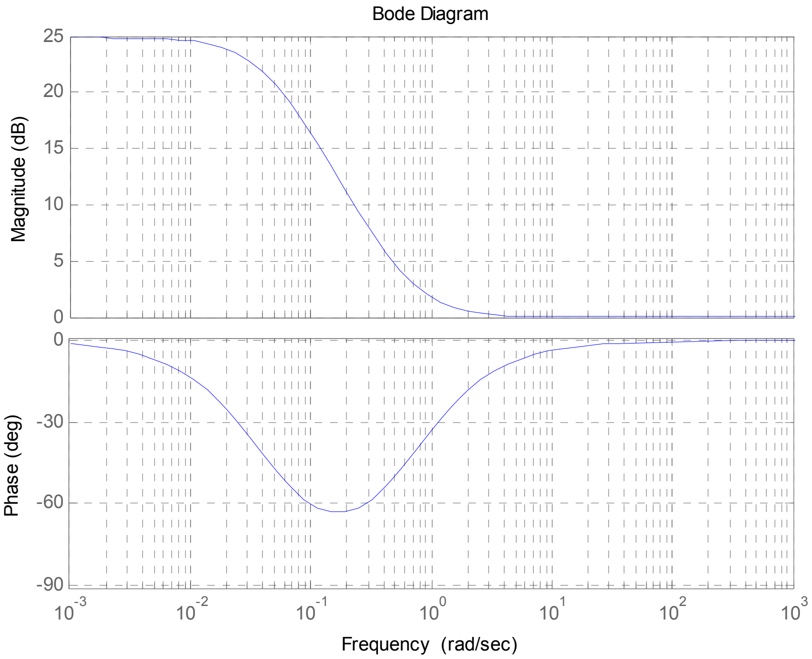

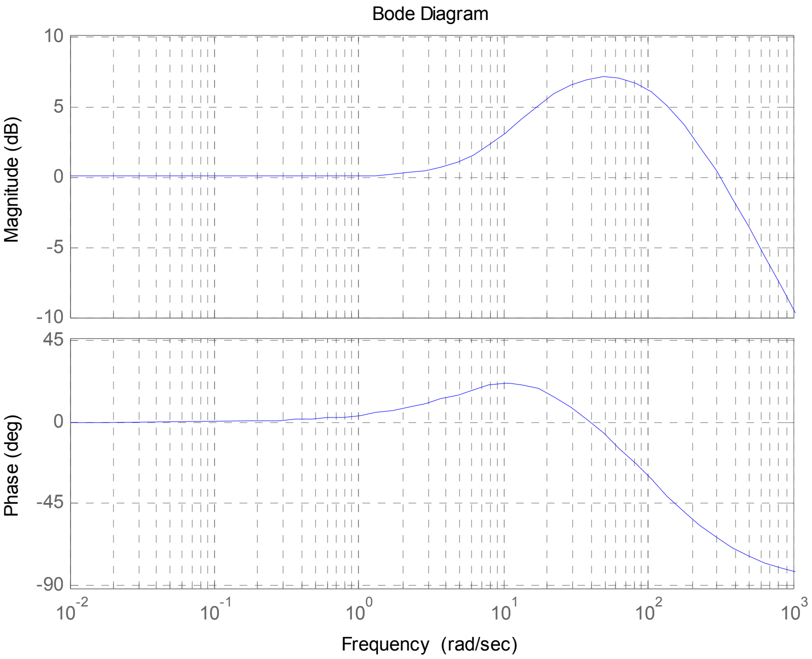

Figure 6.8: Bode Plots of Glide phase pitch control Loop shaping weights W1 and W2

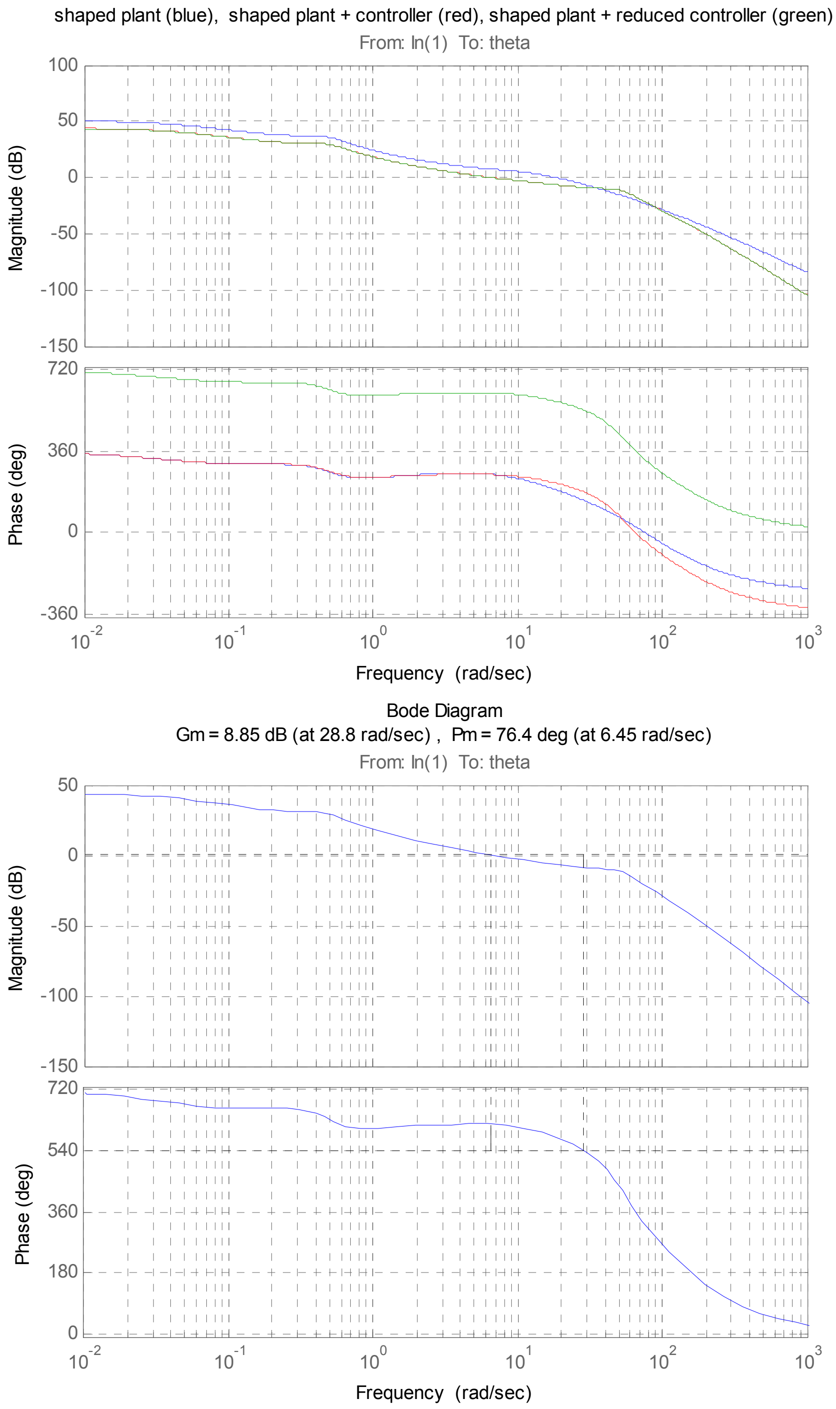

Figure 6.9: Bode plot for Glide phase open loop shaped plant and H∞-controller+plant

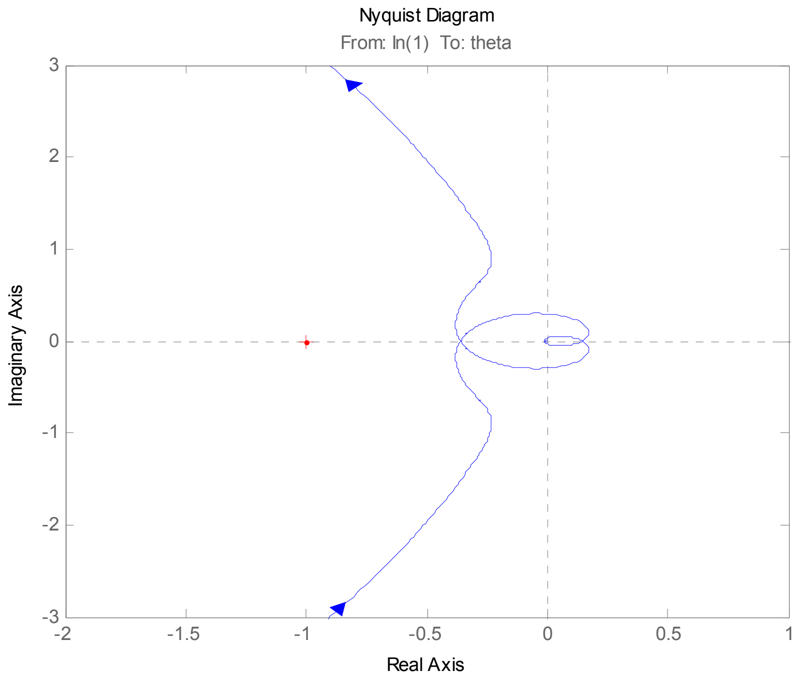

Figure 6.10: Nyquist plot for Glide phase open loop pitch control transfer function with H∞ controller

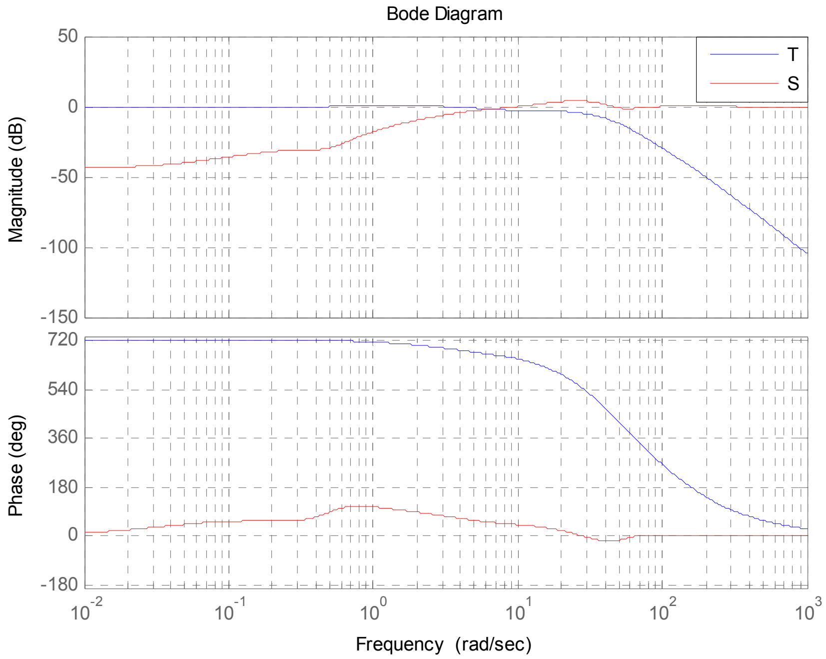

Figure 6.11: Bode plot for Glide phase close loop pitch control and sensitivity transfer function with H∞ controller

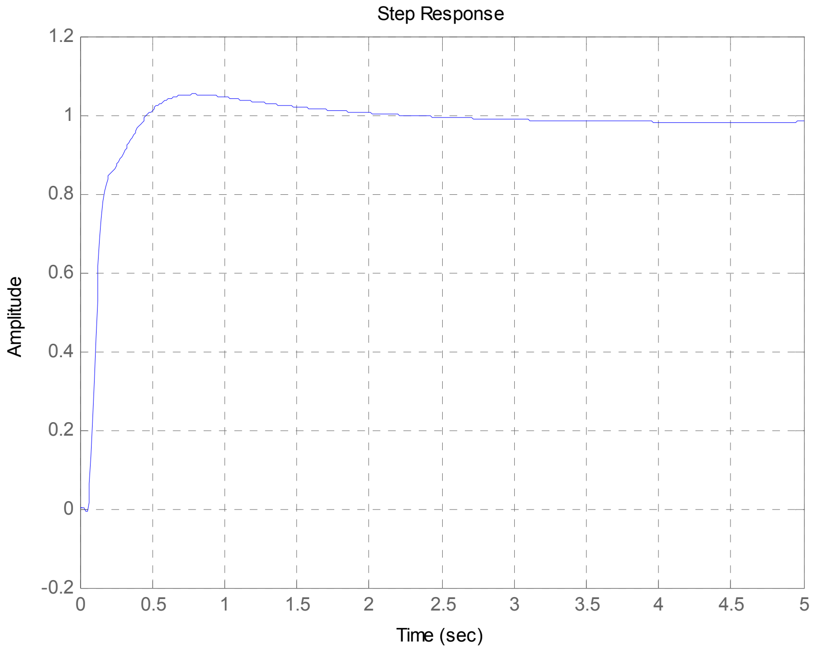

Figure 6.12: Step response for Glide phase pitch control close loop with H∞ controller

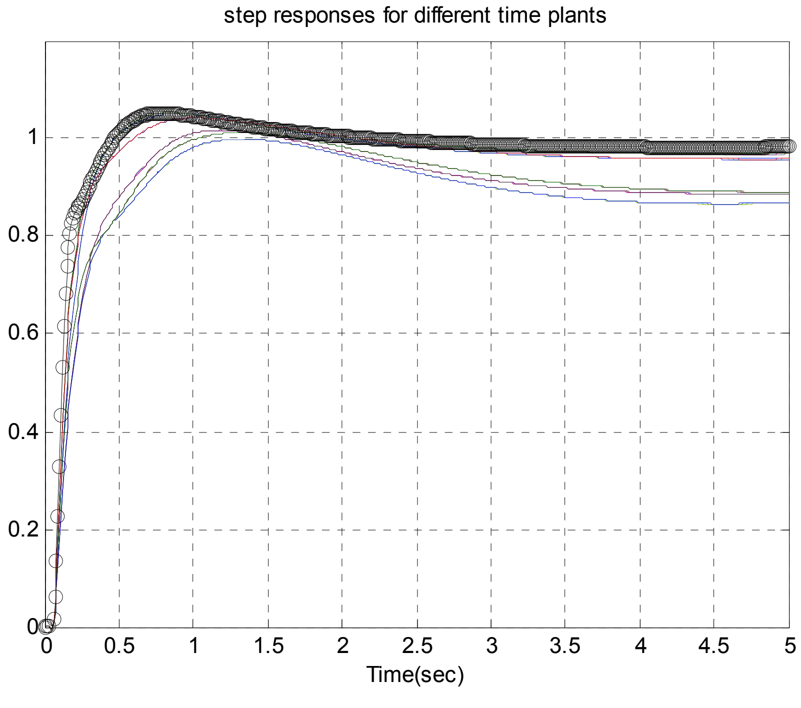

Figure 6.13: Glide phase step response for pitch control close loop over the whole envelope

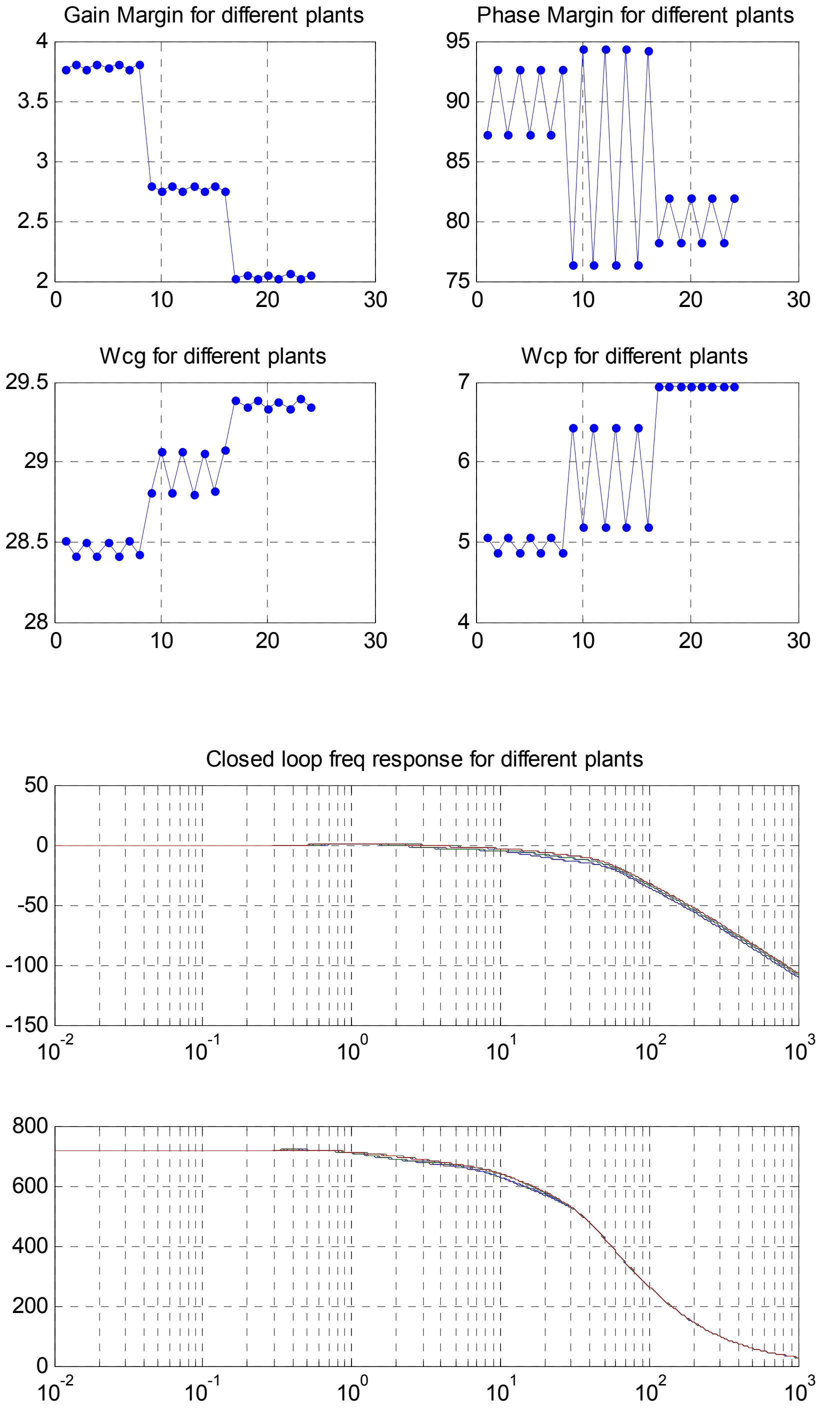

Figure 6.14: Glide phase pitch control Gain/Phase margin and close loop bode plot over the whole envelope

6.3.2.5 Height Controller

Bode plot for height transfer function with cascaded pitch loop is shown in Figure 6.15. Normally, bandwidth of outer loop is kept 0.1 times the bandwidth of inner loop.

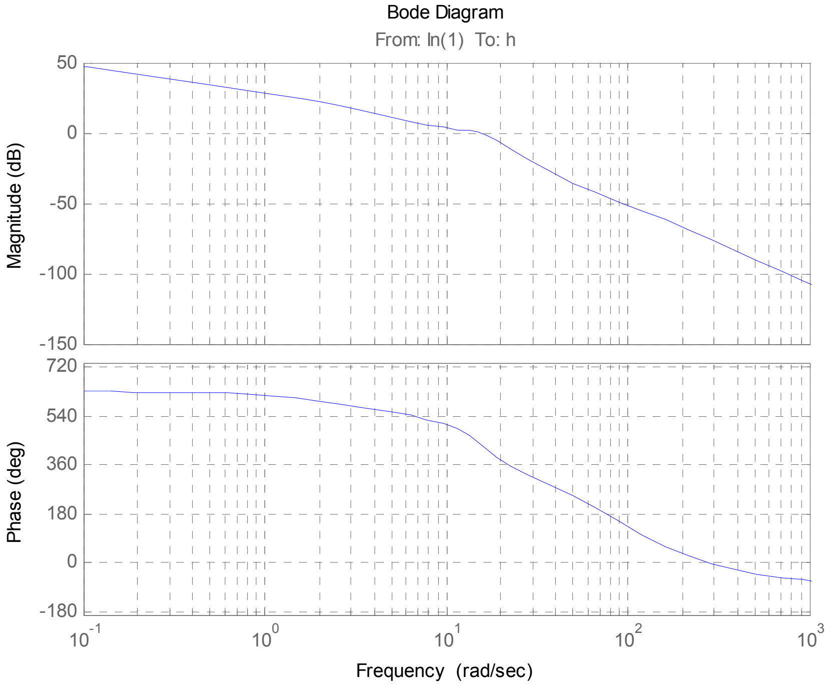

Figure 6.15: Bode plot of Height transfer function with cascaded pitch loop

The weights selected for loop shaping of height transfer function are given below and bode plot is presented in figure 6.16

$$W1 = \frac{0.0225(s+0.1)}{(s+0.01)} \qquad W2 = \frac{79.3916(s+1.789)}{(s+2.236)(s+50)}$$

The shaped plant frequency response is shown in figure 6.15. Using H∞ loop shaping algorithm from [**35**], algebraic riccati equations are solved and the resulting controller for height loop control has gamma = 1.7736 with gain margin 7.53@ 3.90 rad/sec and phase margin is 71.60° @ 0.59 rad/sec.

Bode plot for open loop height control transfer function is given in figure 6.17 and nyquist plot is given in figure 6.18. Bode plot of close loop height control transfer function and sensitivity transfer function with H∞ controller is given in figure 6.19. Step response of close loop height control transfer function is given in figure 6.19. Figure 6.20 contains the close loop height step responses with the designed controller over the whole envelope. Figure 6.21 shows the open loop gain/phase margins for height control with designed controller over the whole envelope and bode plot over the whole envelope for close loop height controller.

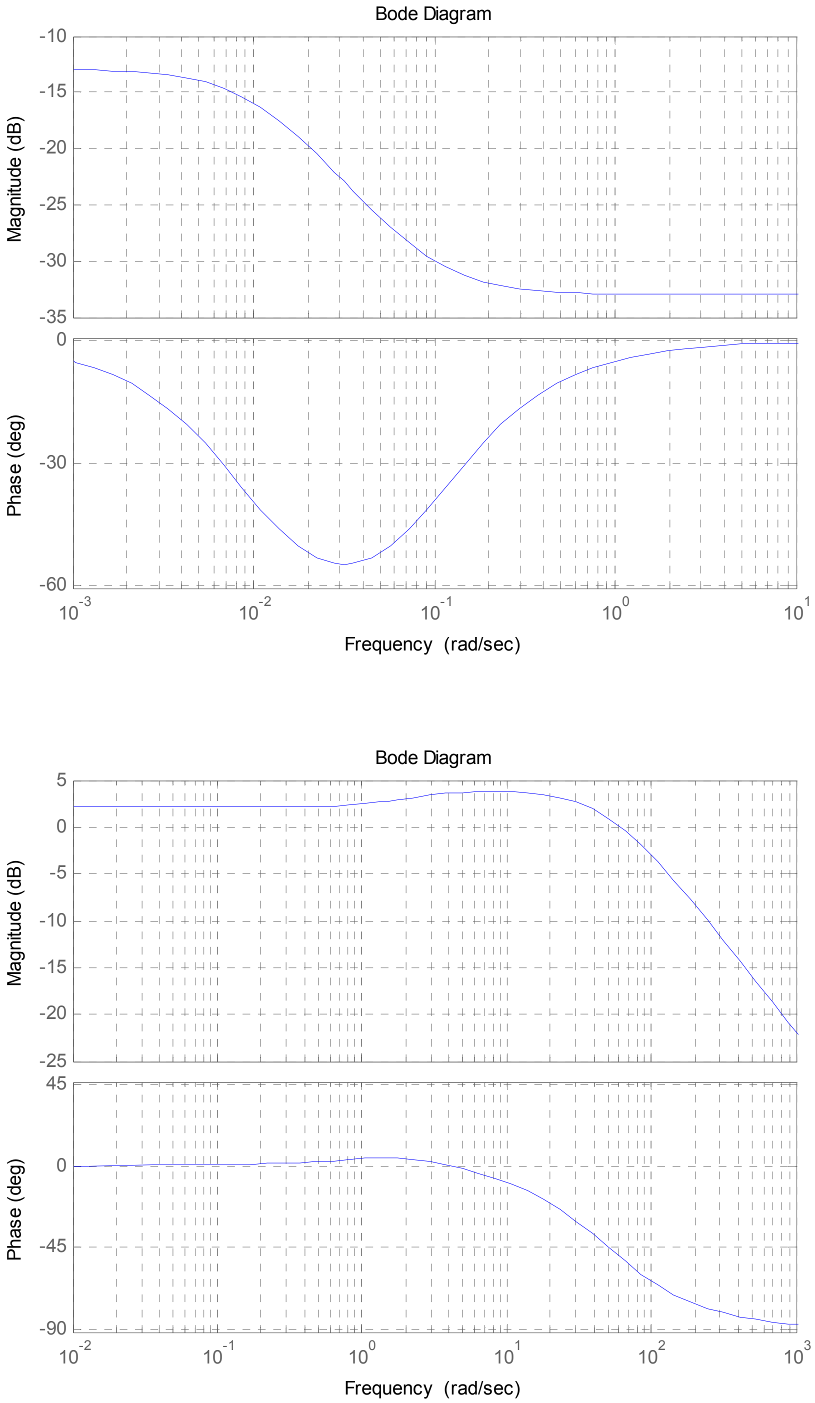

Figure 6.16: Bode plots of weights W1 and W2 for shaping Height loop

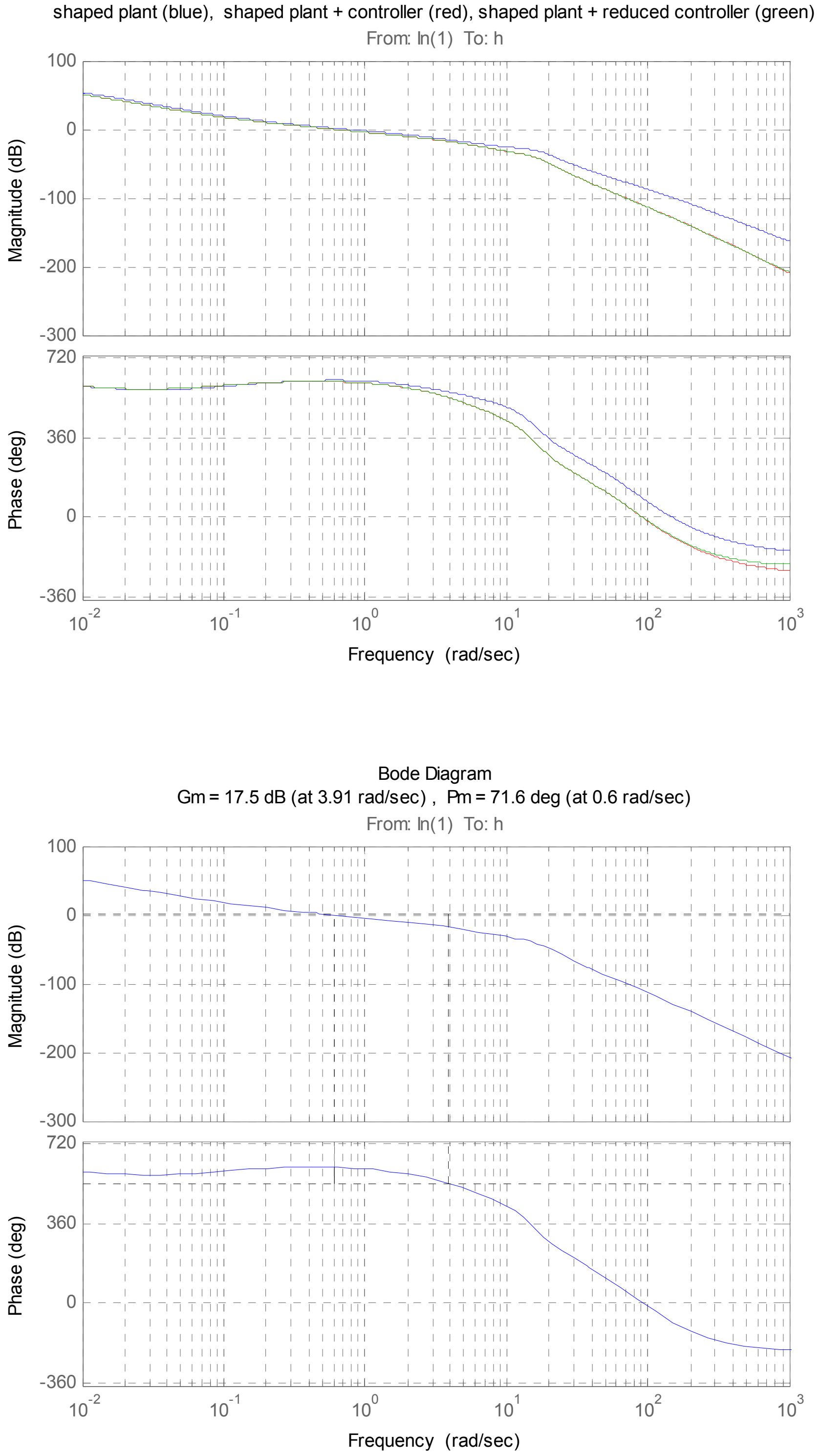

Figure 6.17: Bode plot for height loop shaped Plant and H∞ controller+plant

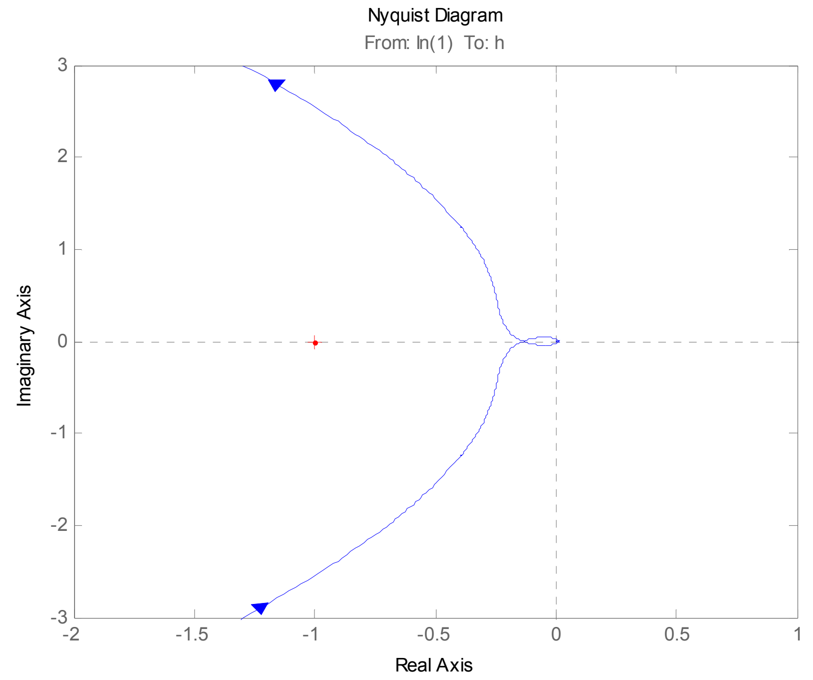

Figure 6.18: Bode plots and nyquist plot for Height Control open loop transfer function with H∞ controller

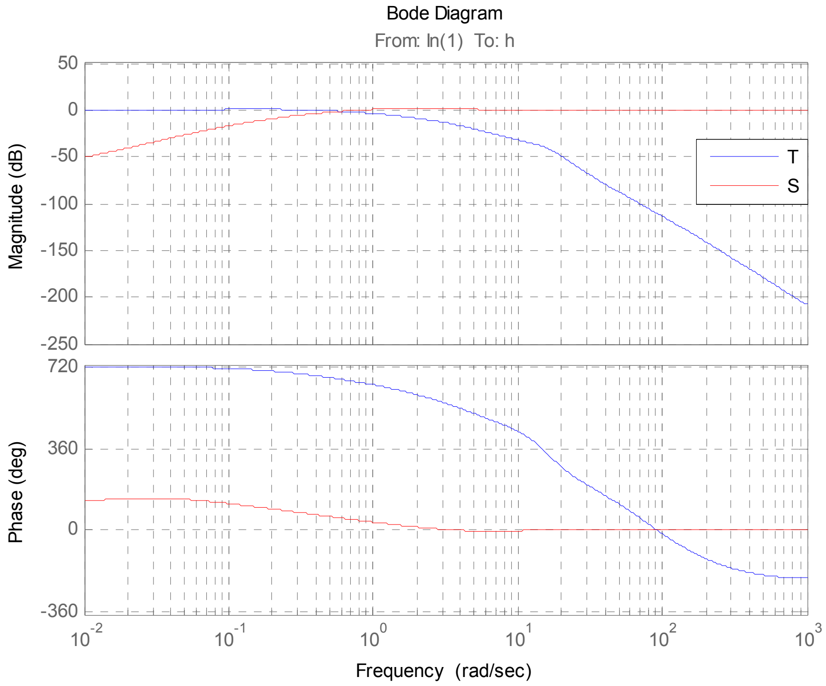

Figure 6.19: Bode plot for Height Control close loop and sensitivity transfer function with H∞ controller

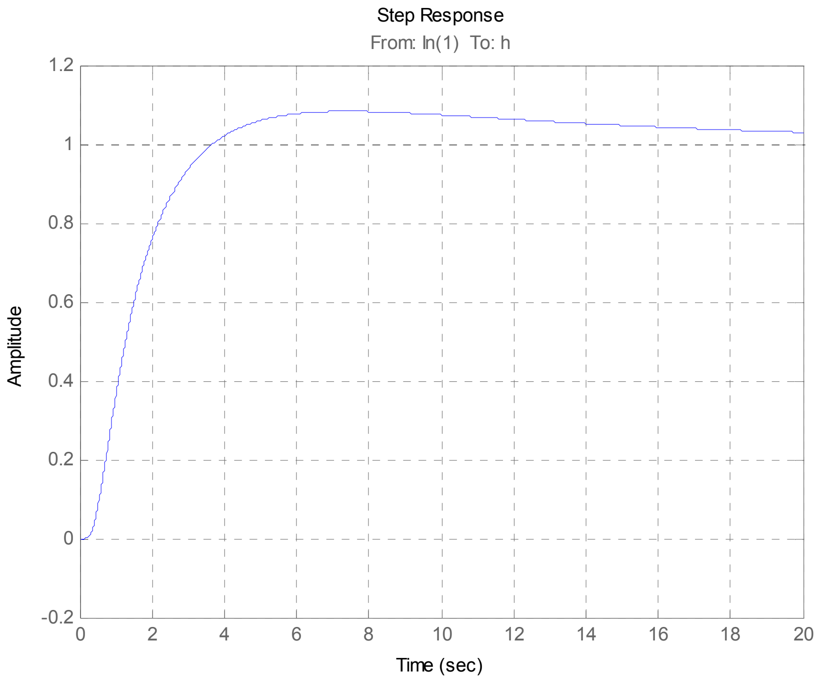

Figure 6.20: Step response for Height Control close loop with H∞ controller

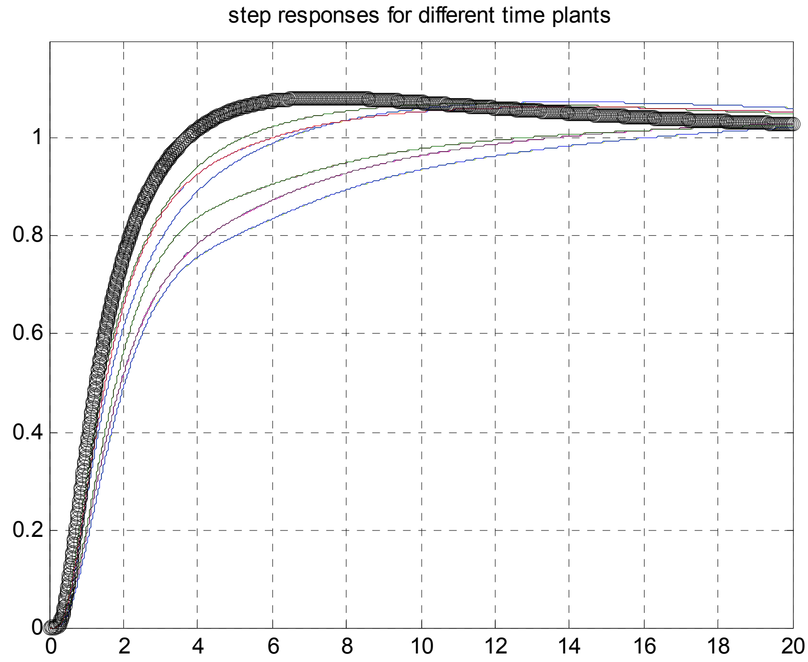

Figure 6.21: Glide Phase close loop height control step response over the envelope

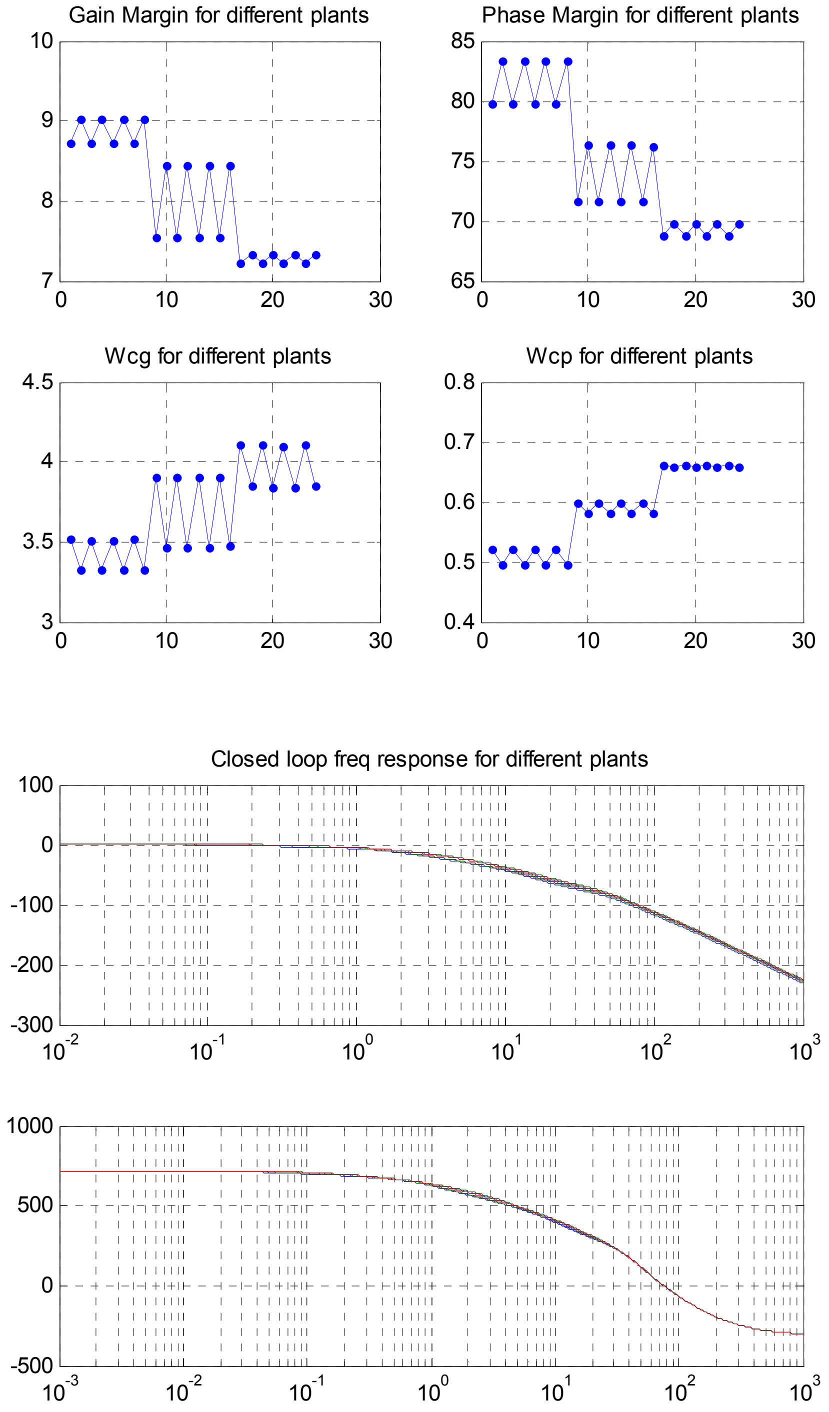

Figure 6.22: Glide Phase open loop height control stability margins and close loop bodeplot over the envelope

6.3.3 Flare Phase

6.3.3.1 The Plant Model

Longitudinal plane linear models are extracted for V = {18, 20, 22} (m/s) with UAV takeoff weight = {7.4, 9.0} (Kg) at height of 5m. Linear model for controller design is taken at V = 20m/sec and at a height of 5 m with empty payload weight. Red dot in figure 6.23 shows the design point linear model.

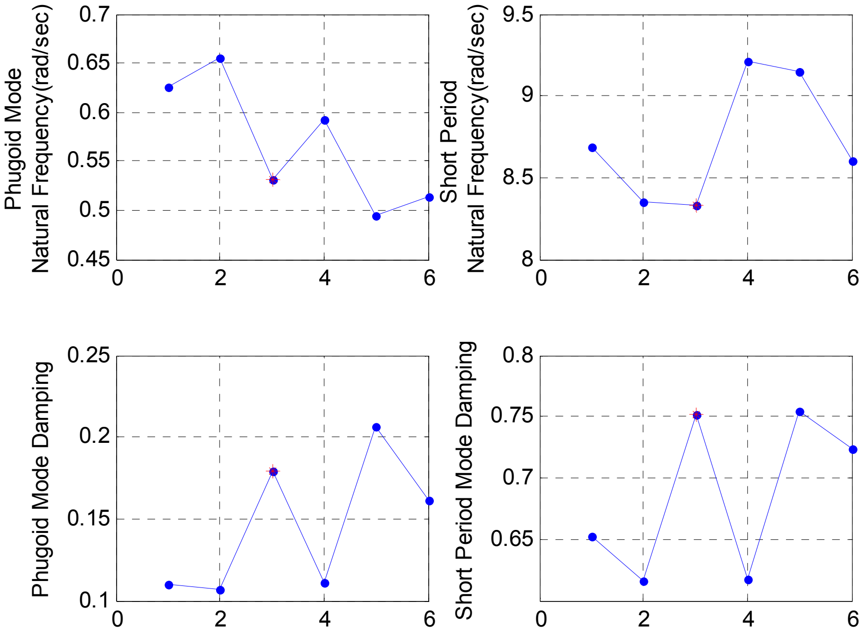

Figure 6.23: Plant selection for Flare phase Controller

6.3.3.2 The Specifications

Since flare phase is the most critical flight phase, maximum tracking of generated command is required for accurate landing. The overshoot < 15% was imposed with a minimum rise time. Vertical velocity controller in the outer loop is required to track reference vertical velocity profile by giving the control signal to inner loop. Further closed loop system response to step input exhibits overshoot < 10%. The steady state error required to be <5%. Controller in the outer loop is design in such a way that it tracks the reference vertical velocity profile by applying appropriate deflections of the elevator if the actual height differs from the desired reference value.

6.3.3.3 Pitch Rate Loop Design

The damping ratio in short period mode for selected model is 0.752. Rate feedback introduced to further improve short period damping. Feedback gain was selected from root locus plot of δ_e to pitch

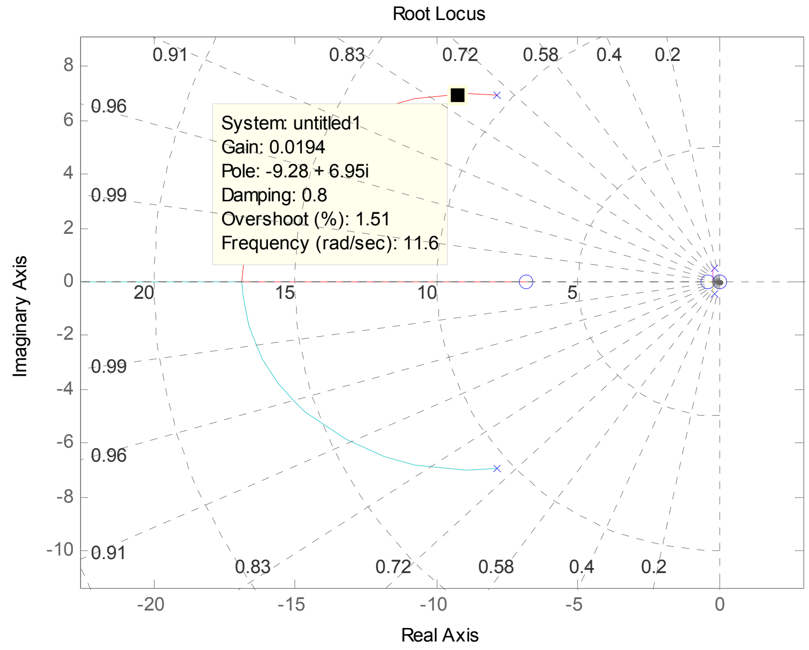

Figure 6.24: Root locus for flare phase pitch rate loop

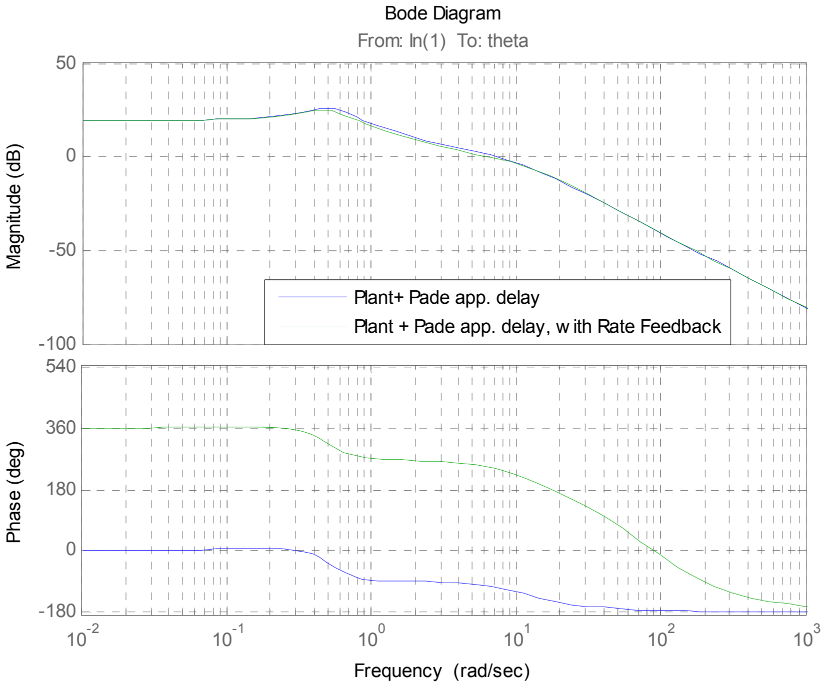

Figure 6.25: Bode plot for flare phase pitch rate loop

rate q. Figure 6.24 indicates that a gain of 0.0193 improves damping to 0.8 and is used as a feedback gain in pitch rate loop and bode plot of δ_e to pitch angle ϴ showing increased damping of short period mode. Figure 6.25 shows the bode plot with reduced peak in magnitude plot for short period mode in response to rate feedback.

6.3.3.4 Pitch Loop Design

The plant model consists of longitudinal plane linear model with pitch rate 'q' feedback with gain. Actuator model is taken to be unity gain as its bandwidth is 8Hz and does not affect the control bandwidth. A delay of 40msec is used as ***Pade'*** approximation of second order at design time as specified in simulation to account for sensor delays.

Weights selected for shaping of open loop frequency response are shown in figure 6.26

$$W1 = \frac{(s+0.7)}{(s+0.01)} \qquad W2 = \frac{647.8592(s+5.606)}{(s+100)(s+32.51)}$$

Using H_∞ loop shaping algorithm from [**35**], algebraic riccati equations are solved and the resulting controller for pitch loop control has gamma = 2.3765 with gain margin 2.21@ 31.56 rad/sec and phase margin is 76.74^o @ 9.42 rad/sec.

Bode plot for pitch control open loop transfer function with H_∞ controller is given in figure 6.27, nyquist plot for pitch control open loop transfer function with H_∞ controller is given in figure 6.28. Bode plot for frequency response of pitch control close loop transfer function and sensitivity transfer function is given in figure 6.29. Close loop step response for pitch control loop with H_∞ controller is given in figure 6.30.

Figure 6.31 shows the step response for pitch control loop with H_∞ controller over the whole flare envelope while figure 6.32 shows the stability margins and close loop bode plot over the whole envelope.

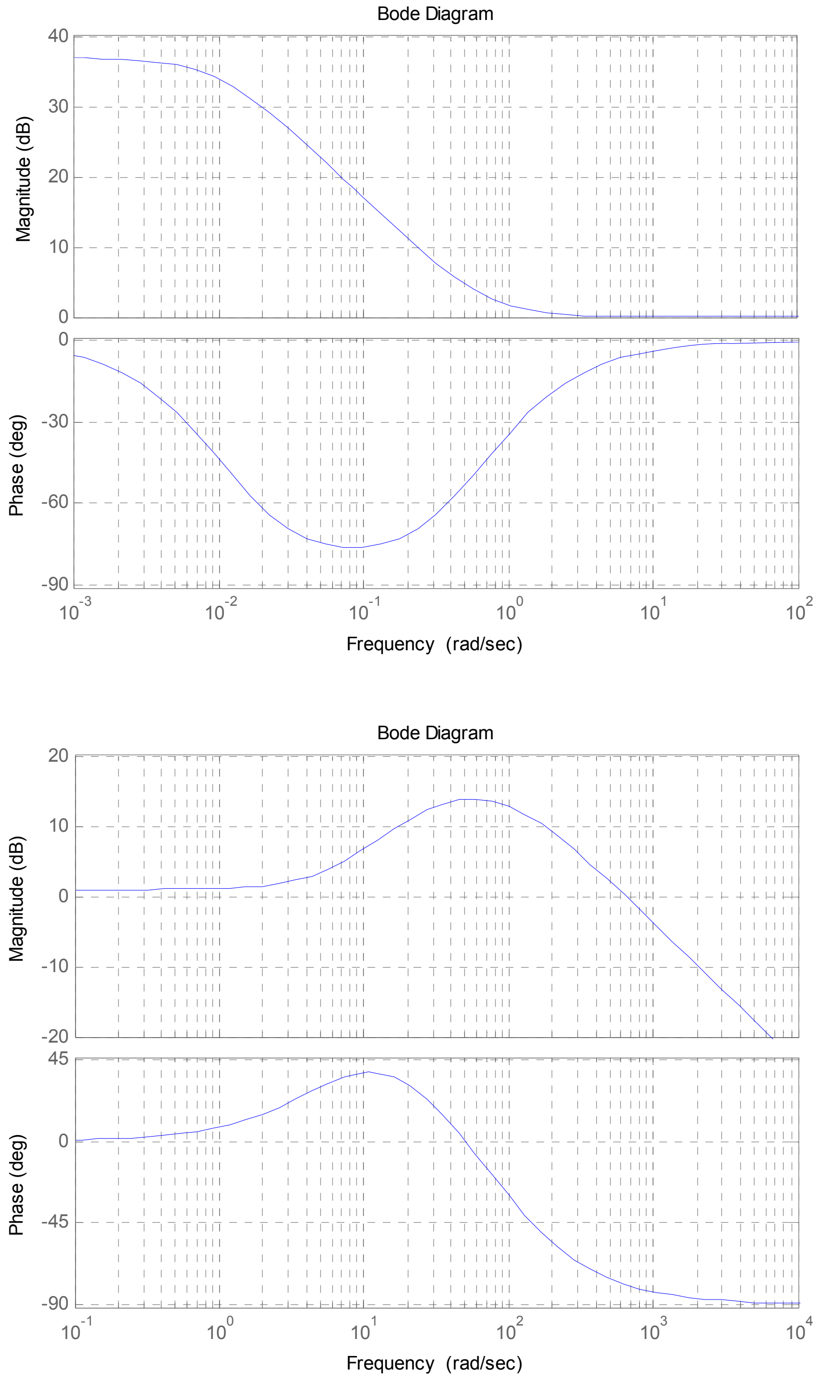

Figure 6.26: Bode Plots of Flare Phase Pitch Control Loop shaping weights W1 and W2

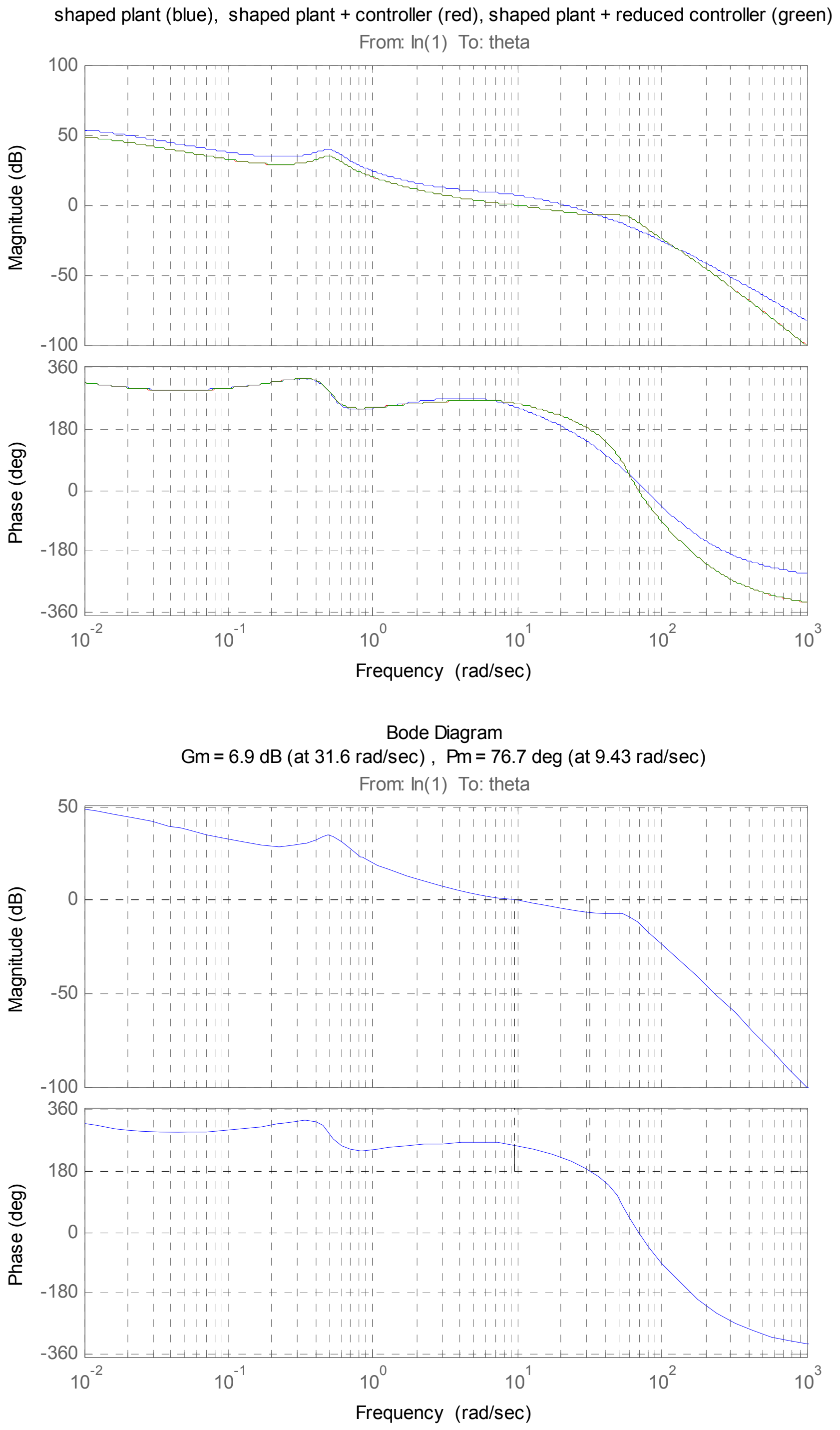

Figure 6.27: Bode plot for flare phase pitch control open loop transfer function with H∞ controller

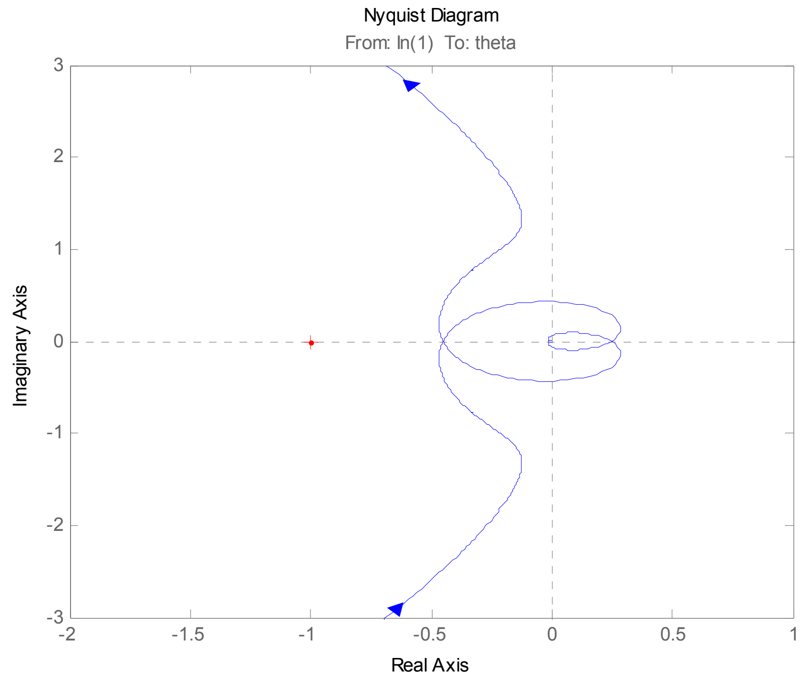

Figure 6.28: Nyquist plot for flare phase pitch control open loop transfer function with H∞ controller

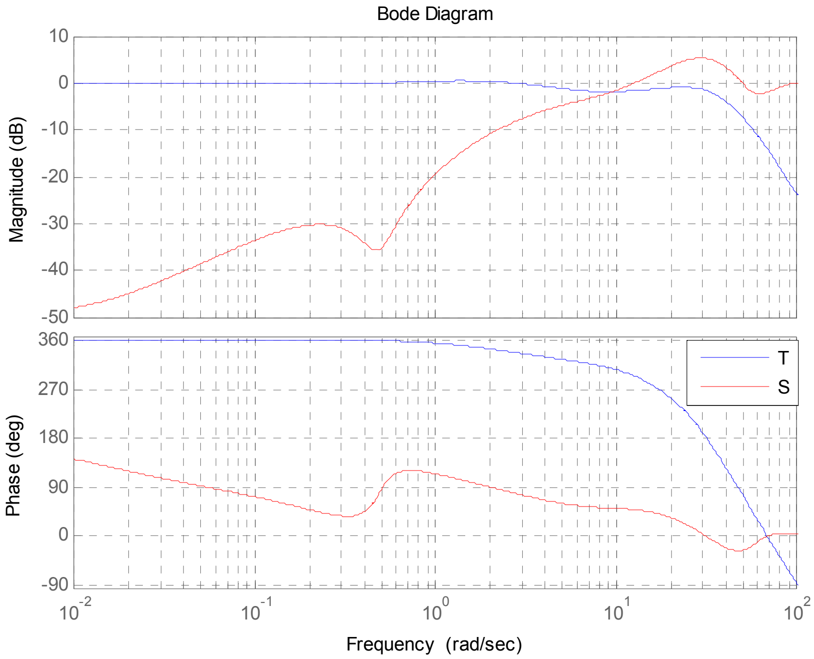

Figure 6.29: Bode plot for flare phase pitch control close loop and sensitivity transfer function with H∞ controller

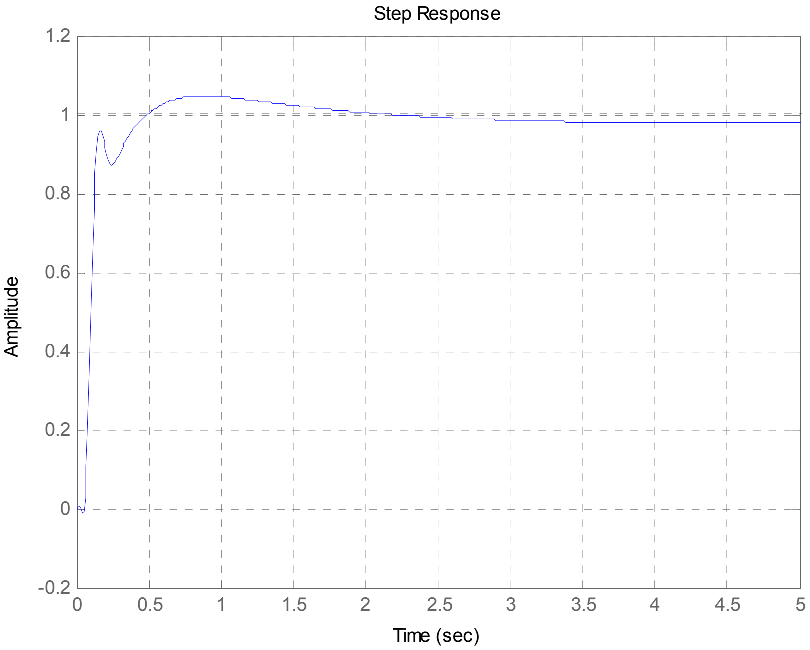

Figure 6.30: Step response for flare phase pitch control close loop with H∞ controller

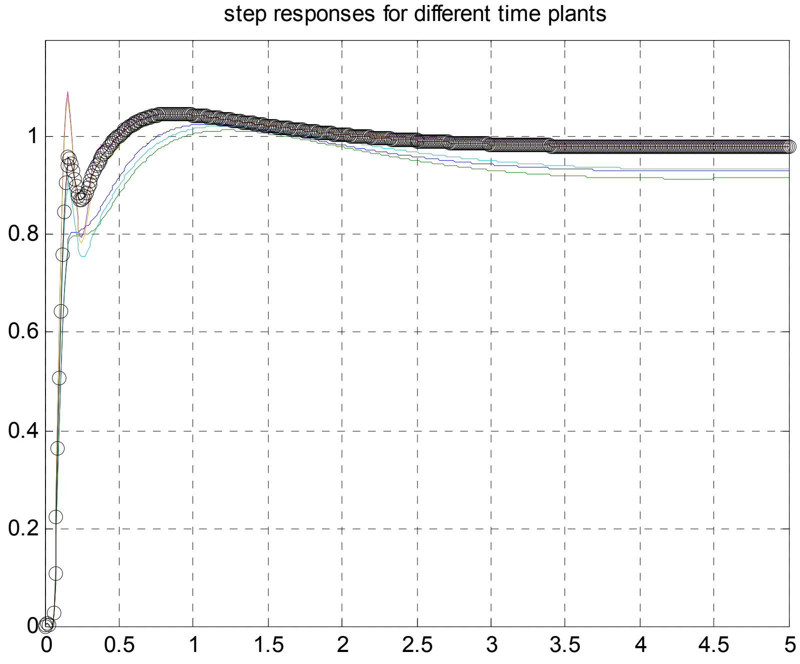

Figure 6.31: Flare Phase close loop pitch control step response over the envelope

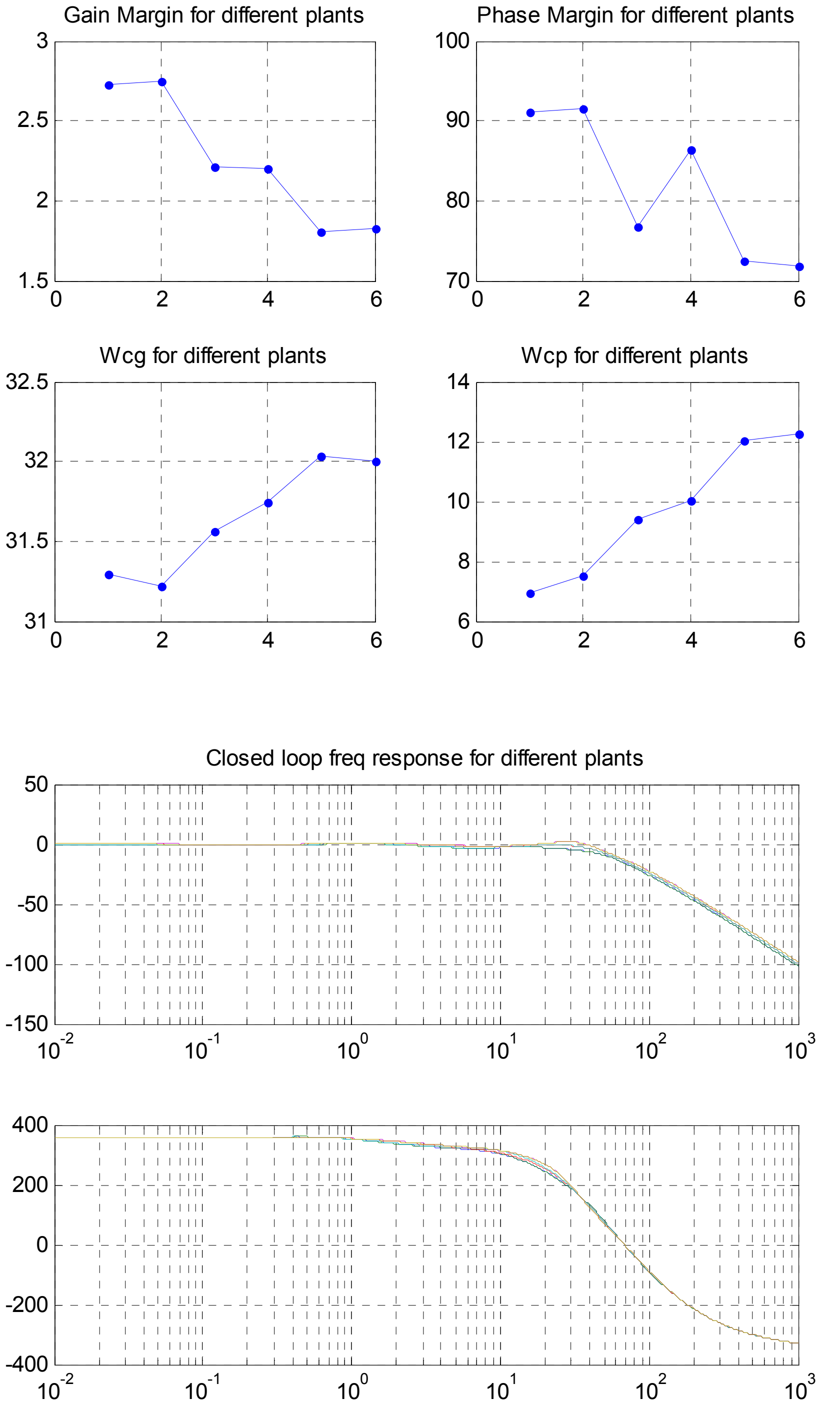

Figure 6.32: Flare phase open loop pitch control stability margins and close loop bode plot over the envelope

6.3.3.5 Vertical Velocity Controller

Bode plot for vertical velocity transfer function with cascaded pitch loop is shown in Figure 6.33. The weights selected for loop shaping of height transfer function are given below and shown in figure 6.34

$$W1 = \frac{(s+0.1)}{(s+0.001)} \qquad W2 = \frac{1.6534(s+6)}{(s+0.01)(s+100)}$$

The shaped plant frequency response is shown in figure 6.35.

Using H∞ loop shaping algorithm from [**35**], algebraic riccati equations are solved and the resulting controller for vertical velocity loop control has gamma = 1.8978 with gain margin 5.16 @ 11.59 rad/sec and phase margin is 72.36^o @ 2.13 rad/sec.

Nyquist plot is given in figure 6.36. Bode plot of close loop vertical velocity transfer function and sensitivity transfer function with H∞ controller is given in figure 6.37. Step response of close loop vertical velocity transfer function is given in figure 6.38. Figure 6.39 represents the evaluation of designed control on whole flare envelope while figure 6.40 shows the stability margins and close loop frequency response over the whole envelope.

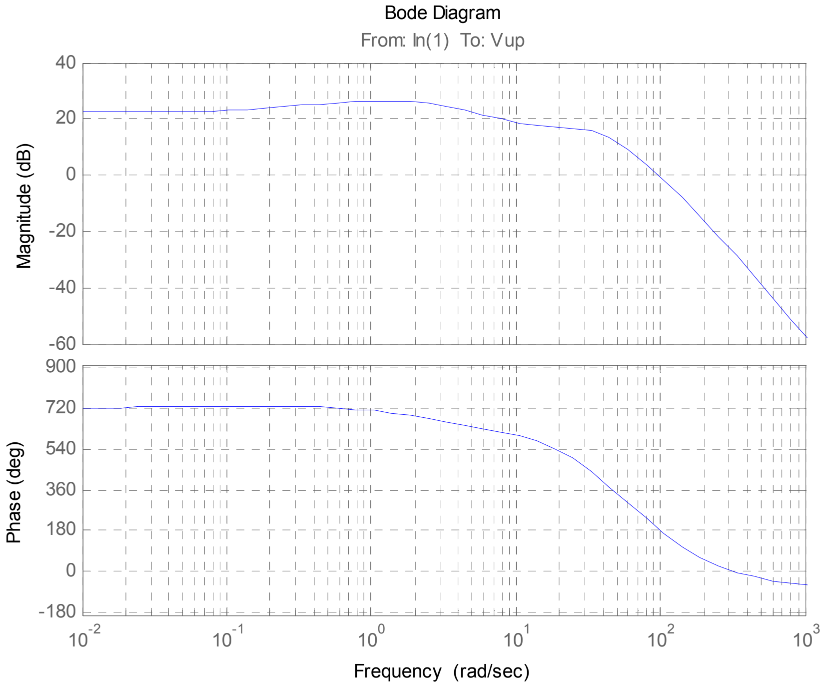

Figure 6.33: Bode plot of Flare Phase Vertical Velocity transfer function with cascaded pitch loop

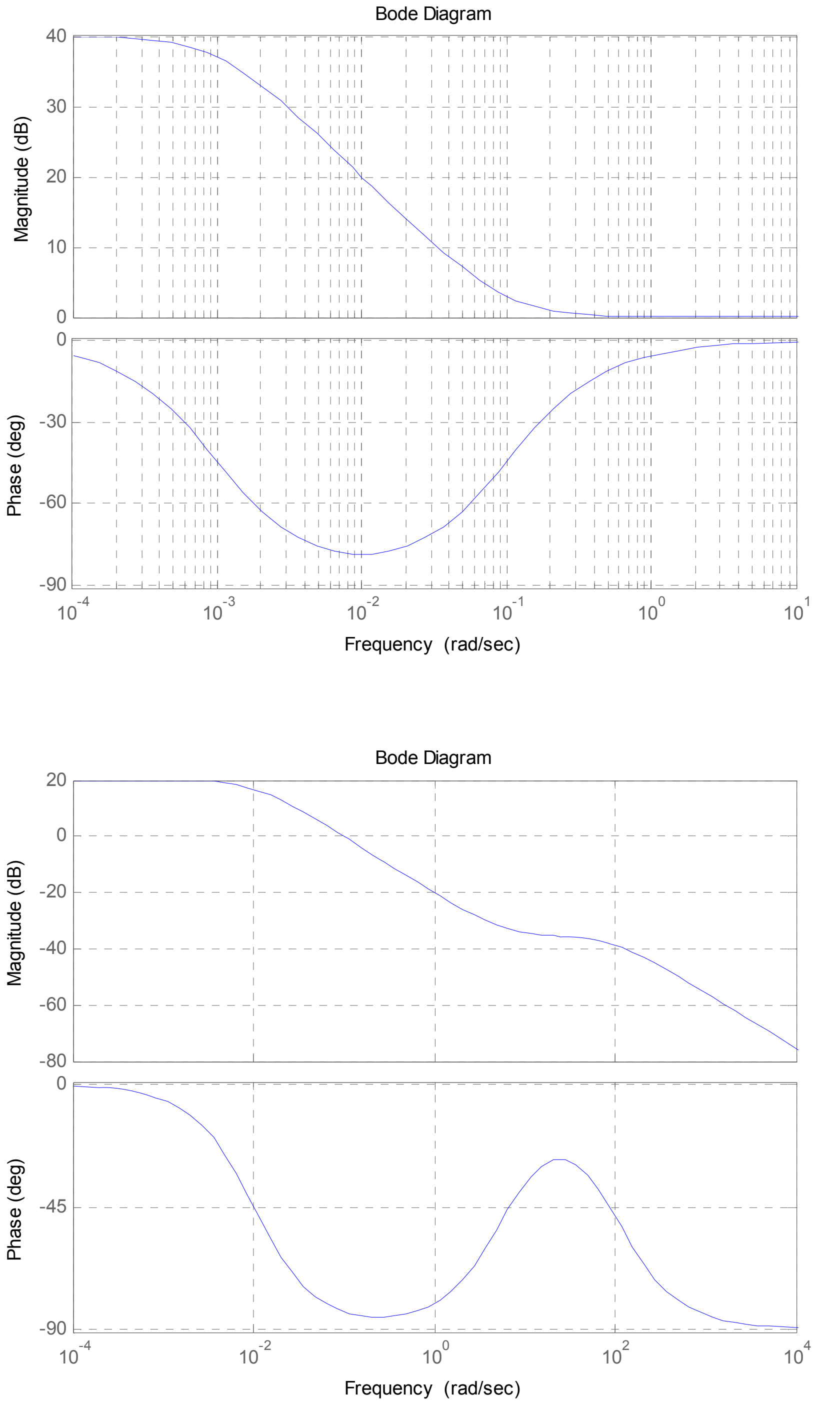

Figure 6.34: Bode plots of weights W1 and W2 for shaping vertical velocity loop

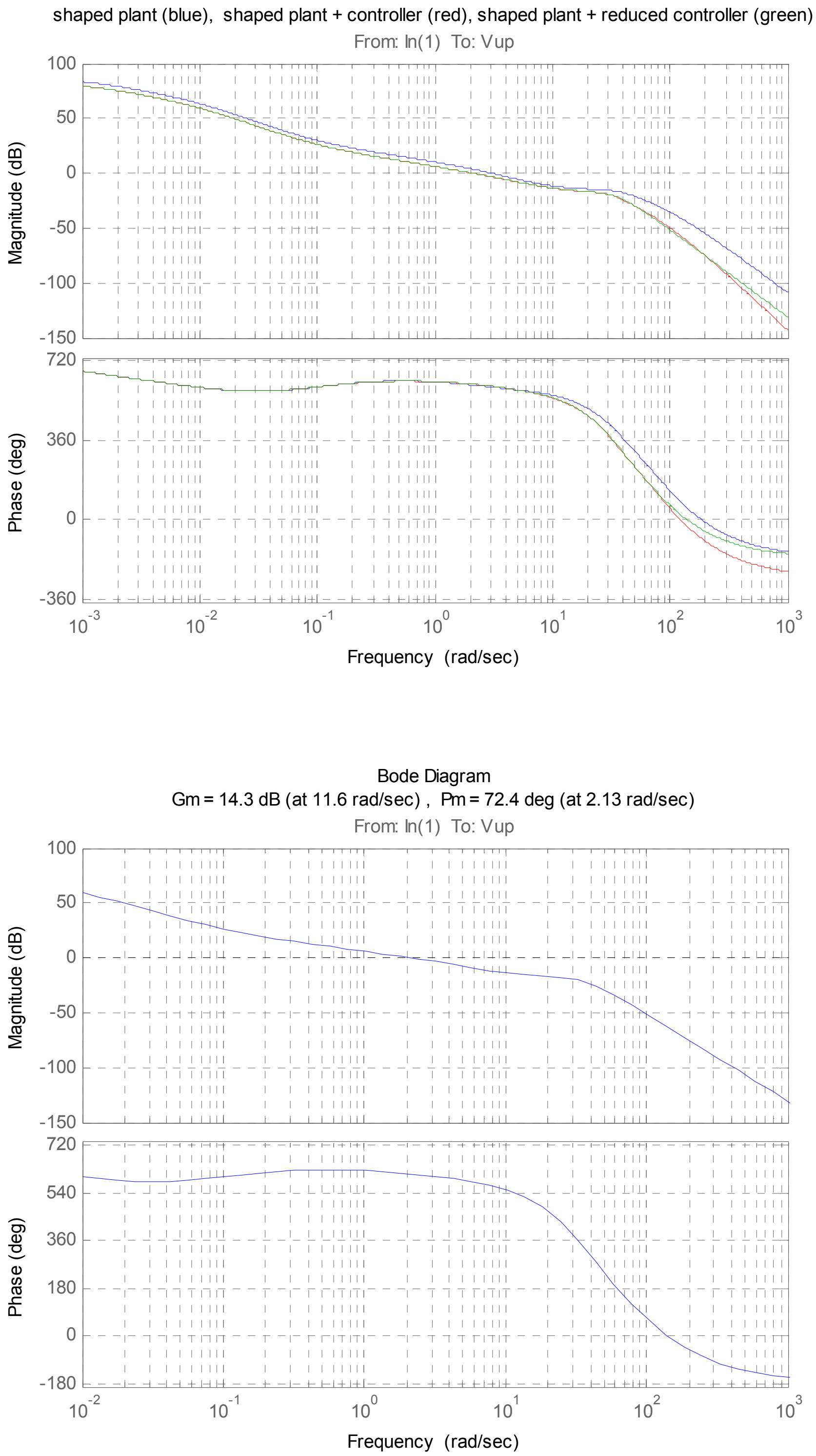

Figure 6.35: Open loop bode plot for vertical velocity transfer function with H∞ controller

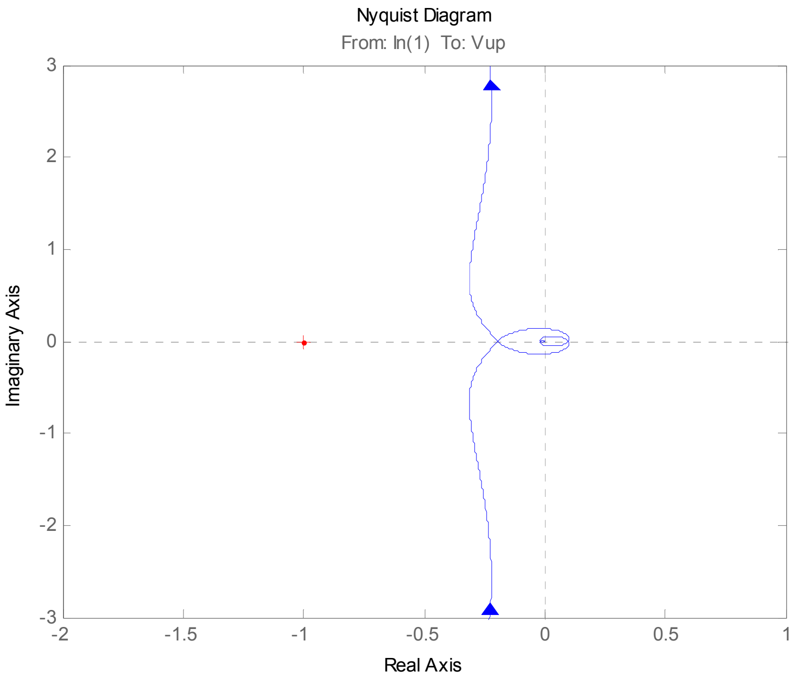

Figure 6.36: Nyquist plot for vertical velocity open loop transfer function with H∞ controller

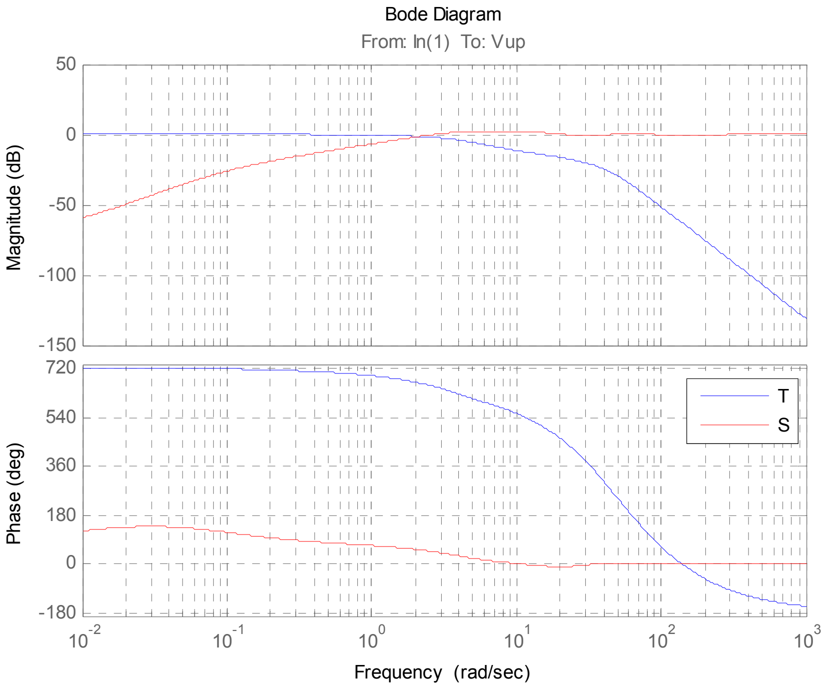

Figure 6.37: Vertical velocity close loop bode plot and sensitivity transfer functions with H∞ controller

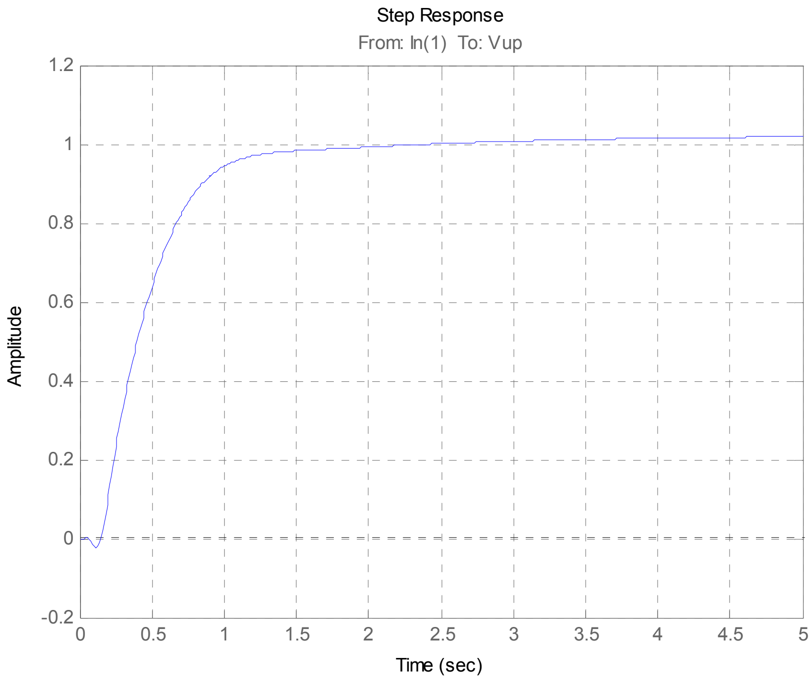

Figure 6.38: Close loop step response for vertical velocity with H∞ controller

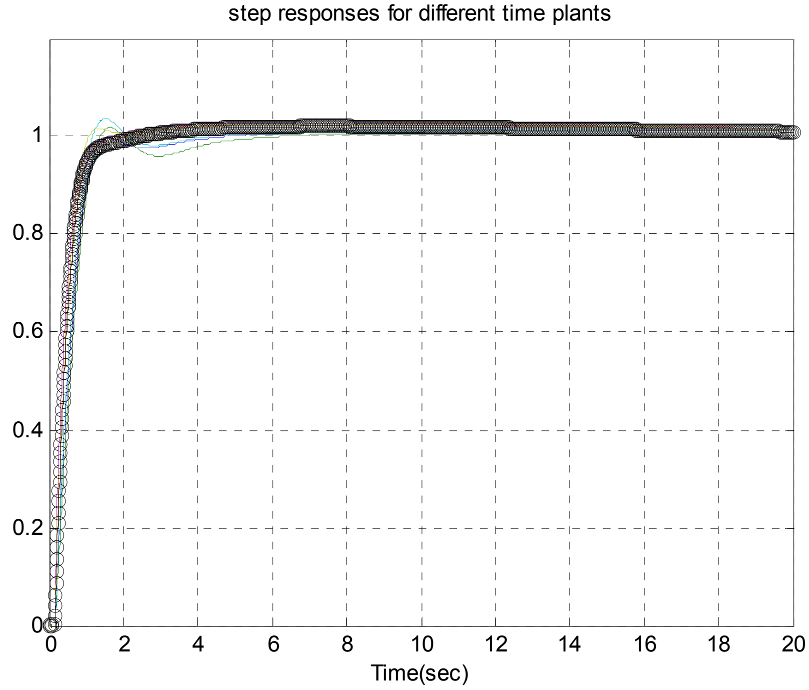

Figure 6.39: Flare Phase close loop Vertical Velocity step response over the envelope

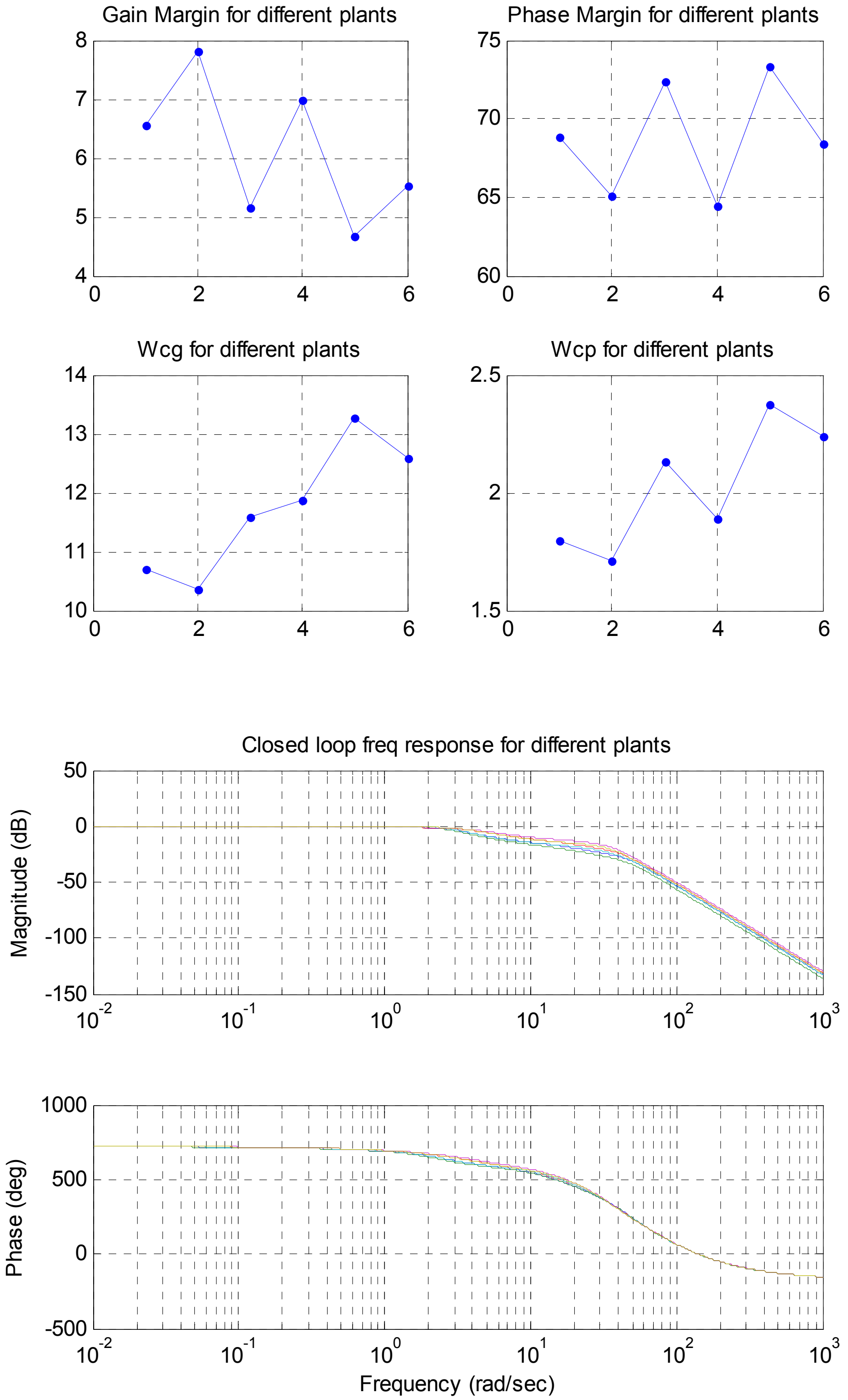

Figure 6.40: Flare Phase stability margins and close loop bode plot over the envelope

Chapter 7: Simulation Results

The simulation results of autonomous landing of FASER UAV are presented in this chapter. Glide phase and flare phase results are presented separately, showing the commanded height and vertical velocity profile and its following in the outer loops and the subsequent pitch attitude command and its following in the inner loop. Distance to runway for relative position of UAV from runway is also present, while this distance becomes negative once the UAV crosses the glide slope initiation point on runway. All the results are for landing phase till touch down on runway for the implemented trajectory generation algorithm and tracking controller in nonlinear simulation.

Section 7.1 presents the glide phase tracking performance and subsequent discussion of any shortcomings/ observations. Section 7.2 presents the flare phase tracking performance, touch down impact and subsequent discussion of any shortcomings/observations in results.

7.1 Glide Phase

The UAV is at 30 m altitude in base leg. It catches the glide slope at 355m from glide initiation point on runway. Subsequently, the height tracking controller starts following of generated glide phase height command till flare initiation height.

Figure 7.1 – 7.5 shows the glide phase performance. The tracking of height command is within ±3 m and it reduces to -0.5 m at flare initiation height. This error in height command tracking is low but it introduces a bias for flare phase performance in the form of late touchdown. An early touch down can be observed if actual height remains below the glide phase height command. Command tracking can be further improved by increasing the bandwidth of controller, but this will result in reduced uncertainty bound during glide phase in comparison to marginal increase in error reduction.

The kink in height reference and subsequently in tracking error at glide start is due to the fact that a band in height is required to be defined for switching from base leg height reference to glide height reference. This marks the start of glide phase. The glide phase height command is based on distance to runway calculation which decreases monotonically and depends on resolution of GPS. Thus a band needs to be defined in order to cope with this distance resolution.

Pitch loop controller performance can be depicted from figure 7.2 and its ability to track the pitch angle command generated by the height loop both in steady state and in transient state. The error in pitch tracking is within ±0.5^{o}, which is exceptionally good.

Elevator deflection in figure 7.3 depicts that enough control authority is still available to have more tighter control. The transients in elevator deflection is low which is due to the kink present for base leg to glide phase height command switching. Distance to runway in figure 7.4 shows the catching of glide slope at around 350m and termination of glide phase at around 24m.

7.2 Flare Phase

The UAV is at 2.03 m above ground when it initiates a flare maneuver. Height controller of glide phase gets disengaged and vertical velocity controller starts sending in pitch command to flare phase cascaded pitch loop controller that in turns generate elevator command.

Vertical velocity tracking controller performance during flare phase is depicted in figure 7.6. The controller is able to track the flare phase generated vertical velocity command with an error of ±0.4m/sec and touches down with -0.6m/sec vertical velocity ensuring low impact at touchdown. This error in vertical velocity results in early touchdown with resulting distance to runway at touchdown to be -17m. The designed value for distance to runway at touch down is -20m for this case. The error of 3m is due to limitation in tracking of vertical velocity command. Thus, the performance can be termed good as the touchdown is within ±4m band.

The distance to runway for flare phase in figure 7.10 becomes negative once the UAV crosses the glide slope initiation point on runway for flare maneuver.

Pitch angle tracking in figure 7.7 shows a tight tracking with an error of ±0.3^{o} and the transients are low while switching between glide and flare phase commands. Pitch angle at touch down is 5^{o} which ensures a main landing gear or rear wheel touch down before nose wheel.

Elevator deflection in figure 7.9 shows transient response which is due to switching from glide phase controller to flare phase controller. This transient can be further reduced by employing bumpless controller switching techniques. Angle of attack at touch down is close to 7^{o}, which is normal for such landings and is no way near to stall angle of attack for this UAV.

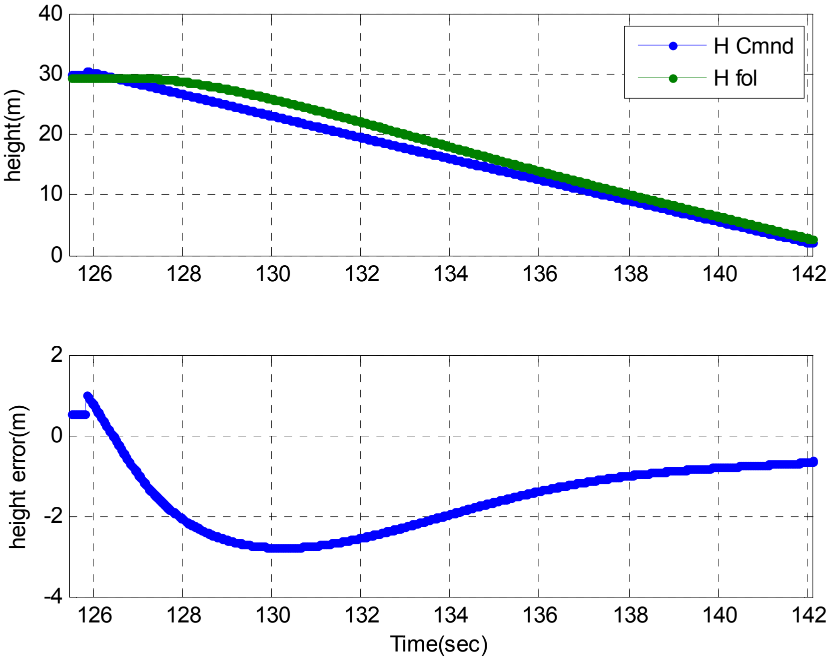

Figure 7.1: Glide phase height tracking

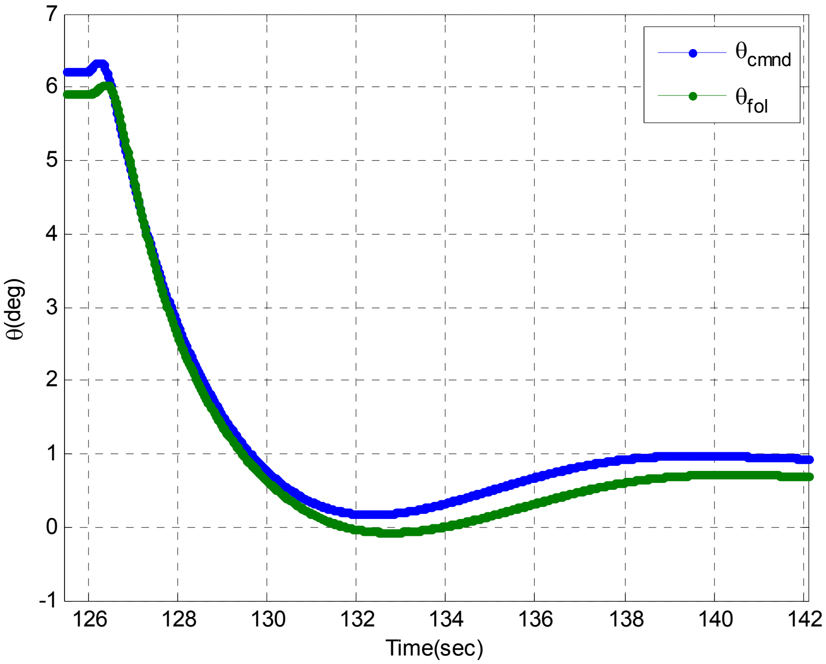

Figure 7.2: Glide phase pitch angle tracking

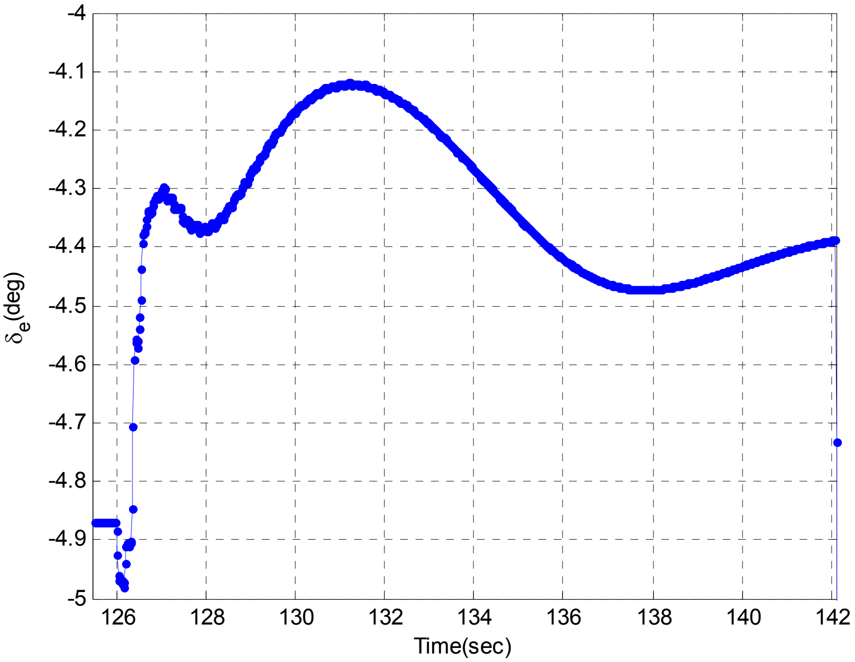

Figure 7.3: Glide phase elevator deflection

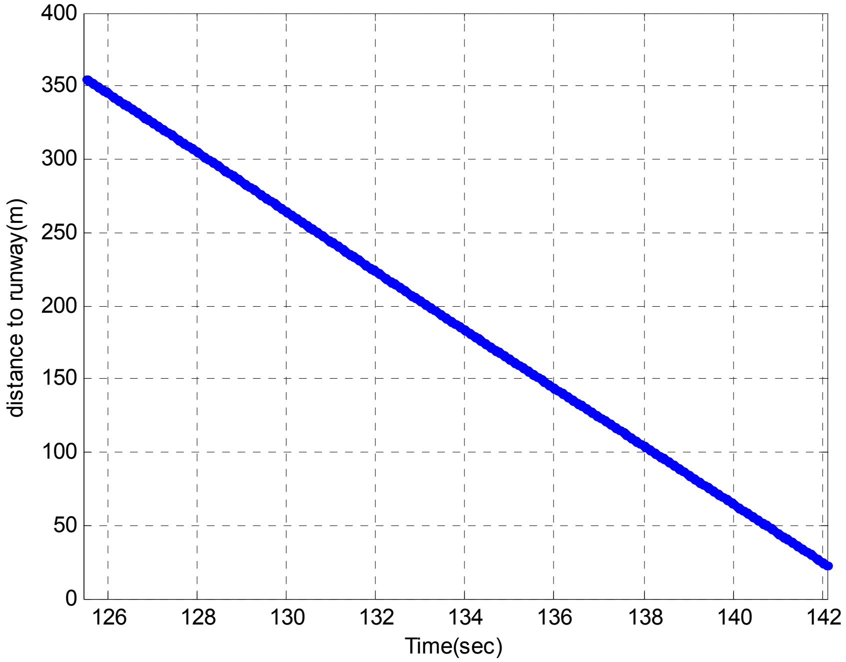

Figure 7.4: Glide phase distance to runway

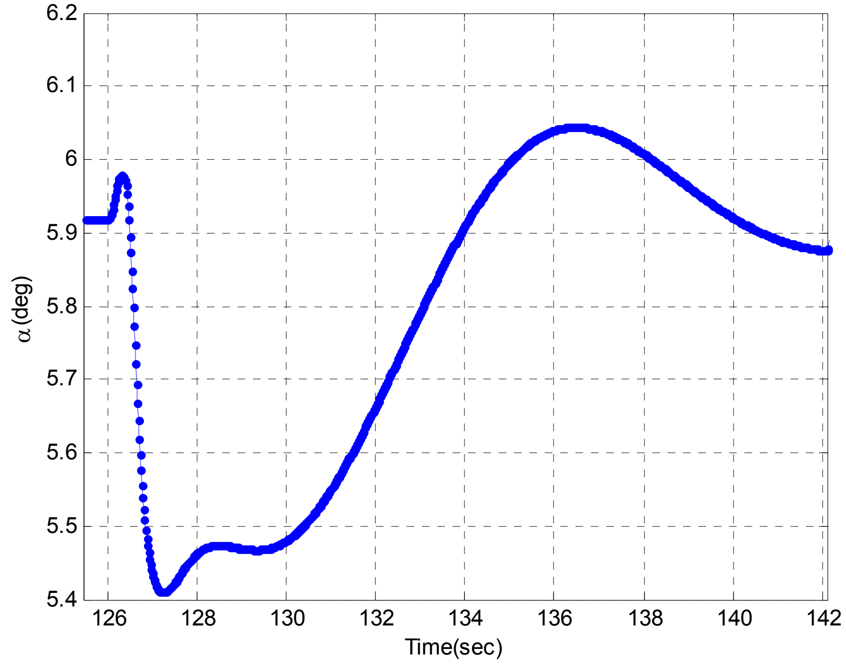

Figure 7.5: Glide Phase angle of attack

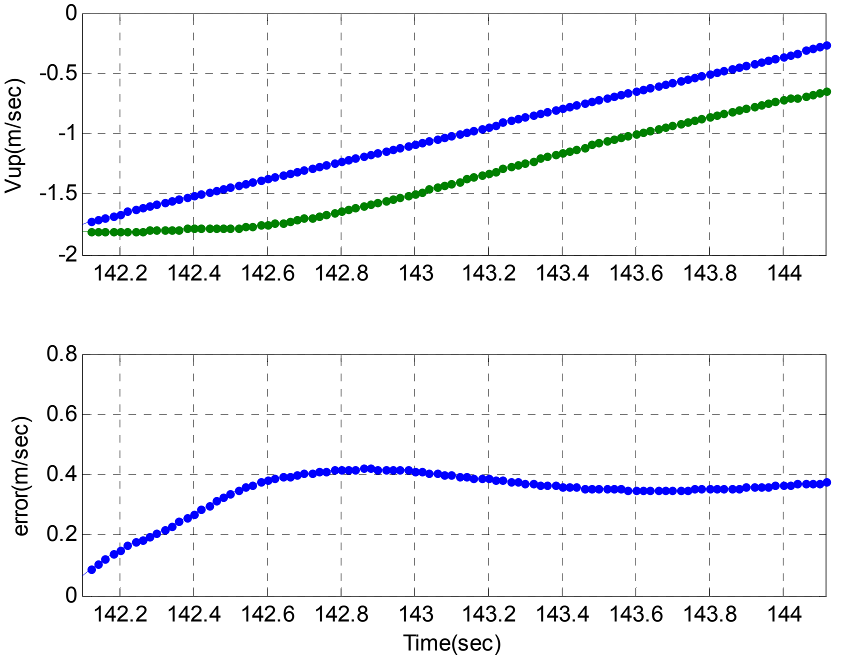

Figure 7.6: Flare phase vertical velocity tracking

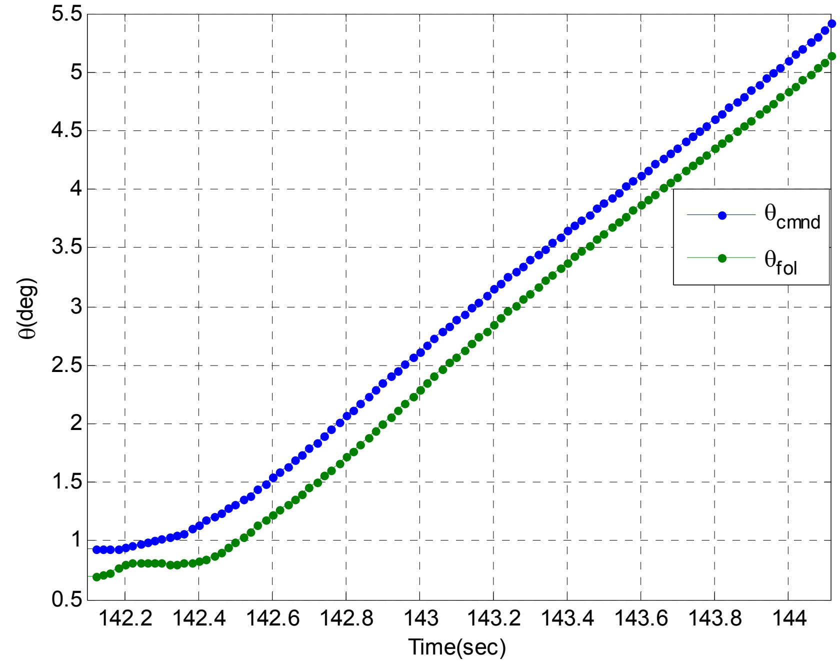

Figure 7.7: Flare phase pitch angle tracking

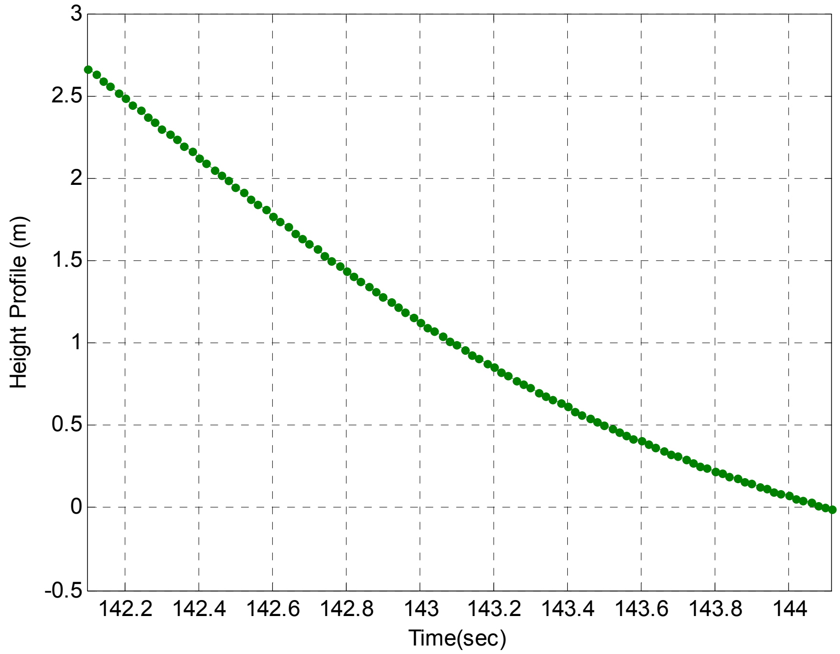

Figure 7.8: Flare phase height profile

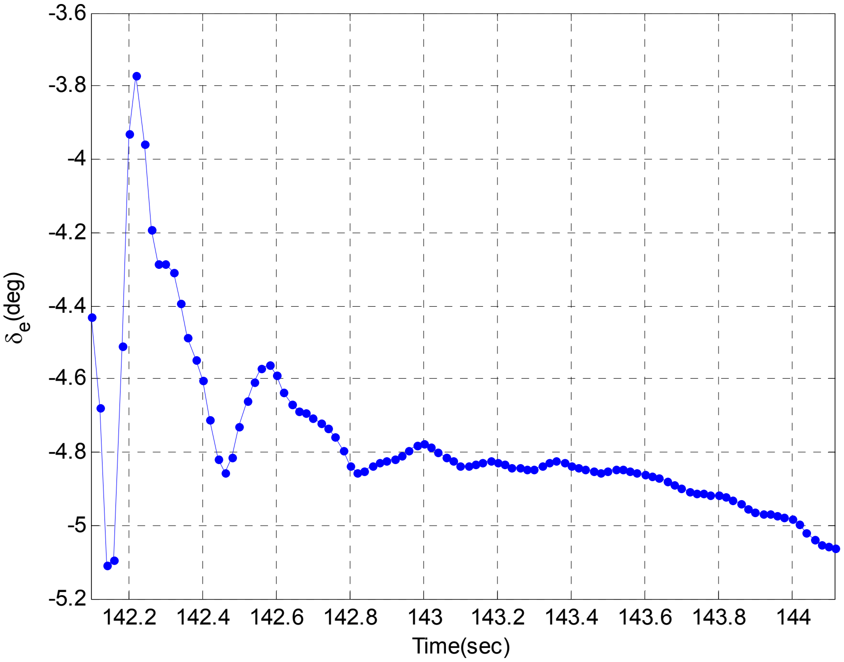

Figure 7.9: Flare phase elevator deflection

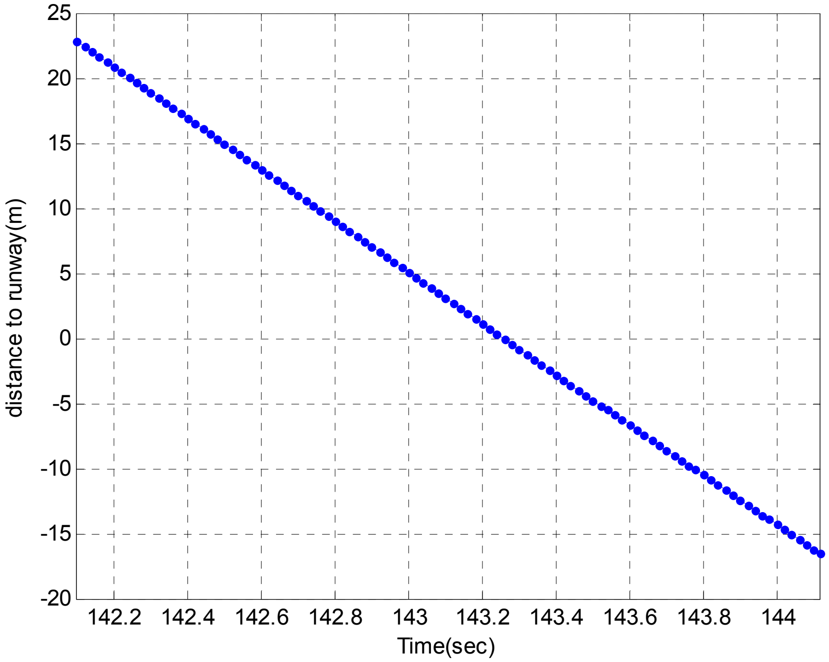

Figure 7.10: Flare phase distance to runway

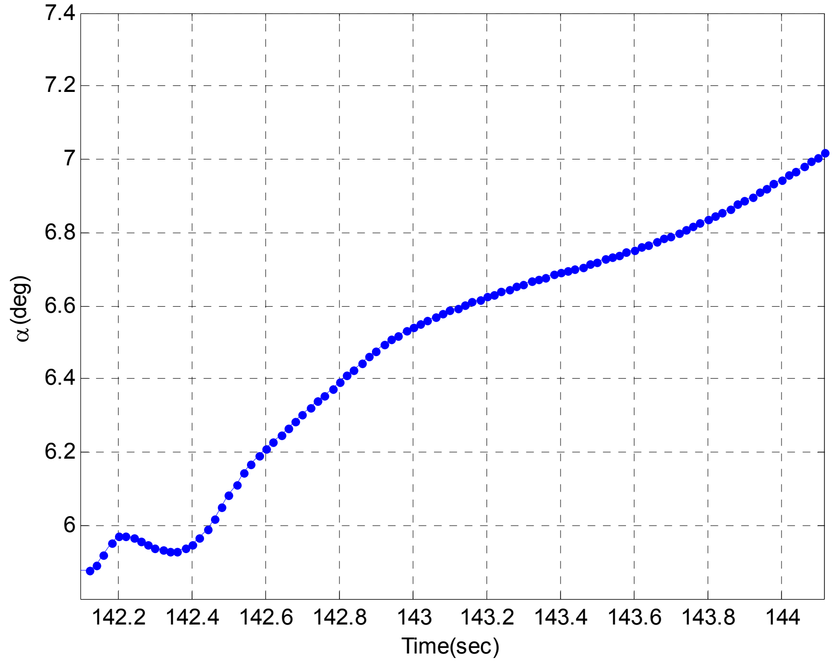

Figure 7.11: Flare Phase angle of attack

Chapter 8: Conclusion

8.1 Conclusion

Trajectory generation algorithm for automated landing of UAV on runway is designed and evaluated on FASER platform. The designed algorithm's performance is compared with existing trajectory generation algorithms. The developed algorithm outperforms the existing algorithms by giving reduced required distance for landing under the same set of boundary values. Online parameter calculation provision is developed and implemented to cater for any change from designed trajectory initial values. It proved to have low computational cost in comparison with the existing algorithms. It requires two linear equation to be solved iteratively while giving the benefits of touch down at intended point on runway with intended vertical velocity.

The tracking control algorithm in the form of H_∞ loop shaping controller is designed on linear models over the landing trajectory and its performance is evaluated over the whole landing envelope. The tracking control algorithm is implemented in nonlinear simulation and its performance for tracking of generated trajectory command to ensure touchdown at desired point with desired impact velocity is evaluated. The performance of generated trajectory algorithm and tracking control was found to be satisfactory.

8.2 Future Work Recommendations

The following items are suggested for future work:

- The trajectory generation algorithm is a boundary value problem and can be casted as an optimal control problem, while accounting for UAV dynamics in order to get the minimum possible landing distance, while conforming to impact velocity constraint and stall avoidance
- The UAV model can be implemented into the open source code Flight Gear and the proposed algorithm can be tested in real-time simulation and performance can be evaluated
- Flight test can be conducted for evaluation of proposed algorithm
- The algorithm can be implemented on other UAV platforms and ultimately in autopilots on manned aircraft for performance evaluation

References

[1] Unmanned Vehicle Systems International web site, http://www.uvs-international.org/

[2] Jackie Northam. (2012, August) NPR. [Online]. http://www.npr.org/2011/07/11/137710942/popularity-of-drones-takes-off-for-many-countries

[3] Sharon Weinberger. (2012, May) Popular Mechanics. [Online]. http://www.popularmechanics.com/technology/military/planes-uavs/darpas-uav-crowd-sourcing-contest#slide-1

[4] Draganfly News. (2012, August) Draganfly. [Online]. http://www.draganfly.com/news/2008/08/24/introduction-to-unmanned-aerial-vehicles-uavs/

[5] Andrew Callam. (2012, August) International Affairs Review. [Online]. http://www.iar-gwu.org/node/144

[6] The General Atomics Predator. (2012, August) Vectorsite. [Online]. http://www.vectorsite.net/twuav_07.html

[7] Jeff Schogol. (2009, April) Stars and Stripes. [Online]. http://www.stripes.com/news/official-air-force-losing-more-drones-than-army-1.90858

[8] Clark, D., “Approach and Landing Accident Reduction (ALAR) and Energy Management”, Mobility Forum, 2005.

[9] Leong Woei, “Computer Aided Landing Control System Design For A Fixed Wing UAV”: Master's dissertation, National Cheng Kung University, 2006.

[10] K. Senthil Kumar, C. Sudhir Reddy, and J Shanmugam, "Design and Simulation of Blending Function for Landing Phase of a UAV," Defence Science Journal, vol. 58, no. 3, pp. 315-326, May 2008.

[11] J. H. Blakelock, Automatic Control of Aircraft and Missiles, 2nd ed. New York: John Wiley & Sons, Inc, 1991.

[12] S. Brian L, F. L. Lewis, Aircraft Control and Simulation, Wiley Interscience, 2003.

[13] M. I. Salfi, U. Ahsun and H. A. Bhatti, “Lateral and Longitudinal Guidance and Control Design of a UAV in Auto Landing Phase”, Proceedings of International Bhurban Conference on Applied Sciences & Technology Islamabad, Pakistan, January 7 – 10, 2009

[14] S. Park, J. Deyst, and J.P. How. “A new nonlinear guidance logicfor trajectory tracking”, AIAA Guidance, Navigation, and Control Conference and Exhibit, Providence,Rhode Island, 16-19 August 2004

[15] M. I. Lizarraga, Autonomous Landing System of a UAV.: Naval Postgraduate School, Monterey California, 2004.

[16] S Padhi and R Singh, "Automatic Path Planning and Control Design for Autonomous Landing of UAVs using Dynamic Inversion", American Control Conference, St. Louis, MO, USA, 2009, pp. 2409-2414.

[17] A Cho et al., "Fully Automatic Taxiing, Takeoff and Landing of a UAV only with a Single-Antenna GPS Receiver," in Proceedings of the 21st International Technical Meeting of the Satellite Division of The Institute of Navigation (ION GNSS 2008), Savannah, GA, 2008, pp. 1174 - 1181.

[18] F. N. Alberts, Accurate Autonomous Landing of a Fixed-Wing Unmanned Aerial Vehicle: Master’s dissertation, Stellenbosch University, 2012

[19] S. J. A. Smit, Autonomous Landing of a Fixed-Wing Unmanned Aerial Vehicle using Differential GPS: Master’s dissertation, Stellenbosch University, 2013

[20] Hann-Shing Ju, Ching-Chin Tsai, “Glidepath Command Generation and Tracking for Longitudinal Autolanding”, Proceedings og the 17th World Congress, The International Federation of Automatic Control, Seoul, Korea, July 6-11, 2008

[21]Dong Il,You,Yeon Deuk, Jung, Sung Wook, Cho, Hee Min, Shin, Sang Hyup, Lee and D.H. Shim, "A Guidance and Control Law Design for Precision Automatic Take-off and Landing of Fixed-Wing UAVs", AIAA Guidance, Navigation, and Control Conference 13-18 August 2012, Minneapolis, Minnesota.

[22]Pashilkar, A.A., Sundararajan, N. Saratchandran, P., "A Fault-Tolerant Neural Aided Controller for Aircraft Auto-landing", Aerospace Science and Technology, Volume 10, Issue 1, January 2006.

[23]Rosa, P., Silvestre C., Cabecinhas, D., Cunha, R., "Autolanding Controller for a Fixed Wing Unmanned Air Vehicle", AIAA Guidance, Navigation and Control Conference, South Carolina, 2007.

[24]Malaek, S.M.B., Sadati, N., Izadi, H., Pakmehr, M., "Intelligent Autolanding Controller Design using Neural Networks and Fuzzy Logic", 5th Asian Conference, 2004.

[25]Shue, S. P., and Agrawal, R. K., "Design of Automatic Landing Using Mixed H2/ H_∞ Control", Journal of Guidance, Control, and Dynamics, Vol. 22, No. 1, 1999, pp. 103–114.

[26]Attar M., Wahnon E., Chaimovitz D., "Advanced Flight Control Technologies for UAVs", 2nd AIAA "Unmanned Unlimited" Systems, Technologies And Operations, 15- 18 September 2003, San Diego, California, AIAA 2003-6537

[27]UAV Laboratories, UNIVERSITY OF MINNESOTA website,
http://www.uav.aem.umn.edu/

[28]Murch, A. and Y. C. Paw and R. Pandita and Z. Li and G. J. Balas,"A Low Cost Small UAV Flight Research Facility," 1st CEAS Specialist Conference on Guidance, Navigation, and Control, April 2011

[29]Unmanned Dynamics. Aerosim blockset homepage. [Online]. Available:
http://www.u-dynamics.com/aerosim/default.htm

[30]Paw, Y. C. "Synthesis and Validation of Flight Control for UAV," PhD Dissertation, University of Minnesota, 2009

[31]Volkan Kargin, "Design of An Autonomous Landing Control Algorithm for a Fixed Wing UAV": Master's dissertation, Middle East Technical University, 2007.

[32]Skogestadt S. and Postlethwaite I, Multivariable Feedback control, Wiley, 1996.

[33]K. Turkoglu, E. M. Jafarov, "H_∞ Loop Shaping Robust Control vs. Classical PI(D) Control: A case study on the Longitudinal Dynamics of Hezarfen UAV", Proceedings of the 2nd WSEAS International Conference in Dynamical Systems and Control, Bucharest, Romania, October 16-17, 2006

[34]S. Iqbal, A. I. Bhatti, M. Akhtar and S. Ullah, "Design and Robustness Evaluation of an H_∞ Loop Shaping Controller for a 2DOF Stabilized Platform", Proceedings of the European Control Conference 2007, Koa, Greece, July 2-5, 2007

[35]Ian Postlethwaite, Multivariable Feedback Control Analysis and Design, 4th Edition JOHN WILEY & SONS publishing company, New York, 1998.